Part Three

Functionalized Nanomaterial for Environmental Techniques

8

Photocatalysis: Activity of Nanomaterials

Tetiana Tatarchuk,[1] Amalthi Peter,[2] Basma Al-Najar,[3] Judith Vijaya,[2] and Mohamed Bououdina[3]

[1]*Vasyl Stefanyk Precarpathian National University, Department of Theoretical and Applied Chemistry, 57, Shevchenko Str., Ivano-Frankivsk 76018, Ukraine*
[2]*Loyola College, Department of Chemistry, Catalysis and Nanomaterials Research Laboratory, Nelson Manickam Road, Chennai, Tamil Nadu 600034, India*
[3]*University of Bahrain, Department of Physics, PO Box 32038, Sakhir, Kingdom of Bahrain*

8.1 Nanomaterials for Photocatalysis

In the past few years, nanomaterials have emerged as one of the main influencers in technology and biomedicine. The extremely small size of nanomaterials (5–100 nm) owe them miraculous properties due to their large surface area in addition to quantum confinement. It is well known that nanomaterials can be shaped in many forms as rods, thin films, powder, and so on [1,2]. They also can be synthesized through several methods resulting in different shapes, sizes, and properties [3]. Therefore, they are applied in mostly every life sector including drugs and modifications, manufacturing, and materials, environmental issues, electronics, energy production, and industry [4]. The photocatalysis process using the unique properties of nanomaterials has been applied in a wide range of applications such as degradation of pollutants from atmosphere and water. It is also used in producing energy. Some nanomaterials such as oxides [5–7], semiconductors [8,9], metals [10,11], and graphene [12,13] have shown great effect on photocatalysis processes [14,15] due to their enhanced and controllable optical properties, which makes them excellent photocatalysts. This chapter will discuss the mechanism of photocatalysis processes using nanomaterials and their applications. Table 8.1 shows some of the nanoparticles applied for photocatalytics procedures. The chapter will also focus on the different types of nanomaterials used in photocatalysis in terms of their synthesis method, microstructure, and their optical and magnetic properties.

Nanotechnology in Environmental Science, First Edition. Edited by Chaudhery Mustansar Hussain and Ajay Kumar Mishra.

Table 8.1 Some of the nanoparticles applied in photocatalytic procedures.

Nanoparticles	Irradiation	Mechanism of photocatalysis enhancement	Reference
TiO_2/WO_3	Sun light/solar UV–visible light	Heterogeneous	[15]
ZnO/Ag	UV (320–400 nm)	Heterogeneous/SPR	[5]
WO_3/TiO_2	UV (365 ± 5 nm)	Heterojunctional-electrical layered system	[6]
p-type -FeOOH/n-type $WO_3 \cdot H_2O$	UVA (365 nm)	Semiconductors	[16]
Zinc and copper co-doped WO3	Visible light (>420 nm)	Heterogeneous	[17]
N-TiO_2	Visible light	Doping	[18]
Fe-doped response TiO_2 film	Visible light	Doping	[19]
Graphitic carbon nitride (g-C_3N_4) with graphene oxide (GO)	Visible light	Heterogeneous	[12]
TiO_2/graphene oxide (GO) composite nanofibers	Visible light	Heterogeneous	[13]
Gold-doped PdO NPs	(UV) 254 nm	"UV + H_2O_2" system batch system	[20]
Ag NPs on Cd(II) boron imidazolate	UV	SPR	[10]
Ag NPs	UV	SPR	[21]
Ag-polymer core-shell NPs	UVA	SPR	[11]
Gd-doped PbSe NPs	Visible light irradiation	Doping	[8]
$M_xBi_{2-x}Ti_2O_7$ (M: Fe, Mn)	UV light (≥320 nm) Visible light (≥ 400 nm)	Heterogeneous	[9]
Ni-doped CuS	Visible light	Doping	[22]
Na-doped ZnO	Solar irradiation	Doping	[23]

8.2 Mechanism of Photocatalysis

Photocatalysis is a series of chemical reactions that is usually induced by electromagnetic irradiation. This will cause excitation of atoms of the irradiated materials that results in radicals that affect surroundings [5]. Photocatalysis process can be divided into two main stages: reduction and oxidation [24]. When a material is irradiated with photons with energy equal to or higher

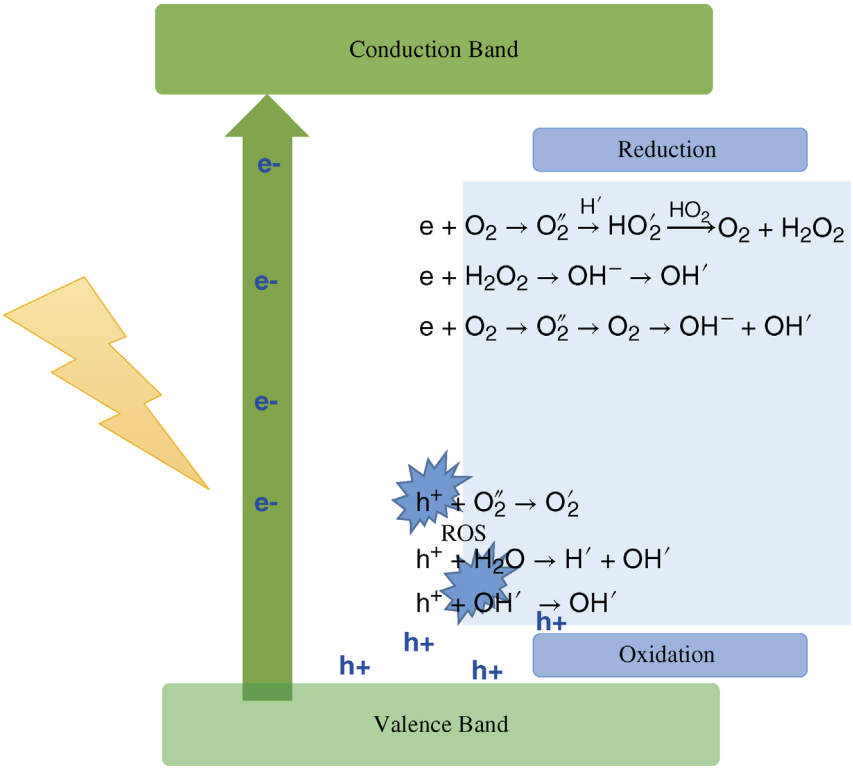

Figure 8.1 Mechanism of photocatalytics process including chemical reactions.

than its bandgap, electrons in the conduction band (CB) will jump to the valence band (VB) through the bandgap leaving positive holes, and this stage is called reduction (Figure 8.1). As a result of reduction, the generated electrons and holes lead to the formation of reactive oxygen spices (ROS) such as O_2 and OH (oxidation). The kind of ROS depends on the type of material and irradiated photons. A typical photcatalysis process is shown in Figure 8.1. The formation of ROS is the significant outcome of photocatalysis, as it can cause various effects such as degradation of dye [10] and antibacterial activity [20]. Other applications of photocatalytic activity are mentioned in Table 8.2. A series of chemical effects occur as a result of photocatlysis. Figure 8.1 shows example of chemical reactions occurs during photocatalysis process.

Efficiency of photocatalysis process can be evaluated by its effect on the surroundings such as degradation, adoption, reduction, or antibacterial activity. The common way of evaluating the efficiency of the photocatalytic process is to compare between the initial concentration of the unwanted substances with the concentration of these substances after the photocatalytic reactions using the following equation:

$$\ln \frac{C_0}{C_t} = kt,$$

Table 8.2 Applications of photocatalytic applications using nanoparticles.

Nanoparticles	Application	Reference
TiO_2/WO_3	Degradation of steroid hormones (EES)	[15]
N-TiO_2	Hydrogen production	[18]
TiO_2	Food safety	[25]
TiO_2	Degradation of tetracycline (antibiotic compound)	[26]
Au-doped PdO NPs	Degradation of tetrodotoxin (TTX) (water pollutant)	[20]
Ag NPs on Cd(II) boron imidazolate	Degradation of methylene blue	[10]
Ag NPs	Degradation of methyl orange, methylene blue, and rhodamine chloride	[21]
Gd-doped PbSe NPs	Degradation of sulfasalazine degradation (pharmaceutical compounds)	[8]
Ag-TiO_2	Degradation of acetaldehyde (air pollutant)	[11]
$M_xBi_{2-x}Ti_2O_7$ (M: Fe, Mn)	Degradation of methyl orange	[9]
Ni-doped CuS	Degradation of RhB	[22]
Na doped ZnO	Degradation of RhB	[27]
g-AgBr/Al-MCM-41	Degradation of basic fuchsin, crystal violet, and aniline toxic organic compounds	[28]
Nano-WO_3	Antimicrobial applications	[29]

where C_0 is the initial concentration, C_t is the reaction concentration, k is the reaction rate constant, and t is time between the two concentrations [22].

The efficiency of photocatalysis activity depends on the yield of the created electrons and holes [8]. The recombination of the electron–hole pair is one of the main factors that reduce the efficiency of the photocatalytic activity [16], and hence attempts were made to diminish the recombination rate by applying voltage to create a current that ensures separation between holes and electrons (photoelectron catalysis) [16]. Graphitic carbon nitride (g-C_3N_4) nanosheets [30] were applied for photoelectrocatalysis for the degradation of phenol from water under visible and UV light using different voltage ranging from 0.5 to 3 V (Figure 8.2). It was found that the degradation rate increases with increasing the bias voltage, reaching its maximum at 2.5 V when the phenol degraded completely after 5 h (Figure 8.2b). This was explained by the higher rate of hole generation at higher voltage and hence higher production of free radicals that promotes the photogdegradation rate. However, when the voltage exceeded a certain limit (2.5 V), the degradation rate started reducing again due to the rearrangements of layers in the media (space charge layer and Hector Helmhotz layer). The effect of external bias was also obvious when TiO_2 hollow spheres were used to remove toxic Cr (VI) from wastewater by applying an external voltage that increased the removal rate of Cr (VI) by 28% [31]. The voltage applied in this case ranged from 1 to 10 V and it was

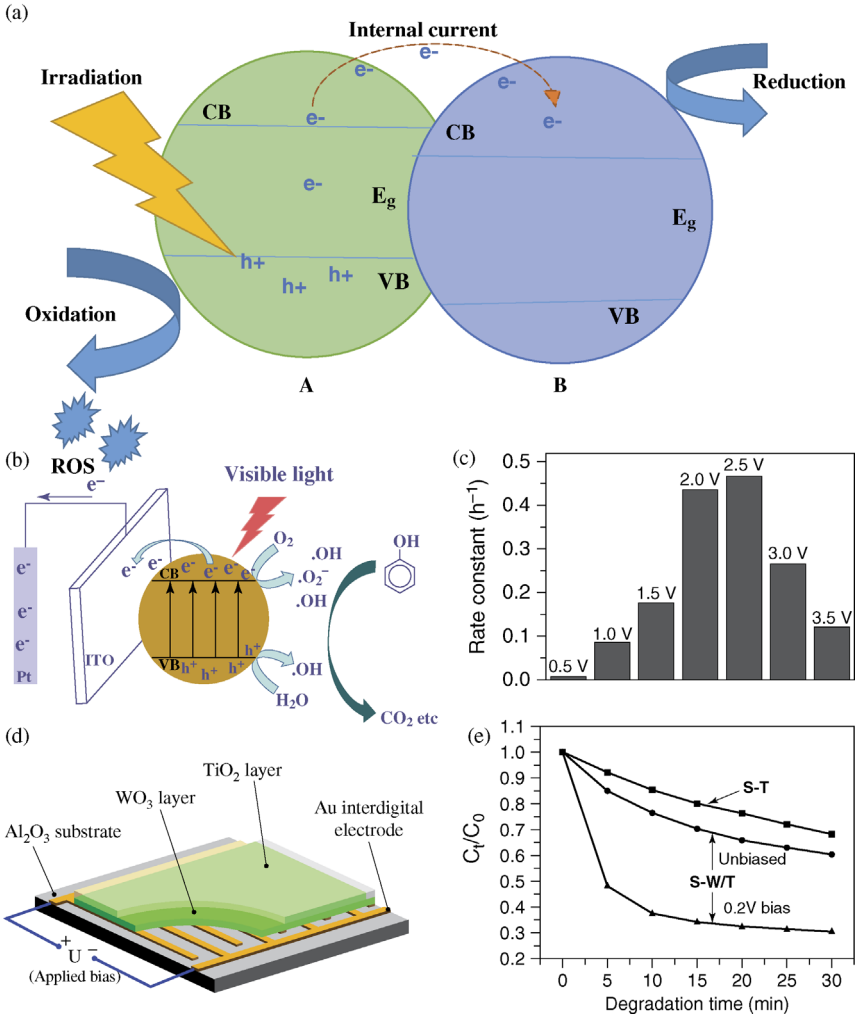

Figure 8.2 (a) Mechanism of hetrostructure photocatalysis. (b) PEC degradation mechanism of phenol by g-C3N4 film electrode [30] (c). The rate constants for EC degradation activity of g-C_3N_4 film electrode for phenol at various potentials in 0.1 M Na_2SO_4 solution (reproduced with permission from Ref. [30]. Copyright 2016, Elsevier). (d) Schematic diagram of the interdigital electrode/WO_3/TiO_2 HEL system (Al_2O_3 substrate, Au interdigital electrode layer, WO_3 layer, and TiO_2 layer from bottom to top) [6]. (e) Comparison of photocatalytic decomposition rates of toluene between S-T and S-W/T with no bias and 0.2 V bias (reproduced with permission from Ref. [6]. Copyright 2011, Elsevier).

found that voltage applied did not dramatically affect the degradation rate. In general, it has been stated that phoroelectrocatlysis not only reduces recombination but also allows electrochemical oxidation that significantly increases the photo-gedradation rate [31].

Another effective way to decrease the recombination rate is the use of heterogeneous structure (a mixture of different materials) [24]. This allows

electrons to move to other atoms in the structure, generating internal current that well separate hole–electron pairs [24]. This nanostructure can consist of a mixture of two oxides as TiO_2/WO_3 nanocomplex for the degradation of steroid hormones from water under solar light. It was proved that hybrid complex provided the maximum degradation rate (54%) in comparison with TiO_2 alone (38%) [15]. Moreover, two types of semiconductors were combined when n-type WO3 and p-type γ-FeOOH complex showed enhanced photocatalysis for degradation of rhodamine blue (RhB) from water [16]. Heterogeneous photcatalysis was also applied using a nanocomplex of zinc and copper codoped WO_3 prepared by precipitation and coprecipitation methods [17]. It was shown that such complex provided the maximum inhibition zone as an antibacterial under visible light (10.65 mm), while pure WO3 provided only (6.24 mm).

Heterogeneous structures can include plasmonic metal (Ag [5] or Au [14] that produce surface plasmon resonance (SPR), so electrons accumulate on the surface of the structure separating them effectively from holes and hence producing more ROS and promoting photocatalytic activity. Furthermore, heterojunctional-electrical layered system can be applied to achieve outstanding photocatalysis activity [6] as WO_3/TiO_2 nanocomplexes (Figure 8.2c) have shown better degradation percentage under 0.2 V to remove gaseous pollutant (Figure 8.2d).

8.2.1 Enhancement of Irradiation Absorption

The radiation applied in photocatalysis often ranges from ultraviolet (UV) to infrared including visible light. It is very essential that the energy of the applied radiation matches or is higher than the energy of the bandgap of the photocatalysis material. Some reported techniques are applied to enhance the absorbance of irradiation by the photocatalyst materials. These approaches can be explained as follows:

a) *Doping*: Doping with an element that has a high optical absorption is one of the effective ways of altering the bandgap to match the energy of the desired radiation and hence have a better radiation absorbance that enhances the potocatalytic activity [18,23,27,32]. For example, dopping TiO with nitrogen will reduce its bandgap from 3.2 to 2.5 eV and hence allow solar light to be absorbed [18] (Figure 8.3a). It was also reported that sol–gel ZnO nanocrystals doped with Na ions resulted in better absorbance compared to pure ZnO [27]. The obtained photoluminescence (PL) Spectra indicates that the amount of Na content affect the absorbance intensity. It was shown that a small amount of Na (0.5%) reduced absorbance around 60% in comparison with pure ZnO, while at 3% of Na, the absorbance raised by 55% [27]. It is very important to notice that the best radiation absorbance is not necessarily attributed to the best photocatalytic efficiency [9]. In the above case [27], the least absorbance with 0.5% Na has actually showed the most efficient degradation of RhB dye; that is, the most efficient photocatalysis.

   In some cases, doping itself resulted in reduction in photocatalytic rate [19]. This was shown when TiO thin films were doped with Cu [32] as higher amount of Cu resulted in less efficient photocatalytic activity. Higher amount

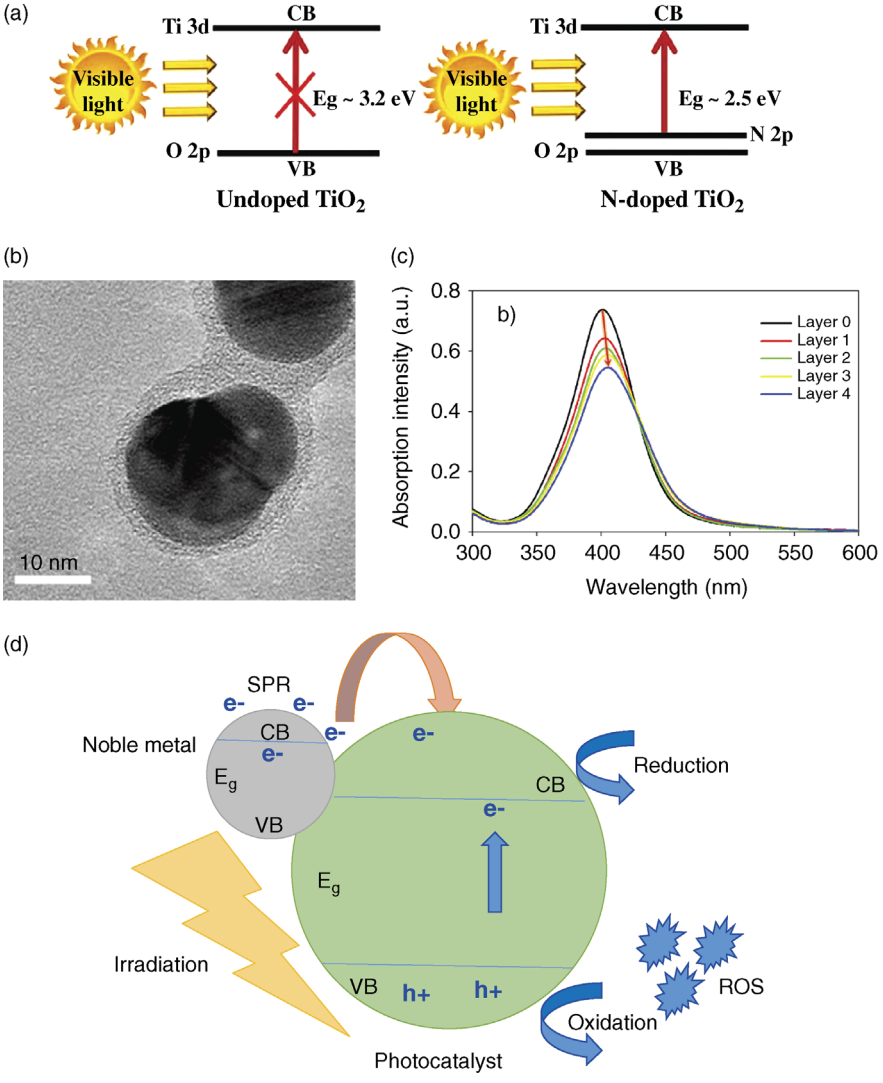

Figure 8.3 (a) Energy-level diagrams for undoped and N-doped TiO_2 [18] (reproduced with permission from Ref. [18]. Copyright 2017, Elsevier). (b) Silver core–shell nanoparticles with silver core and an ultrathin shell [11] (reproduced with permission from Ref. [11]. Copyright 2017, Elsevier). (c) UV–vis absorption spectra of core–shell silver nanoparticles as a function of adsorbed polyelectrolyte layer. The red arrow indicates the redshift in SPR peak position [11] (reproduced with permission from Ref. [11]. Copyright 2017, Elsevier). (d) Mechanism of plasmonic photocatalysis involving SPR effect (reproduced with permission from Elsevier).

of Cu could actually destroy the active catalyst sites or it could increase recombination of electron and ions that, eventually, lowers the photocatalytic activity. Similarly, when doped titanium nanocomposites (PTh/Sn-TiO_2) were used in photocatalysis with different dopant concentrations, a certain amount of concentration (1.5 wt %) revealed the most efficient result in the degradation of Congo red (CR) dye (almost 0% of CR in 120 min).

b) *Photosensitization of semiconductor*: It is reported that involving semiconductor in photoctalysis process, whether as a dopant or as part of a heterogeneous structure, would highly enhance the efficiency of photocatalytic activity resulting in a high rate of oxidation (even in low concentrations [8,24]. This is due to their large bandgaps in comparison to their bulk counterpart [8]. A study showed that the application of a heterogeneous structure $M_xBi_{2-x}Ti_2O_7$ where (M: Fe, Mn) nanocomplex enhances the photocatalytic activity and hence the degradation of methyl orange (MO) dye [9]. Also, Gd-doped PbSe nanoparticles [8], have shown high efficiency under visible light at 8% Gd content for the degradation of sulfasalazine (SSZ). This Gd content was found to be the optimum doping content with a bandgap of 2.8 eV in comparison to 4 (2.7 eV), 12 (2.5 eV), and 20% (4.7 eV) [8]. This indicates that the size of the bandgap is not, in fact, the main influencing factor in photocatalytic activity, as the high concentration of Gd ions cause further recombination and hence lower photocatalytic activity even with a larger bandgap.

Another semiconductor that was investigated lately is CuS doped with Ni ions giving an excellent photocatalytic activity through 98.46% efficiency at 3% Ni in the degradation of RhB dye [22].

c) *Plasmonic enhanced photocatalysis*: As mentioned before, one of the effective procedures to improve photocatalytic activity is the use of noble metals as a part of heterogeneous structure such as Au [11] and Ag [33,34] to generate SPR. It is well know that under irradiation of visible light or near infrared region, noble metals produce free electrons that resonate on their surface [35] and hence broaden the range of the absorbed irradiation [28]. In other words, when noble metals are irradiated with an electromagnetic wave, their conduction electrons will collectively oscillate and result in resonant scattering and absorption peak in the visible to the NIR region [35]. Recently, researchers focused on Ag nanoparticles (Ag NPs) as a superb photocatalyst owing to their low electronic bandgap that improves absorption beside SPR effect [21].

Photocatalytic activity of Ag NPs can be applied for the degradation of organic dyes from wastewater [21]. Very low absorption of MO dye was obtained after photocatalysis process, indicating a high degradation rate of the dye (94%) under UV irradiation. Ag NPs strongly absorb UV irradiation producing electrons on its surface that boosts photocatalytic effect [21]. Furthermore, Ag nanoparticles were successfully applied with TiO_2 in a gas-phase photocatalysis for acetaldehyde (an air pollutant) degradation [11]. TiO_2 NPs were coated with Ag (core–shell nanocomposite) to achieve more stable results. It was also shown from UV–vis absorption spectra that the absorption peak of the core–shell nanostructure can be controlled by changing the thickness of the Ag layer [11] (Figure 8.3b and 8.3c).

Moreover, Ag were involved in nanoparticle complex of Ag-AgBr/Al-MCM-41 for the adsorption of some toxic organic compounds from wastewater. It was shown that such complex showed a rapid adsorption of basic fuchsin (BF) compound in comparison with other complexes. This complex showed the highest absorbance in UV–vis absorbance spectra [28]. Moreover, SPR effect can be combined with surface-enhanced Raman scattering (SERS)

in order to monitor the reaction process by the real-time SERS spectrum and relate it to the photocatalysis results [34], which has significant importance for mechanism study and reaction condition optimization [34]. A general illustration of photocatalysis process including SPR effect is shown in Fig. 8.3d.

8.2.2 Factors Affecting Photocatalytic Procedure

During photocatalysis some factors can affect the surrounding medium and hence control the efficiency of the photocatalystic activity. This include pH [20,26,31], initial concentration [8], stirring rate [5], reaction, light yield, and distance between the light sources and the medium [5].

For Au-doped PdO tested in photocatalysis, it was found that the pH of the medium has a great influence on degradation of tetrodotoxin under UV irradiation (Figure 8.4a). As the pH of the medium was reduced from 11 to 5, the degradation efficiency significantly increased from 55 to 95%. This is due to the high number of OH ions generated in high pH medium that inhibits the production of some ROS that cause degradation [20]. Similarly, when TiO_2 nanospheres in photoelectrocatalysis were used for the adsorption of Cr(VI), adsorption efficiency increased from 65.4 to 100% when pH medium was lowered from 12 to 2. More hydrogen ions in low pH medium would help in the generation of more ROS that enhance adsorption. It is also concluded that lower pH medium also helps the heavy metal to adsorb around the surface of the photocatalyst [31]. On the other hand, other studies showed that higher pH of the medium is more suitable for photocatalysis [26]. In photocatalysis of TiO_2 at pH 11, tetracycline degradation reached 72% in comparison with 46% at pH 2. This was related to the production of ROS, too, as hydroxyl (OH) was predicted to be increased with increasing pH of the medium and hence boost degradation [26].

Moreover, it was proved that the initial concentration of the medium is very essential in assessing the photocatalysis activity. In the photcatalysis of Au-doped PdO NPs for the degradation of SSZ, it was shown that higher initial concentrations of SSZ resulted in less amount of degradation rate and vice versa (Figure 8.4b) [8].

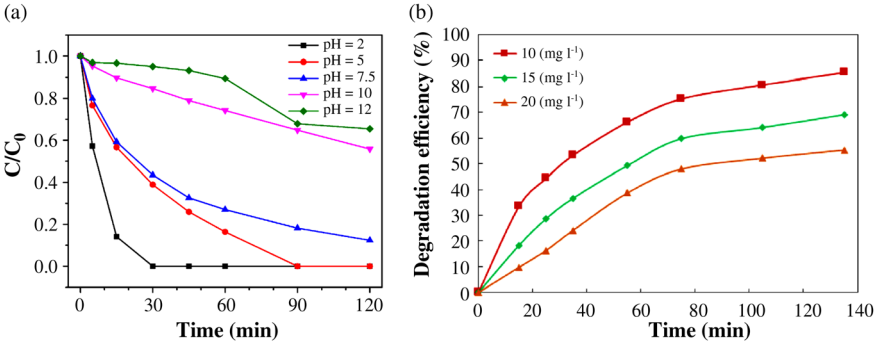

Figure 8.4 (a) Effect of the pH concentration on the TTX degradation (reproduced with permission from [20]. Copyright 2017, Elsevier) (b) The effect of initial concentration of the SSZ on the degradation efficiency. Experimental conditions: [8% Gd-doped PbSe]0 = 1 g l^{-1} (reproduced with permission from Ref. [8]. Copyright 2011, Elsevier).

8.3 Synthesis of Photocatalytic Materials

Numerous methods have been established in the synthesis of photocatalytic materials during the past decade because of their applications in processes such as wastewater and effluents treatment [36], which includes degradation of organic dyes [37] and volatile organic compounds [38], antimicrobial, antibacterial, and antioxidant activity [39], solar cell applications [40], photocatalytic self cleaning effect [41], hydrogen generation [42], food packaging [43], and biomedical and medical applications [44].

Numerous studies have explained that the intrinsic properties of photocatalytic materials can be effectively tailored by controlling their size, shape, composition, crystallinity, and structure. The growth of nanoscale materials rely on factors such as their thermodynamic and kinetic barriers in the reaction. It is also influenced by vacancies, defects, and surface reconstruction. Most synthetic methods for synthesizing nanomaterials use conventional heating due to the need for high-temperature-initiated nucleation followed by a controlled addition of precursor to the reaction.

The preparation of photocatalytic nanocomposite materials can be ideally divided into three main steps: (i) synthesis of an effective photocatalyst, (ii) its surface functionalization to enhance reactivity, and (iii) its incorporation in the most suitable host matrix according to the final application. Various methods have been developed for the synthesis of these property-tailored materials, which include hydrothermal, coprecipitation, sol–gel, ultrasonic impregnation, ionic liquid-assisted photochemical synthesis, electrochemical synthesis, solvotherml, facile chemical impregnation, microwave-assisted synthesis, and so on. In this section, recent progress in modern material science for the synthesis of photocatalytic materials, as well as advances achieved in their functionalization to tune their surface chemistry, will be presented and discussed. The next section focuses on the various nanoparticles that are employed in a wide range of applications of photocatalysis, see Figure. 8.5.

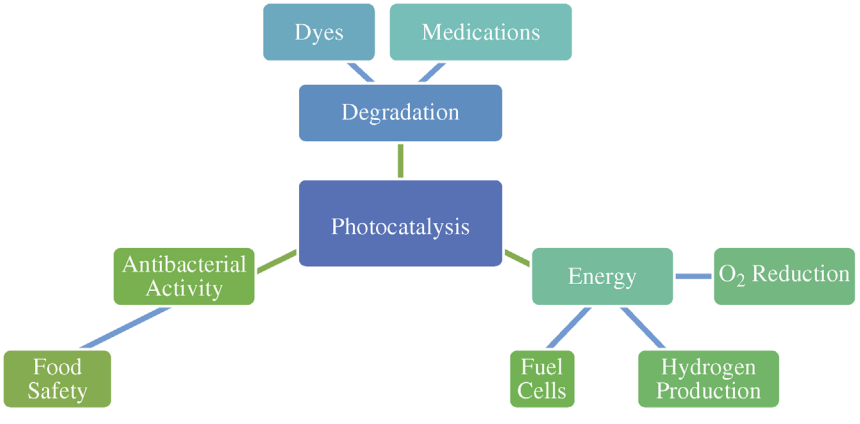

Figure 8.5 Photocatalysis applications of nanomaterials.

8.3.1 Hydrothermal Method

Hydrothermal synthesis has been identified as the most popular, gathering interest from scientists and technologists of different disciplines, particularly in the last 15 years. The word "hydrothermal" has geological origin, a self -explanatory word, "hydro" meaning water and "thermal" meaning heat [45].

This method is used to produce different chemical compounds and materials using closed-system physical and chemical processes flowing in aqueous solutions at temperatures above 100 °C and pressures above 1 atm [46]. It includes the ability to synthesize crystals of substances, which are unstable near the melting point, and large crystals of high quality. Substantial enhancement of synthesis by the use of additional external factors facilitates control of the reaction medium during the synthesis process. This approach is implemented in various options such as hydrothermal-microwave [47], hydrothermal-ultrasonic [48], hydrothermal-electrochemical [49], hydrothermal-mechanochemical [50], and hydrothermal-sol–gel [51].

A number of photocatalytic materials were synthesized by employing hydrothermal methods, including titania, silver, grapheme-based catalyst, cadmium and nickel sulfides, mixed metal oxide, rare earth metal oxides, and so on.

8.3.1.1 Titanium-based Photocatalyst

TiO_2 is a low-cost, nontoxic, and highly photostable material. Its photosensitivity, biological inertness, and unique optical properties make it very promising for the photocatalytic degradation of pollutants. However, photocatalysis on titanium dioxide is still limited by its UV band wavelengths (220–400 nm), and potentially limited photocatalytic activity can be expected in the visible spectral region or under solar irradiation (>290 nm) [52]; in addition, the low quantum yield due to the recombination of electron–hole pairs limits its practical application. Various attempts to limit this recombination have been reported, such as metal ion or nonmetal doping of the crystalline TiO_2, incorporation of noble metals in TiO_2 matrix, and composites with carbonaceous materials and other metal oxides [53].

Shixiong *et al.* have prepared TiO_2/graphene involving a two-step ultrasonic hydrothermal method. The precursor 1,3,6-trinitropyrene (TNP) was dispersed in an alkaline medium followed by the addition of TiO_2 and sonication. The hydrothermal reaction was performed in an electric oven, the resulting product was collected by filtering, and then washed and dried (Figure 8.6). The alkaline medium facilitates the intermolecular fusion of TNP onto the graphene transforming it to graphene quantum dots (GQDs) under mild hydrothermal conditions, envisaging a strong chemical interaction between TiO_2 nanoparticles and GQDs. The method generated uniform particle size with exclusive nanoparticles and almost defect-free graphene domains. GQDs content in TiO_2/GQDs is easily tuned by simply varying the addition amount of TNP precursor during the preparation process. By optimizing the amount of TNP, the photocatalytic H_2 evolution performance and photocurrent response of TiO_2/GQDs composite photocatalyst are enhanced [54].

Heterostructured photocatalyst of titanium was reported by Zhang *et al.* The authors succeeded in preparing $Bi_{12}TiO_{20}$-Bi_2WO_6 heterostructures by a facile

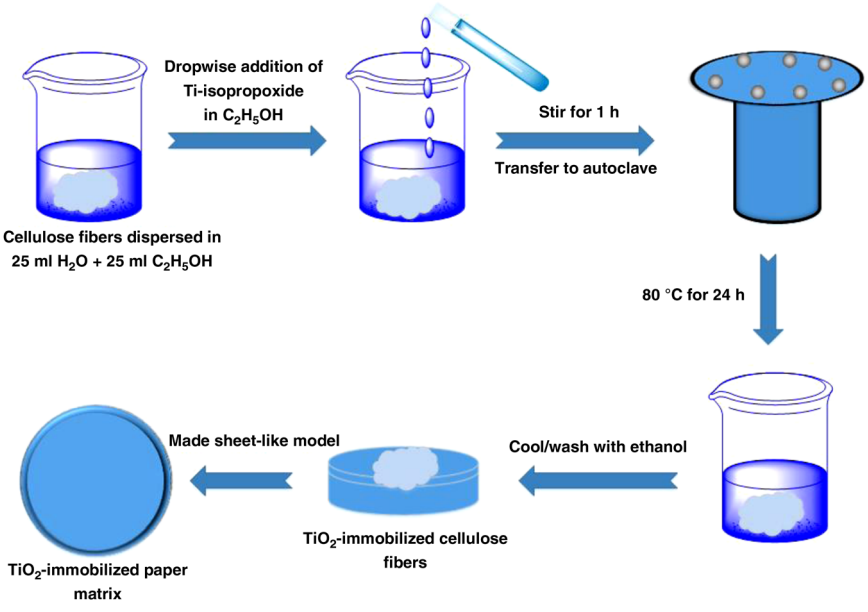

Figure 8.6 Schematic diagram of hydrothermal method of synthesis.

hydrothermal method. The morphology comprised of regular tetrahedrons and nanoflakes. The obtained heterojunction was found to posses higher photocatalytic ability for the degradation of RhB under exposure to UV–visible light [55].

Dispersion of gold (Au) NPs onto the surface of titanium oxide by hydrothermal method was reported by Malik *et al.* to prepare for obtaining a heterogeneous catalysts. A well-ordered 2D regular hexagonal porous nanostructure with long stripe-like channels was obtained characteristically. The presence of TiO_2 NPs in pore channels of SiO_2 assist in the homogeneous and uniform dispersion of Au NPs. The prepared catalysts show significant impact in enhancing the photocatalytic performance of Au–TiO_2/SiO_2 nanocomposite toward reduction of rose bengal (RB), methyl blue (MeB), RhB, and CR [56].

Many publications reported on doping (anion and cation impurities) and on developing TiO_2-based composites combining n–n semiconductors (TiO_2/SnO_2, TiO_2/ZnO, and TiO_2/WO_3) or *n–p* junctions (TiO_2/NiO_x,TiO_2/Cu_xS, and TiO_2/CuO_x), or by activating TiO_2 with noble metals (Pt,Pd, and Au/TiO_2) [57]. Other metal (Cr, Ni, Cu, and Nb) doped TiO_2 [58], fluorinated anatase TiO_2/reduced graphene oxide nanocomposites [59], silver (I) oxide/titanium dioxide heterojunctions [60], Li-doped $PbTiO_3$ perovskite [61] are also reported for various photocatalytic applications.

8.3.1.2 Silver-based Photocatalysts

Ag-based materials are identified as important photocatalysts because of transfer and separation of carriers [62], as well as better electrocatalytic activity [63]. The synthesis of Ag-based materials is of great interest to the scientific community

because of their numerous applications in catalysis, electronics, photonics, optoelectronics, sensing, and pharmaceuticals. The antibacterial activity of Ag NPs has been proven by various studies and consequently they have been incorporated into many commercial products. Due to their strong visible light-driven response, Ag-based semiconductors are utilized also as promising photocatalysts.

Most of the Ag-based semiconductors could exhibit high initial photocatalytic activity. But they suffer from poor stability because of the photochemical corrosion. Designing heterojunction, increasing specific surface area, enriching porous nanostructure, regulating morphology, controlling crystal facets, and producing plasmonic effects were considered as effective strategies to improve their photocatalytic performance. Combining the superior properties of carbon materials (e.g., carbon quantum dots, carbon nanotube, carbon nanofibers, and graphene) with Ag-based semiconductor has also produced high efficient composite photocatalyts [64].

A direct Z-scheme-type photocatalyst WO_3/Ag_3PO_4 composite (molar ratio 1 : 1, 1 W/1Ag) was prepared by Jinsuo *et al.* using hydrothermal method. SEM observations of Ag_3PO_4 at different magnifications, reveal large quantities of polyhedral particles with size of 10–15 m and high surface area. The edges and angles of the crystalline grains are regular and distinct, with some defects on the crystal surfaces, which act as active sites for the degradation reaction of methylene blue (MB) and MO organic dyes under visible light with a removal rate up to 95%. The enhanced performance of the catalyst was attributed to their relatively high surface area, strong light absorption, matched energy band structure, and the improved separation of photogenerated charge carriers between the two components [65].

Li *et al.* synthesized Ag^+-carbon dots (CDs)-Bi_2WO_6 ternary composite with excellent solar light-driven photocatalytic performance using hydrothermal impregnation method. The as-prepared catalyst exhibited uniformity in diameter without aggregation and micropores (0.5–2 μm). Ag^+-carbon dots (CDs)-Bi_2WO_6 displayed superior photocatalytic efficiency with nearly 100% removal of TC ($20\,mg\,l^{-1}$) in 20 min and 64% mineralization in 90 min [66].

Solar light-responsive $Ag/AgCl/WO_3$ photocatalyst was successfully synthesized by Adhikari *et al.* employing the microwave-assisted hydrothermal process. The composite photocatalyst has mixed morphology composed of rectangular plate-like and round-shaped WO_3 particles. AgCl NPs have an average diameter of 30 nm and possess two different morphologies: spherical and (some are) oval. Moreover, AgCl NPs are attached to WO_3 NPs and heterojunction is formed. The TEM image exhibits Ag NPs having diameter in the range of 10–20 nm in the composite. It is revealed that the distribution of Ag and AgCl nanoparticles in the composite photocatalyst is found to be heterogeneous, which is due to the hydrothermal treatment and it was carried out after the photoreduction of Ag NPs. The composite photocatalyst exhibited much higher photocatalytic activity compared to commercial WO_3 powder that can be ascribed to the surface plasmon resonance effect induced by Ag NPs. This work provides an insight into the further fabrication of $Ag/AgCl/WO_3$ composite system in order to obtain highly active visible light-responsive photocatalyst [67].

Numerous ternary metal oxide photocatalysts have been reported in literature, such as $AgVO_\beta$ [68], $AgMO_2$ (M = Al, Ga, and In) [69], Ag_2CO_3 [70], and Ag_3PO_4 [71] that have been found to exhibit enhanced photocatalytic performance under visible light irradiation (VLI), compared to the traditional TiO_2 photocatalyst.

8.3.1.3 ZnO-based Photocatalyst

ZnO is a versatile smart semiconductor that gained attention due to its wide range of technological applications in photocatalysis [72], field-effect transistors [73], chemical sensors [74], field emitters [75], transparent conductors [76], ultraviolet light emitting devices [42], and so on. Its importance in technological applications comes from its wide direct bandgap of energy 3.37 eV at room temperature and a large exciton binding energy of about 60 meV along with the electrical and optical properties of a II–VI semiconductor. ZnO has excellent thermal and chemical stabilities, a large piezoelectric constant, and an easily modified electric conductivity. The physical properties of ZnO are highly dependent on particle morphology, size, aspect ratio, orientation, and so on, which designs its technological applications. Consequently, significant scientific efforts have been devoted to the synthesis of shape-controlled ZnO nanostructures to explore its potential as a smart and functional material. Numerous nanostructured ZnOs with various morphologies have been fabricated, such as nanowires [77], nanosheets [78], nanotubes [79], and nanoflowers [80]. Controlled growth of hierarchical nanostructured ZnO has also received particular attention in the development of more complex structures.

Different flower-like ZnO nanoarchitectures were synthesized by Shuwang *et al.* adopting facile hydrothermal method and using CO $(NH_2)_2$ and N_2H_4 as alkali sources simultaneously. Ultralarge ZnO macroflower was constructed by the ultrathin leaf-like nanobelts and hollow semisphere-like, sphere-like, and apple-shaped NPs simultaneously. The diameter of an individual flower reaches 90 mm. Meanwhile, three or five flower-like ZnO nanostructures with different diameters, lengths, and tips (planar, semipyramid, and/or pyramid tips) are formed simultaneously under the same reaction condition. The photocatalytic activity and photocurrent strongly depend on the defect intensity of ZnO crystals and its unique morphology [72].

Şenay *et al.* synthesized ZnO and different noble and transition metals (Ni, Mn, Fe, and Ag) doped ZnO (M/ZnO) nanostructures by hydrothermal method. Results confirmed the formation of well-dispersed Ni and Ag NPs and highly agglomerated Mn and Fe NPs on the surface of ZnO nanostructures. The degradation rate of tartrazine was studied and obtained at a maximum rate of 98.2% in 60 min using Ni/ZnO. Doping transition metals may change the nucleation rate of ZnO and hydrothermal process is helpful for the growth of such hexagonal M-Zn-O nanorods. The metal atoms are both incorporated in ZnO lattice or substituted with some Zn atoms in ZnO lattice and dispersed or agglomerated onto ZnO nanostructure surfaces during the noble and transition metals doping process [81].

Core–shell ZnO/oxygen-doped g-C_3N_4 nanocomposite was prepared by Zheng *et al.* via hydrothermal method with the addition of hydrogen peroxide

(H_2O_2). The size of the prepared nano-ZnO is about 20~30 nm. The g-C_3N_4 nanosheets appear as loose and soft agglomerates with a dimension of 1~2 μm. Speculation is that the smaller ZnO NPs tend to form larger ZnO particles hydrothermal process. The size distribution of ZnO/oxygen-doped g-C_3N_4 does not show obvious changes when compared to pure nano-ZnO, indicating that the size of ZnO/oxygen-doped g-C_3N_4 NPs can be controlled effectively with the addition of hydrogen peroxide. In the process of hydrothermal reaction, g-C_3N_4 nanosheets were oxidized by hydrogen peroxide and then dehydration reaction occurs between C-OH groups to form the C-O-C groups, resulting in a relatively stable oxygen-doped g-C_3N_4 nanosheets wrapped on the surface of ZnO NPs. In the process of hydrothermal treatment, oxygenous groups were introduced to g-C_3N_4, which was helpful for the formation of core–shell nanostructure. Core–shell ZnO/oxygen-doped g-C_3N_4 architectures can provide a large interfacial area forming rapid charge separation and consequently increase the carrier separation efficiency. Oxygen-doped g-C_3N_4 NPs could also enhance the carrier separation efficiency and extend the range of light absorption. The photocatalytic performance of ZnO/oxygen-doped g-C_3N_4 NPs were found to be significantly enhanced [82].

8.3.2 Sol–Gel Processing

One of the most successful methods adopted for the synthesis of photocatalytic materials is the sol–gel processing route under appropriate experimental conditions. The sol–gel process involves the combination of chemical reactions that turns a homogenous solution of reactants into an infinite molecular weight polymer. This polymer is consisted of three-dimensional interconnected pores. The polymer is isotropic, homogeneous and uniform and it replicates its reactants exactly and miniaturizes all features without distortion. A variety of reaction conditions are employed for suitably architecturing the photocatalytic materials (Figure 8.7).

At present, the sol–gel method for processing materials is coupled with other distinctive methods of preparation in order to tailor the morphology and properties of the materials. For example, sol–gel hydrothermal [83], sol–gel-assisted electrospinning [84], sol–gel microwave [85], sol–gel ultrasonic [86], and so on. A variety of photocatalytic materials are synthesized by adopting the sol–gel method, which includes traditional titanium-based materials [87], ferrites [84], aluminum-doped materials [88], and so on.

8.3.2.1 Titanium-based Materials

Wenjie *et al.* prepared Al-In-codoped TiO_2 photocatalyst through the sol–gel method. The precursors were dissolved in ethanol, followed by the addition of tetrabutyl titanate and hydrochloric acid under continuous strring. The obtained gel was dried at 80 °C for 8 h and subsequently grounded and calcined at 400 °C for 3 h. The crystallite sizes of xAl–3% In-codoped TiO_2 samples with Al content ranging from 0.2 to 2% are 6.0, 5.7, 6.2, and 6.3 nm. Doping of Al and In within TiO_2 matrix hinders crystallization and agglomeration of TiO_2 crystals during the synthesis process. The codoped *x*Al-3%In-TiO_2 materials have improved adsorption capacity and photocatalytic activity [87].

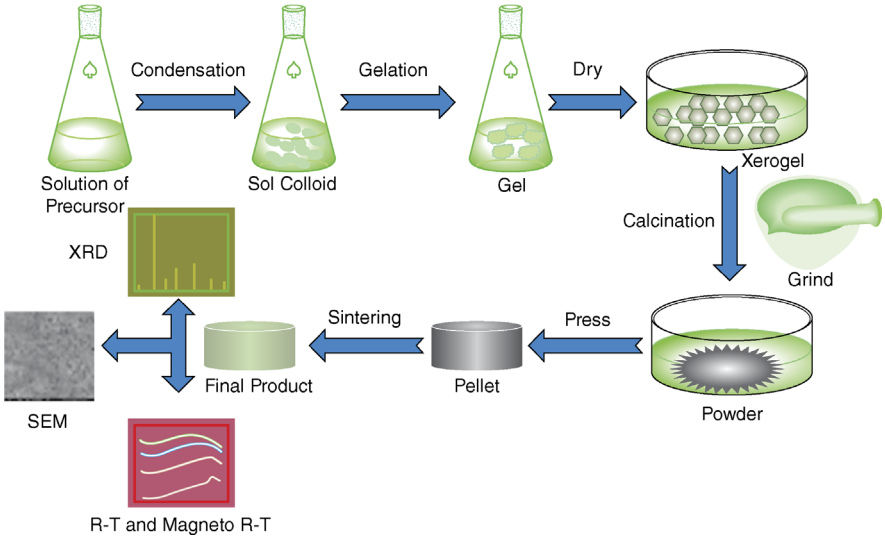

Figure 8.7 Schematic diagram of sol–gel method of synthesis.

An unusual sol–gel method utilizing novel and less chemical materials in addition to simple procedure was proposed by Masoud *et al.* to synthesize $ZnTiO_3$ nanostructures. Initially, the precursors along with chelating agents were dissolved in ethanol, stirred and kept in an oven at 60 and 70 °C, and finally grounded and calcined at 700, 800, and 900 °C for 3 h. A large number of separate, small and uniform particles were observed after calcination at 700 °C. It is found that the amorphous gel can be transformed into pure ilmenite-type $ZnTiO_3$ through calcination at 700 °C. The effect of pH on the growth process and morphology can be related to the formation of gel in sol–gel method. Since sol–gel method is a chain process, the synthesis of nanomaterials of quality and properties of the obtained product (gel) in this method depend on the intermediate steps. The most important steps for the formation of gel are prehydrolysis, hydrolysis, and polycondensation. At low pH, the effective density of H^+ ions in the sol is high and hydronium ions (H_3O^+) arises from the higher amount of H^+ ions, which prevents the hydrolysis and condensation process under low pH condition. Consequently, at the end of polycondensation process, the gel network resembles only to a linear polymer structure, leading to agglomeration and formation of larger aggregates. On the other hand, when the pH of sol is raised to 9, the effective density of H^+ ions is reduced, which causes an increase in the OH ions. The addition of NH_4OH (for increasing pH) also favors this process. As a result, the hydrolysis and polycondensation rates for the formation of gel are faster when the precursor sol is in higher pH [89].

Chunquan *et al.* has reported g-C_3N_4/TiO_2 hybrid photocatalysts synthesized through a modified sol–gel technique with varying the weight ratio of g-C_3N_4 under facile conditions. The g-C_3N_4 powder is dispersed in a mixture constituted by mingling ethanol with acetic acid and then stirred for 30 min. Second, TBOT (tetrabutyl titanate) was added in drops to the g-C_3N_4 suspensions under

continuous stirring. The pH was adjusted to lead the hydrolysis of TBOT at a moderate rate. The mixture was then stirred continuously for 12 h to immobilize TiO_2 colloids onto the bulk g-C3N4. Finally, the obtained product was dried in an oven at 105 °C for 12 h, followed by calcination (500 °C for 2 h in air, heating rate of 2.5 C min^{-1}). A mesoporous photocatalysts material is obtained with a pore size in the range of 2–10 nm, which is beneficial for the adsorption of contaminant molecules in water. The dispersivity of TiO_2 NPs deposited on the surface of g-C_3N_4 nanosheets is significantly improved. TiO_2 NPs in g-C_3N_4/TiO_2 become more dense and uniform and produce an excellent heterojunction effect, which would be beneficial for the transfer of photogenerated electrons and the improvement of photoactivity. g-C_3N_4/TiO_2 possesses an irregular lamellar structure, and the loaded TiO_2 NPs are uniformly and densely distributed without obvious aggregation on the surface of g-C_3N_4 nanosheets, which exhibits a good hybrid effect between g-C_3N_4 and TiO_2. The photocatalyst reveals a close interface between g-C_3N_4 and TiO_2 clearly by the facile sol–gel method [90].

8.3.2.2 Aluminum-based Materials

Aluminum-based photocatalytic materials exhibit superior strength, hardness, toughness, and coefficient of thermal expansion. Aluminum is the most commercially important simple metal. The overwhelming applications of aluminum-based materials are due to their superior physicochemical features. For example, Al_2O_3 has application in diverse fields ranging from medical, military, and industrial purposes. Aluminum (Al) nanomaterials act as drug delivery systems, which could encapsulate the drugs to increase solubility for evading clearance mechanisms and allowing the site-specific targeting of drugs to cells [91]. Al-based photocatalysts are found to be highly used in photoluminescence and photodegradation [88]. A few examples are discussed below.

Single-phase TiO_2-Al_2O_3-mixed oxides were successfully synthesized by the sol–gel method as reported by Young-Soo *et al.* [92]. XRD patterns and Raman spectroscopy confirmed that the addition of Al maintains the anatase phase. Samples with high Al content (more than 90%) remained amorphous even after calcination at 800 °C, and well-crystallized structures were achieved after calcination at 1000 °C. Phase transformation of pure titania from anatase to rutile was observed above 400 °C. When a small amount of Al was added; however, anatase phase was maintained even after calcination at 800 °C. The added Al seems to be highly dispersed and acts as a stability promoter for anatase phase. With the increase of Al content, pore size steadily decreased, resulting in the increase in surface area. BET surface area was found to be strongly dependent on composition, and all mixed oxides showed much higher surface area than either pure TiO_2 or Al_2O_3. The enhanced photocatalytic activity of mixed oxides was most probably due to the higher surface area and maintenance of anatase phase.

Mousumi *et al.* [88] reported facile synthesis of Al-doped ZnO-polyaniline hybrids by combining both sol–gel and *in situ* oxidative polymerization process. First, the precursors were dissolved in methanol and subjected to the sol–gel process at 60 °C for 2 h under magnetic stirring until a clear white gel was formed. The gel was cooled down to room temperature and kept for 24 h. The dried gel was calcined at 500 °C in air for 2 h. Then the chemical *in situ* oxidative

polymerization was adopted to prepare the ZnO–polyaniline hybrids. The morphology of nanostructured Al-doped ZnO (AlZnO) from TEM images showed nanorods with a diameter less than 100 nm. Superior photoelectrochemical performance and enhanced visible-light-assisted photodegradation of organic contaminants was obtained by the as-prepared Al-doped ZnO–polyaniline (PAZ) hybrid.

Mesoporous Al_2O_3 with a highest specific surface area was synthesized by the sol–gel method as reported by Tzompantzi *et al.* [93]. These mesoporous materials were found to have a shape of bottleneck interconnected. The materials dried at 100 °C and annealed at 400 °C show the highest specific surface area, while calcination over 400 °C shows a decrease in the specific surface area, from 412 $m^2 g^{-1}$ for the sample dried at 100 °C to 278 $m^2 g^{-1}$ for the sample calcined at 700 °C. The highest values of pore diameter correspond to materials calcined at 400 and 500 °C. This behavior is due to some internal changes in the material, that is, partial dehydroxylation during the calcinations processes. The study revealed that highly hydroxylated alumina, even after calcination over 600 °C, can be obtained by the sol–gel method. XRD Rietveld analysis indicated that sol–gel Al_2O_3 annealed at 400 °C presents an important deficiency in Al. The modification in Al—O bonds distances observed suggest the formation of point defects, which can be responsible for the photocatalytic activity of hydroxylated Al_2O_3. An important shift in the UV–vis absorbance to the visible region was observed in the sol–gel Al_2O_3 annealed at 400 °C. All of the sol–gel Al_2O_3 samples dried at 100 °C and annealed at 400, 500, 600, and 700 °C, respectively, were photoactive for the degradation of phenol.

8.3.2.3 Synthesis of Ferrite

Ferrite NPs have long been of much scientific and technological research interest due to their applications in electronics [94], magnetic recording media [95], ferrofluids [96], catalysis [97], and in gas sensors [98]. Significant research efforts have been made toward using these nanomagnetic particles as MRI contrast agent [99] and in drug delivery systems [100]. The physical and chemical properties of ferrite nanocrystals are greatly influenced by the synthesis route, and for this reason various approaches have been investigated. The sol–gel method is one of the simplest approach for the synthesis of ferrites.

$Ca_2Fe_2O_5$ nanofibers were synthesized by sol–gel-assisted electrospinning and calcined at 500 °C for 2 h, as reported by Xu *et al.* [84]. The diameter of all nanofibers after calcination exhibited shrinkage owing to the decomposition of PVP (polyvinyl pyrrolidone) and the formation of $Ca_2Fe_2O_5$ nanofibers. The nanofibers adhere well with each other. The surface of the sample appear porous in structure with an average diameter of 200 nm. Nanofibers after calcination are crushed into short belt-like fibers because fibers with larger aspect ratio could be formed following buckling with the increase of precursor concentration. The photocatalytic efficiency for the decomposing RhB solution is attributed to the effect of higher specific surface area, favouring increase in the number of active sites during photoreaction. TEM observations and pore-size distribution indicated a wide pore-size distribution, further confirming the presence of a large number of irregular pores. The BET surface area of the sample was found to be

38.28 m^2 g1. The large surface area for heterogeneous photocatalysis can provide more surface active sites for the adsorption of reactant molecules, making the photocatalytic process more efficient. This synthetic method may be extended to prepare other ternary metal oxides at relatively low temperatures. A rugby-shaped $SrFe_2O_4$/reduced graphene oxide (RS-$SrFe_2O_4$/RGO) composite with high photocatalytic activity was prepared by Danfeng *et al.* by adopting a ultrasonic-assisted sol–gel route [84]. The precursor metals along with the gelling agent citric acid are dissolved in double-distilled water solution under vigorous stirring at 60–70 °C. The molar amount of citric acid added is equal to that of $Sr(NO_3)_2$ in the solution. The citric acid helps the metal ions to get dispersed in homogeneous solution. Ehylene glycol is used as dispersant and stabilizer. The pH value of the mixture was adjusted to pH 3 by using $NH_3{\cdot}H_2O$. After stirring for 30 min, thiourea was added. A gel-like precursor was obtained by using ultrasonic irradiation for 1 h at 80 °C, then heated and burned to form a loose powder. Finally, the as-obtained powder was subjected to calcination at 700 °C for 8 h (6 °C min^{-1}). The morphological observations showed a uniform rugby geometrical shape with an average length of 1 μm and a diameter of 500 nm. RS-$SrFe_2O_4$ was distributed uniformly on the surface of reduced graphene oxide (RGO) nanosheets and an enhanced photocatalytic activity for RS$SrFe_2O_4$/RGO is observed by this unique method of synthesis [86].

8.3.3 Microwave Method

Microwave (MW) heating method can address the problem of heating inhomogeneity. It is well known that the interaction of dielectric materials, liquids, or solids, with microwaves leads to dielectric heating [101]. The use of MW irradiation provides increased reaction kinetics and rapid initial heating, which results in enhanced reaction rates. This also provides energy efficiency by reducing the reaction time from hours to minutes compared to conventional heating methods, which culminates in clean reaction products and higher yields. By judiciously choosing the solvents and reactants, the precursors can be selectively heated to produce specific nanostructures. As a result, the use of MW irradiation as an efficient, environment-friendly, and economically viable heating method for the production of nanomaterials has increased significantly. Even household microwave ovens have been used to prepare nanoparticles [102]. Coupled synthesis such as microwave hydrothermal synthesis [47], microwave solvothermal synthesis [103], and microwave sol–gel synthesis [86] are also reported. Hereafter, the synthesis of various photocatalytic materials, such as grapheme-based materials, Zn-based, and Ti-based materials in photocatalysis under MW irradiation conditions will be presented. Application of these nanomaterials in catalysis is also reviewed (Figure 8.8).

8.3.3.1 Graphene-based Materials

Graphene has a unique atom-thick two-dimensional (2D) structure, high conductivity, and charge mobility, huge specific surface area, excellent mechanical, thermal, and electrical properties. Thus, it has been regarded as an important component for functional materials, especially for developing a variety of

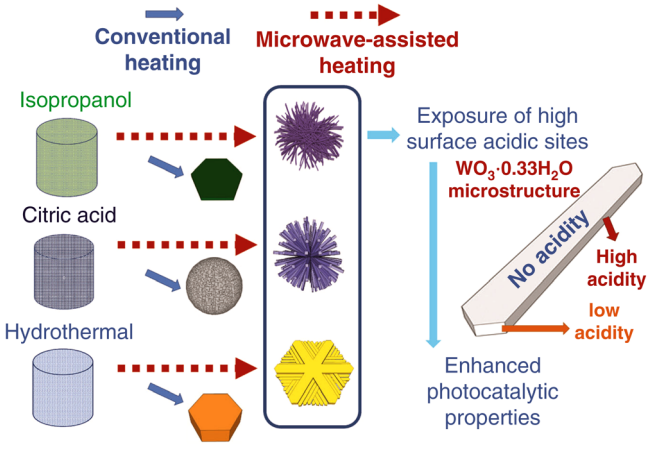

Figure 8.8 Schematic diagram of microwave synthesis approach (reproduced with permission from Ref. [104]. Copyright 2013, Royal Society of Chemistry).

photocatalysts. Hence, the recent advancements in synthesizing graphene-based new photocatalysts, and their applications are summarized.

A facile, fast, and scalable microwave irradiation (MWI) method for the synthesis of Ag NPs dispersed on graphene sheets were developed by Qiang *et al.* Graphene oxide is prepared from natural flake graphite powder by a modified Hummers' method. The reactants are dispersed into absolute ethanol, with ultrasonication for 1 h, and further magnetically stirred for 6 h. The slurry thus obtained is placed in a microwave oven under cyclic MWI (30 s on for every 30 s interval) for several cycles at 800 W. Cyclic microwave radiation is employed instead of continuous one to avoid bumping. The resulted suspension is subjected to centrifugation, washed, and then dried at 60 °C in vacuum for 24 h. Ag nanoparticles with tens of nanometers are uniformly deposited on the surface of GO sheets. Ag ions are introduced via the strong cooperation with the terminal oxygen-containing functional groups on the GO nanosheets. During the microwave treatment, the hydrolysis of Ag ions occurs through deoxidization as well as the reduction of GO. As a result, Ag NPs are attached onto the surface of GO. The existence of Ag NPs is evidenced by XRD. The corresponding rGO–Ag nanocomposite is found to exhibit extraordinary higher catalytic properties for the degradation of RhB. And it is clear that the microwave cyclic time has a significant effect on the photodegradation of rGO–Ag nanocomposite for RhB. This is associated with the thermal reduction of GO, which promotes the photogenerated electron transfer, due to the lower energy level of thermally reduced GO. Further increase in the microwave cyclic time led to a poorer photodegradation performance, which is ascribed to serious oxidation of partially reduced GO [105].

Darvishi *et al.* [106] has demonstrated an easy, fast, and low cost MWI approach for the preparation of CuO/graphene (CuO/G) hybrid composite, which includes dispersion of CuO/graphene-oxide hybrid, followed by MWI reduction. Initial GO is prepared by the improved Hummers' method, involving the ultrasonic bath where GO is dissolved in a mixture of water/ethanol until a

homogeneous yellow solution of graphene oxide of preferred concentration was obtained. Then, CuO (93 wt% relative to GO) was added to the above solution under stirring for 2 h and the suspension was placed inside a microwave oven (720 W) for 9 min to reduce CuO/graphene oxide into CuO/graphene (CuO/G), centrifuged, washed several times with distilled water, and finally dried. The study revealed nanoparticles of copper oxide having an average size of ~13.50 nm with monoclinic structure. Photocatalytic performance of CuO/G hybrids studied by degradation of MB under UV irradiation indicates that CuO/G hybrid is an effective photocatalyts for degradation of MB [106].

8.3.3.2 Zinc-based Materials

Zinc oxide (ZnO) nanoparticles were synthesized by Supattra *et al.* using crude water extract of *Psidium guajava* Linn leaves and MWI. As a general procedure, the crude extract was mixed with zinc (II) aqueous solution. Four different zinc salts, that is, $Zn(CH_3COO)_2$, $ZnSO_4$, $ZnCl_2$, and basic carbonate form of $ZnCO_3$, were used. The synthesis was carried out using a household microwave oven operating at 720 W for varying cycles of 3 min on and 1 min off. The samples chosen for the photocatalytic studies were ZnO NPs yielded from the reaction conducted for 45 cycles and treated at 900 °C. ZnO NPs showed excellent surface area and efficient photocatalytic activity toward the degradation of organic dyes [107].

A crystalline, hexagonal wurtzite ZnO nanowire was grown by Solis *et al.* [108] using a microwave-assisted thermal decomposition. The process consists of an hourglass-shaped reactor within a conventional microwave oven. For a typical reaction, a ceramic container with ZnO precursor material powder homogeneously mixed with graphite is placed in the center of the MATD (microwave-assisted thermal decomposition) device. The mixture is placed in an oven for 2 h at 100 °C in order to remove moisture from the material. After introducing the sample in the center of the microwave, it is covered with the inner container and the oxygen flow begins. The maximum reaction time was 3 min and the reaction powers used in different experiments were 1200, 1000, 600, and 100 W. The container with the precursor material is placed in a ceramic plate fixed in the same place in the oven and the sample is not rotated during the synthesis process. After the reaction, four samples were collected from different zones of the reactor. The as-obtained NWs presented a tetrapod shape with diameters between 20 and 100 nm and presented irregular shapes with some thinner and wider parts. ZnO NWs can be grown independently on certain substrates. However, vertically aligned growth on a substrate has more advantages for photocatalytic applications. The anisotropy of the ZnO crystal structure assists the growth of NWs.

8.3.3.3 Titanium-based Materials

Caudillo *et al.* reported MWCNT/TiO_2 heterojunction photocatalysts synthesized by microwave-assisted process using titanium butoxide as a precursor and ethanol as solvent. All the precursors are dissolved in ethanol and the suspension was subjected to irradiation in a commercial microwave reactor for 20 min at 120 °C and thermally treated at 400 °C for 1 h. Morphological studies revealed smooth nanotubes of different lengths with an average diameter of 75 nm. It is

also observed that the CNTs decorate the photocatalyst surface. The surface junction between TiO_2 and MWCNT is confirmed by TEM analysis. The average crystallite size is on the order of 10 nm. This investigation demonstrates that the microwave-assisted method leads to MWCNT/TiO_2 heterojunction photocatalysts with higher photoactive properties for environmental applications [109].

Synthesis of hierarchical TiO_2 microspheres as catalytic materials based on a simple microwave-assisted solvothermal process of titanium glycerolate intermediate precursor is reported by Prince *et al.* [110]. In a typical experimental procedure, 18 ml of glycerol was mixed with 36 ml of ethanol with stirring. After few minutes, 3.0 mmol of titanium isopropoxide was slowly dropped into the mixture solution with stirring to form a homogeneously transparent solution for 2 h in a closed container at room temperature, the final mixture solution was transferred into the microwave irradiation flask. The flask made of polytetrafluoroethylene can be heated by microwave to a maximum allowed pressure and temperature of 5 MPa and 260 °C, respectively. The mixture was sealed tightly and then heated to 180 °C at 600 W power and held for 0.5–2.5 h. After it was cooled to room temperature naturally, the TiO_2 products were collected by centrifugation and washed thoroughly three times at least with anhydrous ethanol and deionized water. Subsequently, the obtained samples were dried in an oven at 60 °C overnight. Finally, to remove the residual organics and promote further crystallization, the dried sample was annealed at 550 °C for 2 h in a muffle furnace (2 °C min^{-1}) before being used as a catalyst. In addition, the glycerol dosage in the precursor solution was adjusted, while keeping the total volume unchanged and the same preparation procedure and conditions, to control the morphology of the final products. It was found that only after the introduction of titanium precursor into the microwave-assisted solvothermal system maintained at 180 °C for 15 min, spherical intermediate products were obtained. Small nanosheets grown randomly on the surface of the as-obtained microspheres as observed. XRD patterns demonstrated the amorphous nature of the as-prepared products. When the reaction time was prolonged to 45 min, the nanosheets transformed into typical nanoribbons. When the reaction time was further increased to 90 min, these building unit nanoribbons grew continuously in length. The complete hierarchical microspheres with sharp 18 nanoribbons building units were formed, and the size became relatively uniform around 4.0 μm in diameter. Moreover, the synthesis of these hierarchical microspheres produced more homogeneously distributed and more uniform shapes than those prepared in shorter time. With the further prolongation of reaction time to 150 min, the building units transformed from nanoribbons to nanowires, leading to the formation of final hierarchical microspheres consisting of nanowires. The obtained hierarchical TiO_2 microspheres possess tunable building units, high specific surface areas, and improved optical performance [110].

8.3.4 Coprecipitation Method of Synthesis

Coprecipitation reactions involve the simultaneous occurrence of nucleation, growth, coarsening, and/or agglomeration processes. The products are generally insoluble species formed under conditions of high supersaturation. Nucleation is

the key step and a large number of small particles will be formed. Secondary processes, such as Oswald ripening and aggregation, dramatically affect the size, morphology, and properties of the products.

8.3.4.1 Silver-based Catalyst

Ghanbari *et al.* [111] prepared Ag_2CdI_4/AgI nanocomposites by *in situ* coprecipitation method from aqueous solutions of Cd $(NO_3)_2{\cdot}2\,H_2O$, $AgNO_3$, and $LiI{\cdot}2\,H_2O$ as starting materials. AgI yellow precipitation is prepared from $AgNO_3$ and $LiI{\cdot}2\,H_2O$ in 50 ml of distilled water and then certain amount of capping agent (CTAB, SDS, Triplex, NaHSal, and PVP) is added to the above solution. CdI_2 white precipitate is obtained from $Cd(NO_3)_2{\cdot}2\,H_2O$ with stoichiometric amount of $LiI{\cdot}2\,H_2O$ (by considering the desired molar ratio of Ag^+ to Cd^{+2} in different experiments). Finally, the solution consisting of AgI is added to CdI_2 solution and heated at 90 °C for drying. The reaction conditions in this method are easily controllable. The molar ratio of Ag^+/Cd^{+2} and type of capping agent have an influence on components, purity, and size of nanocomposites. The calculated bandgap confirms that Ag_2CdI_4 nanoparticles can be used as effective photocatalysts. Photooxidation tests show that degradation reached a high value of 96.6% after 100 min irradiation of UV light [111].

8.3.4.2 Zinc-based Catalyst

Three different coprecipitation methods, namely, decreasing pH method, constant pH method, and increasing pH method, were adopted by Hu *et al.* [112] to synthesize wurtzite zinc-gallium oxynitrides (ZnGaNO) particles by nitridation of $Zn/Ga/CO_3$ layered double hydroxides (LDHs). The obtained particles are found to be a ZnO/ZnGaNO composite, a single-phase ZnGaNO, and a porous $ZnGaNO/ZnGa_2O_4$ composite, respectively. Precipitation processes determine the microstructure of $Zn/Ga/CO_3$ LDHs and thereby affect the photocatalytic performance of final ZnGaNO particles.

Precursor solutions: A mixed aqueous solution with 0.4 M $Zn(NO_3)_2{\cdot}6\,H_2O$ and 0.3 M $Ga(NO_3)_3{\cdot}9\,H_2O$ is prepared to give a metallic nitrate solution (solution A) with $[Zn^{2+}]/[Ga^{3+}]$ mole ratio of 4: 3. 2 M NaOH and 1 M Na_2CO_3 are mixed to form a base solution (solution B).

Decreasing pH method: Solution A (100 ml) is added quickly to 1 M Na_2CO_3 solution (70 ml) with vigorously stirring at 40 °C. After complete delivery of the mixed nitrate solution, the pH of the reaction mixture is adjusted to 8 using 2 M NaOH solution. The reaction mixture is aged at 80 °C for 12–2 h with thorough stirring. The product suspension is then repeatedly centrifuged and washed with deionized water. The precipitate is dried at 70 °C for 24 h.

Constant pH method: Solutions A and B are simultaneously added in drops to a vessel containing stirred deionized water while maintaining a pH of 8. The mixing process is carried out at 40 °C. After complete delivery, the reaction mixture is aged at 80 °C for 12–24 h with good stirring. The product suspension is centrifuged and washed and dried at 70 °C for 24 h.

Increasing pH method: Solution A (100 ml) is mixed with 100 ml of 1 M HNO_3. Solution B is then added in drops to the mixed solution until the pH reached at 8. During the titration process, the solution is stirred vigorously at

40 °C. The reaction mixture is aged at 80 °C for 12–24 h with good stirring. The product suspension was then centrifuged, washed with deionized water, and the precipitate was dried at 70 °C for 24 h. The nitridation process was carried by heating 1.5 g Zn/Ga/CO_3 LDH powders at 800 °C under a NH_3 flow of 120 ml min^{-1} for 30 min.

The photocatalytic performance decreased in the order of decreasing pH sample, constant pH sample, and increasing pH sample. The superior photocatalytic activity of the decreasing pH sample was attributed to the ZnO/ZnGaNO heterostructure which enhances the separation of photogenerated electron–hole pairs and produced a large amount of $O^{2-\bullet}$ radicals and holes h^+ as main active species to degrade phenol and its intermediates. The facile synthesis of ZnO/ZnGaNO particles makes it a potential efficient visible-light-responsive photocatalyst for water pollutant degradation [112].

8.3.4.3 Ferrite Catalysts

Highly crystalline, single-phase spinel $ZnFe_2O_4$ nanoparticles were synthesized by Vinosha *et al.* [113] using coprecipitation technique. $ZnCl_2$ and $FeCl_3$ were dissolved separately in distilled water and well stirred till homogenization was attained. NaOH solution as mineralizer was added in drops to $FeCl_3$ solution under continuous stirring in order to adjust the pH of the solution to 10. Finally, $ZnCl_2$ solution was added to the above solution and the temperature was raised to 80 °C for 3 h until a brown precipitate was obtained. The precipitate was centrifuged with distilled water and ethanol. The by-product thus obtained was annealed at 75 °C for 24 h in a hot air oven followed by calcination at 500 °C for 5 h. The size distribution for the synthesized sample was found to be approximately 8.2 nm. Nanoparticles usually form when the growth rate is lower than the nucleation rate. The size can be tailored by the annealing temperature. Here, the agglomeration of the nanoparticles has been controlled by regulating growth rates and nucleation during the synthesis. Ferrite materials have received considerable attention due to their electrical and magnetic properties [113].

8.3.4.4 Titanium-based Catalysts

Quan *et al.* [114] prepared lanthanide-doped titanium dioxide photocatalysts by a coprecipitation process. It was found that Ln^{3+}–TiO_2 photocatalysts prepared by coprecipitation exhibited an excellent photocatalytic activity compared to those prepared by the usually used sol–gel process. The photocatalysts prepared by the coprecipitation and sol–gel process have a similar crystal composition, but the former catalysts have more regular anatase phase with a larger crystallite size, thereby leading to a difference in their photocatalytic activity. The pores in the sol–gel prepared catalysts are in the range of mesopores (2–50 nm), whereas the pores in the catalysis prepared by coprecipitation consist of larger mesopores and macropores (>50 nm). The morphology of the primary particles and agglomerates of Ln^{3+}–TiO_2 catalyst powders are affected by doping methods. The inhibition effect of lanthanide doping on the phase transformation is greater in the coprecipitation process than in the sol–gel process, which is related to the more uniformly dispersed hydroxides of lanthanide in the precursors to form Ln^{3+}–TiO_2 catalysts. This finding is beneficial for preparing more regular

crystalline Ln^{3+}–TiO_2 catalysts with anatase structure and larger crystallite size by annealing at higher temperature.

8.3.5 Solvothermal Synthesis of Photocatalytic Materials

This method is favorable for the preparation of a variety of materials such as metals, semiconductors, ceramics, and polymers. The process involves the use of a solvent under moderate to high pressure (typically between 1 atm and 10 000 atm) and temperature (typically between 100 and 1000 °C) that facilitate the interaction of precursors during synthesis. If water is used as the solvent, the method is called "hydrothermal synthesis." The synthesis under hydrothermal conditions is usually performed below the supercritical temperature of water (374 °C). The process can be used to prepare many geometries including thin films, bulk powders, single crystals, and nanocrystals. In addition, the morphology (sphere (3D), rod (2D), or wire (1D)) of the formed crystals is controlled by manipulating the solvent supersaturation, the concentration of chemical of interest, and kinetic control. The method can be used to prepare thermodynamically stable and metastable states including novel materials that cannot be easily formed from other synthetic routes (Figure 8.9).

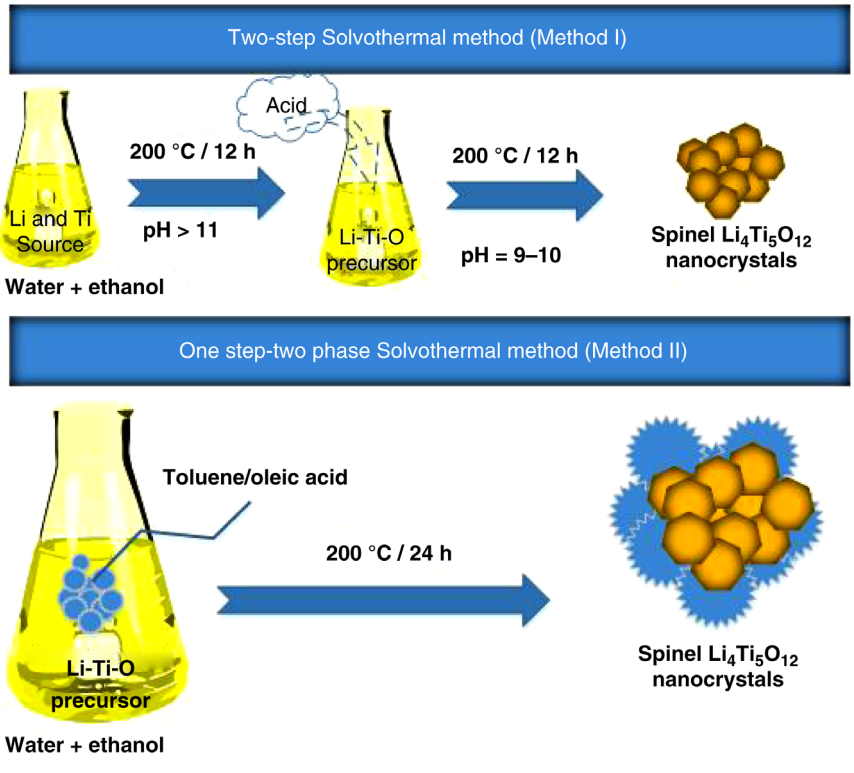

Figure 8.9 Schematic Diagram of Solvothermal synthesis method.

8.3.5.1 Copper-based Materials

Copper is an essential element that is widely distributed in fresh water and sea [115]. It has outstanding characteristics such as high electrical and thermal conductivity and corrosion resistance. Oxides of copper have narrow bandgap with various applications such as heterogeneous catalysts, gas sensors, optical switches, magnetic materials, and so on [116]. Copper complexes act as catalysts for homogenous photooxidation of hydroxylic organic substrates (very often pollutants) [117]. The yield of oxidation products strongly depends on the composition of copper complexes, which offers the possibility of useful control and tailoring of copper catalysts properties [118]. The presence of Cu in addition to another reactant can lead to enhancement of the pollutant photodegradation.

For the first time flower-like Cu_2MnSnS_4 nanoparticles were synthesized by Guan *et al.* [119] using a solution-based solvothermal method. Higher magnification of the prepared catalyst revealed the thickness of the petal to be 40 nm, which is formed by agglomeration of small nanocrystals with grain sizes of about 10 nm, which is in accordance with the value obtained by XRD analysis. It is observed that the rough surface of the petal increases the surface areas that has a great effect on photocatalytic activity. Cu_2MnSnS_4 nanoparticles form through homogeneous nucleation and growth process, while nanosheets are formed through oriented aggregation. Then, nanosheets attach to flower-like particles through self-assembly process for prolonged solvothermal reaction. The Cu_2MnSnS_4 nanocrystals was found to degrade about 85% of the methylene blue within 240 min under visible-light irradiation, suggesting it to be a potential candidate for visible-light photocatalyst for the treatment of wastewater from pollutants [119].

Facile solvent thermal synthesis was adopted by Wang *et al.* [120] to synthesize a series of cocoon-like hierarchical structures of *x*Cu-$BiVO_4$ photocatalysts using ethylene glycol with ethylene diamine tetraacetic acid (EDTA) as a chelating agent. Initially, $Bi(NO_3)_3{\cdot}5\,H_2O$ was dissolved in ethylene glycol. The mixture was subjected to stirring and NH_4VO_3 was added. After consecutive stir addition of EDTA, ammonia was added to maintain a pH of 11. Then different contents of Cu $(NO_3)_2{\cdot}3\,H_2O$ were added into these suspensions with continuous magnetic stirring and transferred into 100 ml Teflon-lined stainless autoclave and heated at 180 °C for 10 h. Now, the autoclave was cooled at room temperature, and the yellow precipitates thus formed were filtered and washed with absolute ethanol and distilled water for several times and dried at 80 °C in air for 12 h to obtain $BiVO_4$ with different Cu^{2+} doping contents. It was found that the amount of Cu^{2+} has no effect on the crystal phase of $BiVO_4$ but plays an important role in the morphology; the catalysts turn from rodflower-like particles into cocoon-like hierarchical nanstructures due to Cu^{2+} doping. It indicated that a large number of irregular particles are connected together to form the cocoon-like morphology. The results showed that Cu^{2+} doping effectively enhances the photocatalytic activity of the $BiVO_4$ evaluated by the degradation of RhB under visible-light irradiation. The improvement of photocatalytic activity is associated with the change of morphology, the enhancement of light absorption, narrowing bandgap, and lowerimg recombination ratio of photo-induced electron–hole pairs [90].

Wei *et al.* [121] synthesized hierarchical structures of Cu_2SnSe_3 microspheres by solvothermal method using ethylenediamine as solvent. SEM images show a 2D nanosheet pattern. When the hydrothermal temperature was raised to 150 °C, the bulk particles disappeared, leaving only 2D nanosheets. When the temperature was further increased to 200 °C, uniform 3D microspheres, consisting of 2D nanosheets, were harvested. Ethylenediamine plays an important role in the formation of Cu_2SnSe_3 crystals. Two amino groups in the ethylenediamine structure are strong chelating groups, which not only provide reaction sites in the naosheet formation but also 3D microsphere self-assembly. Solvothermal temperature is an important factor for providing high-pressure environment for crystal growth. The high solvothermal temperature (150 °C) provides an appropriate condition for Cu_2SnSe_3 crystal nanosheet formation, when increasing the temperature to 200 °C, the formed 2D nanosheet self- assemble to form a 3D microsphere structure with the ethylenediamine ligand [121].

8.3.5.2 Titania-based Catalyst

Zdravkov *et al.* [122] prepared mesocrystalline anatase TiO_2 particles by solvothermal sol–gel method using aliphatic organic acids at various temperatures of 250, 300, and 350 °C. The size and shape of the primary crystallites are controlled by varying the synthesis temperature and hydrocarbon chain length of organic acid molecules. The obtained anatase crystallites tend to agglomerate in aqueous solutions and exhibit enhanced photocatalytic activity. Titanium tetraisopropoxide is dissolved in acetic acid and the solution is placed in a silver vessel, which, in turn, is placed in a steel autoclave (internal volume 65 ml) and heated for 6 h at 250, 300, or 350 °C. The precipitates formed are separated by centrifugation, washed with petroleum ether, acetone, and ethyl alcohol, and dried under argon. All samples contain residual organics that were removed after the thermal post-treatment and complementary chemical treatment with KOH [122].

8.4 Phase Transition and Microstructure of Photocatalytic Materials

Changes in structure and properties accompanying phase transitions have been of great importance to scientists for many years. With changing pressure and temperature conditions, particularly sintering temperature, the material experiences several phase transitions that affect their physical properties owing to structural changes in the crystal lattice and to the absorption or release of latent heat. It is accompanied by significant variations in the physical properties such as density, phase transitions, and mechanical behavior. Phase transitions often lead to mechanical softening or hardening that can be related to different intrinsic mechanical behavior and volatile solubility of the product phases [123]. Crystalline solids undergoing phase transformation display fine-scale microstructure that in turn plays an important role in determining the macroscopic properties of solids. Hereafter, we try to understand the various phase transitions in

photocatalysts, their activity, and the role of lattice parameters in determining the microstructure and consequently the macroscopic properties.

The best component to study the phase transitions during photocatalysis is TiO_2, since it has been widely used as photocatalyst for over three decades. Titania photocatalysts are known to be applicable in a range of important technological areas such as electrolysis of water to generate hydrogen [124], dye-sensitized solar cells (DSSCs) [125], air purification [126], water treatment [127], self-cleaning coatings [128], nonspotting glass [129], and self-sterilizing coatings [130]. Titania is also used to catalyze many reactions, such as alcohol dehydration, photo-Kolbe oxidations of organic acids [131], oxidation of aromatic compounds [132], degradation of paint pigments [133], and nitrogen oxide reduction [134] under UV illumination.

8.4.1 Formation and Analysis of Titania Phases

During the synthesis of TiO_2 films by various methods, the initial crystalline TiO_2 phase formed is generally anatase [135]. From a structural perspective, this could be due to the short-range ordered TiO_6 octahedra in arranging into long-range ordered anatase structure owing to the less-constrained molecular construction of anatase relative to rutile [136] (Figure 8.10). Alternatively, from a thermodynamic perspective, the more rapid recrystallization of anatase could be due to the lower surface free energy of this polymorph, despite the lower Gibbs free energy of rutile [137]. That is, the higher surface free energy of rutile crystallites may favor the crystallization of anatase. It should be noted that it is possible to form rutile under near-room temperature conditions [138]. Hydrothermal methods of synthesis, which can facilitate the precipitation of crystalline TiO_2 directly

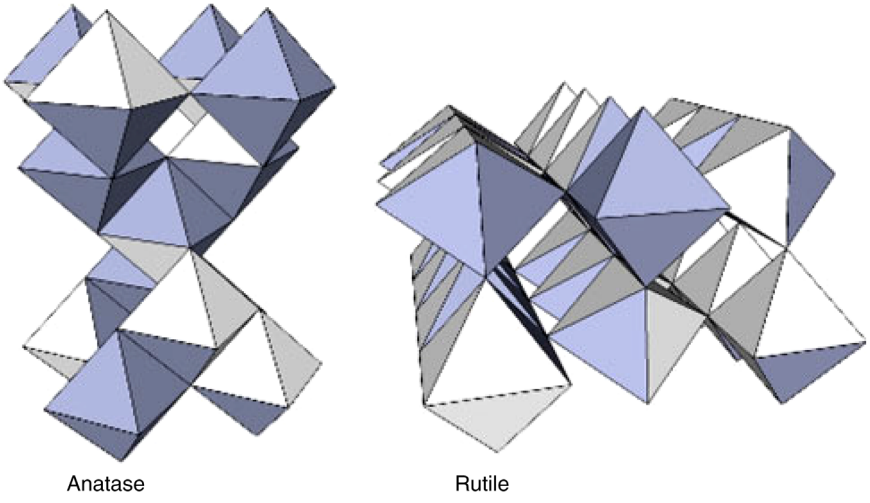

Figure 8.10 Three-dimensional representation of the arrangement of TiO_6 octahedra in anatase and rutile showing four-edge sharing connectivity in anatase and two-edge sharing connectivity in rutile (reproduced with permission from Ref. [136]. Copyright 1976, Elsevier).

from a liquid phase, can be controlled to precipitate rutile. Aside from this method, rutile is obtained only through high-temperature treatment.

8.4.2 Anatase to Rutile Transformation

Controlling the conditions that affect the kinetics to control the transformation of anatase to rutile phase is of considerable interest. This is particularly the case for high-temperature processes and applications, such as gas sensors and porous gas separation membranes [139], where the phase transformation may occur, thereby altering the properties and performance of these devices. Therefore, an understanding of the stabilities of the TiO_2 polymorphs, the kinetics of their phase transformation, and the processes involved in controlling them is essential to the ability to obtain single-phase or multiphase microstructures. These issues are critical to the long-term consistency of devices, where retention of anatase or a multiphase microstructure may not be possible, thereby potentially requiring processing designed to produce single-phase rutile. Similarly, limitations in temperature while desiring a specific polymorph, such as rutile, may require manipulation of the materials and processing conditions so as to enhance the direct formation of rutile. The generation of the phases of TiO_2 depends significantly on the synthesis parameters, which in turn affect the product. The kinetics of these processes typically are considered in terms of temperature and time. In terms of the former, pure bulk anatase is considered widely to begin to transform irreversibly to rutile in air at 600 °C [140]; however, the reported transition temperatures vary in the range 400–1200 °C [141] owing to the use of different methods of determining the transition temperatures, raw materials, and processing methods. The anatase to rutile transformation is not instantaneous; it is time dependent because it is reconstructive [142]. Consequently, the kinetics of the phase transformation must be interpreted in terms of all of the factors that influence the requisite temperature–time conditions. These parameters for undoped anatase include particle size, particle shape (aspect ratio), surface area, atmosphere, volume of sample, nature of sample container, heating rate, soaking time, impurities (from raw materials and container), and measurement technique. The anatase-to-rutile phase transition, sometimes referred to as "ART", usually occurs by nucleation and growth process [143]. As mentioned by Penn. *et al.*, the kinetics of this transition depend on variables such as impurities, morphology, sample preparation method, heat flow conditions, and so on.

8.4.3 Morphological Effects

The grain morphology plays an important role in photocatalytic applications of titania. Nanocrystallinity has been shown to lower the material's densification temperature and enhance its photocatalytic activity. Therefore, it is important to inhibit the grain growth of titania during heating as this gives a higher surface area and thus improved performance. Bulk rutile is more stable thermodynamically than anatase at all temperatures and pressures (Figure 8.11) owing to its lower free energy [144]. However, the lower surface energy of the anatase planes relative to those of rutile [137] cause the former to be more stable for crystallites of

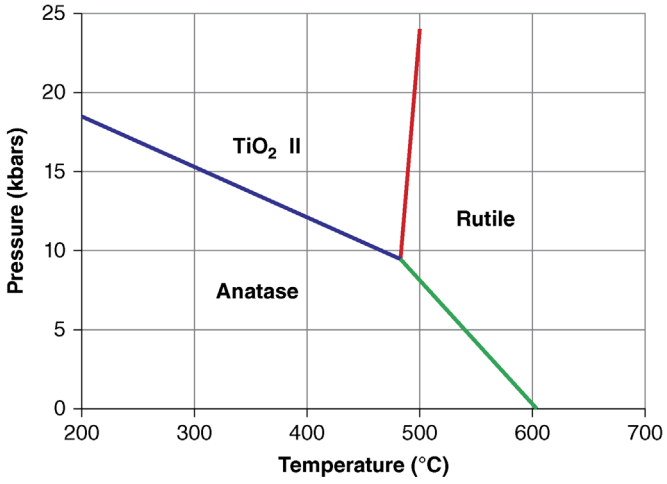

Figure 8.11 Reaction boundaries of phase transitions in TiO_2 (reproduced with permission from Ref. [148]. Copyright 2000, Elsevier).

extremely small sizes and correspondingly high surface area. In this case, surface energy consideration outweighs bulk thermodynamics and so, for crystallites below a critical size (45 nm [110], 14 nm [137], and 11 nm [145]), anatase has a lower total (bulk and surface) free energy [144]. Further, the size above which rutile becomes more stable depends on stresses [137]. Despite this, it has been reported that larger anatase grains (i.e., predominantly bulk thermodynamics) transform to rutile more slowly than finer grains (i.e., predominantly surface thermodynamics). This is probably due to the lower surface energy and fewer interfaces at which rutile can nucleate. Thus, the transition to rutile and grain growth of anatase can be considered as competing phenomenon [146]. Significant rutile grain growth is exhibited as the anatase to rutile transition proceeds [103]. Rutile grains coarsen at the expense of neighboring anatase during coalescence until the large rutile grains begin to impinge on each other [147]. This increase in grain size causes a decrease in surface area and a consequent decrease in photocatalytic activity [148].

8.4.4 Phase Transition Studies of Orthorhombic Bi_5O_7I Spherical Microstructures

Orthorhombic phase Bi_5O_7I spherical microstructures were successfully fabricated by Han *et al.* [149] through thermal conversion of BiOI microspheres in air at temperatures ranging from 450 to 525 °C. The BiOI-450 sample exhibited a higher photocatalytic activity for the degradation of RhB in aqueous solution under light irradiation compared to other samples and retained its relatively high photocatalytic activity even after eight cycles. The porous Bi_5O_7I microspheres fabricated in this study are readily applied as a photocatalyst for environmental remediation. At 400 °C, both BiOI and Bi_5O_7I phases are present. From 425 to 525 °C, the BiOI was fully converted to the orthorhombic phase Bi_5O_7I, indicating

that the Bi_5O_7I can be obtained from the BiOI precursor at lower temperatures. XPS wide scan spectra of the samples indicate the presence of bismuth (Bi 4f, Bi 4d, Bi 4p, and Bi 5d), oxygen (O 1 s), iodine (I 3d), and carbon (C 1 s). The observed shift of binding energies confirms the complete phase transition from BiOI to Bi_5O_7I after heat treatment at 450 °C. SEM and TEM show spherical microstructures assembled by numerous ultrathin nanosheets. For all BiOI powders, the spherical shape is maintained and their diameters slightly decreased from 3 to1.5 mm, while the thickness of the sheet-like nanostructures increased. TEM image of a single Bi_5O_7I microsphere heat treated at 450 °C confirms it is composed of nanosheets of a thickness of about 25 nm. HR TEM image reveals that the two different lattice fringes with intervals of about 0.317 and 0.306 nm can be assigned to (312) and (113) planes of the orthorhombic phase Bi_5O_7I, respectively. The BiOI-400 sample showed the higher adsorption property with RhB that is attributed to its large surface area, unique surface, and surface electronegativity (see Figure 8.12) [149].

8.4.5 Phase Transition Studies of Bicrystalline Cr-TiO_2 Nanoparticles

Employing one-step flame spray pyrolysis technique, Tian *et al.* [150] synthesized bicrystalline phase Cr-TiO_2 nanoparticles. The mixed phases of TiO_2, such as anatase/rutile and anatase/brookite, exhibit higher photocatalytic activity than pure single-crystal phase. The enhanced activity of mixed phases is attributed to the formation of heterojunction between different phases, which can efficiently separate the spatial charges and consequently improve the quantum yield of TiO_2. The intimate contact between two phases is necessary to enhance the

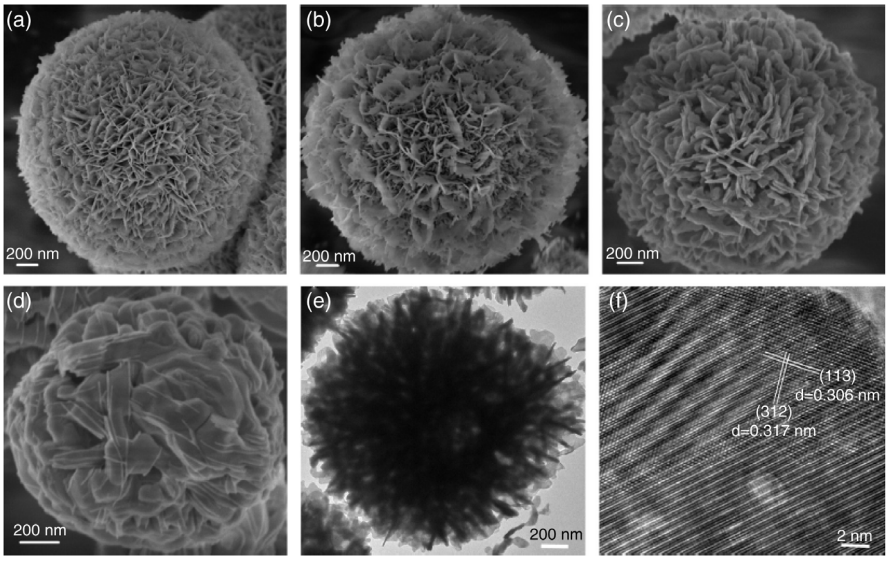

Figure 8.12 SEM images of pure (a) and heat-treated BiOI powders at 400 (b), 450 (c), and 500 °C (d). TEM (e) and HRTEM (f) images of the BiOI powder heat treatment at 450 °C (reproduced with permission from Ref. [149]. Copyright 2016, Elsevier).

photocatalytic activity of mixed-phase TiO_2. Small rutile crystallites are found to interweave with anatase crystallites to facilitate efficient electron transfer at anatase/rutile interface. Research has proved that there is an optimum ratio between the two phases to enhance the photocatalytic activity. In this study, the XRD patterns confirm both the crystalline nature of different Cr-TiO_2 samples and the presence or absence of segregated Cr oxides. All samples consist of anatase and rutile, and the intensity of rutile (1 1 0) peak increases gradually with the increase in Cr content, with the decrease in anatase (1 0 1) peak. No characteristic peak of Cr incorporation into the crystal lattice of TiO_2 is reported; rather, Cr oxide is highly dispersed and its size is very small. It has been considered that metal dopants can be conveniently incorporated into TiO_2 lattice when their ionic radii are identical or close to that of the Ti^{4+} cation. The phase composition (anatase and rutile) in the samples is estimated from the respective peak intensity of anatase (1 0 1) and rutile (1 1 0) with the following equation:

$$\mathrm{WR} = \mathrm{AR}\,0.884\mathrm{AA} + \mathrm{AR}\,(\mathbf{1}),$$

where WR represents the weight fraction of rutile and AA and AR are the integrated intensities of anatase (1 0 1) and rutile (1 1 0) peaks, respectively.

The content of rutile increases from 9.2% for undoped TiO_2 to 63.4% for 5% Cr-TiO_2 (Figure 8.13), indicating that Cr^{3+} doping can effectively promote the

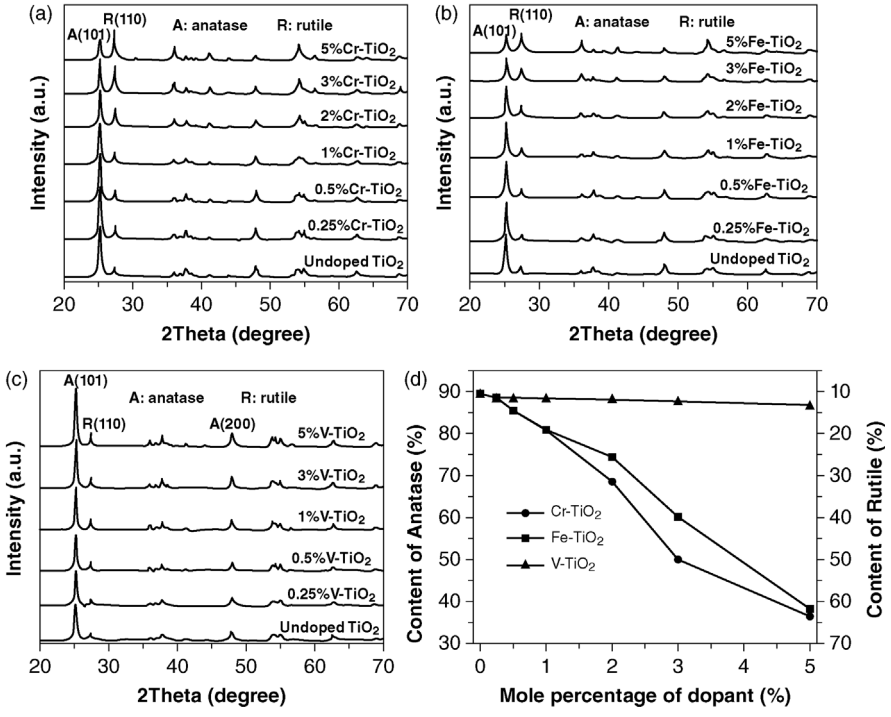

Figure 8.13 (a–c) XRD patterns of Cr-TiO_2 (a), Fe-TiO_2 (b), and V-TiO_2 (c). (d) Content evolutions of anatase and rutile as a function of doping amount (reproduced with permission from Ref. [150]. Copyright 2012, Elsevier).

formation of rutile and simultaneously restrain the formation of anatase, that is, Cr doping favors the anatase-to-rutile transformation of TiO_2. The average crystallite size of anatase and rutile is found not influenced by Cr doping. It has been reported that in the hot-wall and flame reactors trivalence Fe^{3+} or Al^{3+} doping can create oxygen vacancies in TiO_2 matrix, which is favorable to anatase-to-rutile transformation. To explore the influence of the valence state of metal dopant on the crystal transformation in flame spray reaction, Fe-TiO_2 and V-TiO_2 were prepared by using $Fe(AcAc)_3$ and $VO(AcAc)_2$ as trivalent and tetravalent dopants, respectively. For Fe-TiO_2, the intensity of rutile (1 1 0) peak appreciably increases with the increase in Fe content, similar to that of Cr-TiO_2. In the case of V-TiO_2, the intensity of rutile (1 1 0) peak only shows a slight increase, together with the increase in anatase (1 0 1) peak. It can be seen that Fe^{3+} and Cr^{3+} doping appreciably promotes the anatase-to-rutile transformation of TiO_2, while V^{4+} doping almost has no influence. Cr^{3+} ions incorporated into TiO_2 crystal lattice can extend the visible light absorption of TiO_2, consequently improving the visible light photocatalytic activity of TiO_2. However, too high Cr content is detrimental to the improvement of visible light photocatalytic activity, because both Cr_2O_3 clusters and excess rutile content favor the recombination of photogenerated electrons and holes. The optimal Cr^{3+} content corresponding to the highest photocatalytic activity was found to be 1% [150].

8.4.6 Phase Transition Studies of N, S, and C Co-Doped TiO_2 Nanomaterials

Lei *et al.* [151] discussed the effect of calcination temperature on the structure and visible-light photocatalytic activity of (N, S, and C) codoped TiO_2 nanomaterials. XRD of NSC-TiO_{2-x} shows peaks corresponding to anatase phase, with no indication of any rutile or brookite impurity being detected. As the calcination temperature increases from 400 to 700 °C, the peak intensity of anatase (1 0 1) increases; meanwhile, its width of (1 0 1) plane becomes narrow, which is attributed to gradual crystallization of anatase TiO_2. The average crystallite size of pure TiO_2-500, NSC-TiO_2-400, NSC-TiO_2-500, NSC-TiO_2-600, and NSC-TiO_2-700 is 34.1, 10.1, 14.4, 26.1, and 32.5 nm, respectively. This indicates that t (N, S, and C) codoping could efficiently inhibit grain growth. Compared to NSC-TiO_2-500, TiO_2-500 reveals a small amount of rutile, which means that N, S, and C as codoping elements retard the anatase–rutile transformation. It is also evident from TEM and HRTEM images that NSC-TiO_2-500 has round-shaped particles in the range of 10–20 nm, which is consistent with the calculated value (14.4 nm) obtained from XRD. HRTEM image shows that the interplanar spacing is about 0.35 nm, which corresponds to (1 0 1) plane of anatase TiO_2. Doping anatase TiO_2 with N, S, and C could not only broaden the light adsorption spectrum into the visible region (>400 nm) to make it visible-light active but also inhibit the recombination of photo-induced carriers to make it more efficient under visible light irradiation. NSC-TiO_2-500 exhibited the highest photocatalytic activity for Cr(VI) photocatalytic reduction under visible-light irradiation, which can be attributed to the synergic effect of its enhanced crystallinity. The outstanding photocatalytic performance of NSC-TiO_2-500 makes it a promising photocatalyst in efficient utilization of solar energy for Cr(VI) wastewater treatment [151].

8.5 Optical and Magnetic Properties

Nowadays, various types of photocatalytic semiconductors, including binary, ternary, quaternary, and composites are extensively investigated in order to enhance their photocatalytic activities [152–157]. Photocatalytic activity is closely related to the optical absorption ability and the migration of the photogenerated electron–hole pairs. Optical properties can be evaluated by UV–visible diffuse reflectance spectrum (UV–vis DRS) and photoluminescence (PL) spectra. The bandgap of the photocatalyst can be estimated by following Tauc plot: $(\alpha h\upsilon)^{1/n} = A(h\upsilon - E_g)$, where α is absorption coefficient, $h\upsilon$ denote incident light frequency, A proportionality constant, E_g – bandgap, $n = 1/2$ for direct transition, and $n = 2$ for indirect transition [158]. By extrapolating $(\alpha h\upsilon)^{1/n}$ linearly to zero, the bandgap energy can be calculated. Many binary compounds have been classified as semiconductors, but not all are suitable for photocatalytic applications. An appropriate semiconductor for heterogeneous photocatalysis must fulfill the following characteristics: appropriate bandgap (in the range of 1.7–3.2 eV), efficient light absorption, high carrier mobility, precise band edge positions that straddle the water redox potentials, nontoxic, and chemically stable [159].

To describe mechanistically the enhanced photocatalytic activity of semiconductor nanocomposites under visible-light irradiation, the corresponding conduction band and valence band positions for each semiconductor component can be estimated at the point of zero charge by the following equations:

$$E_{CB} = X - E^e - 0.5E_g,$$

$$E_{VB} = E_{CB} + E_g,$$

where X, E^e, and E_g are the absolute electronegativity, energy of free electrons on the hydrogen scale (4.5 eV), and the bandgap energy of the semiconductor, respectively [160].

The association of two or more nanocrystalline semiconductors allows the design of novel semiconductors heterostructures that are potentially useful in photocatalysis, water splitting, microelectronics, and other applications [161–163]. The advantage of using associations of semiconductors is twofold: (1) to extend the photoresponse by coupling a large bandgap semiconductor with a short bandgap semiconductor (coupled semiconductors heterostructures) and (2) to retard the recombination of photogenerated charge carriers by injecting electrons into the lower lying conduction band of the large bandgap semiconductor (capped semiconductors heterostructures) [159]. The mechanism of charge separation in coupled and capped semiconductors is similar, but the interfacial charge transfer is notably different. In a *coupled semiconductor* system, the particles are in contact with each other and the holes and electrons are available for oxidation or reduction reactions on the surface of different particles. In *capped semiconductors* with a core–shell structure, a charge rectification takes place, and only one of the charge carriers is accessible at the surface; the other charge carrier gets trapped inside the inner semiconductor [159].

More examples of coupled semiconductors have been reported not only by coupling TiO_2 and metals or semiconductors but also in composites containing

titanium dioxide with other oxides, including WO_3 [164,165], CeO_2 [14,166], and ZnO [167–171]. This section discusses in detail the optical and magnetic properties of different semiconductor hybrid heterostructures and the various approaches by which the photocatalyst can be modified. The use of the composite materials is also taken into account.

8.5.1 MeNPs–Semiconductor Hybrid Heterostructures

Two-component hybrid nanostructures based on the combination of a metal-oxide semiconductor and noble metal nanoparticles (MeNPs) have been widely investigated in photocatalysis due to their unique physical and chemical properties. Metal–semiconductor hybrid structures show absorption spectra exhibiting combined coupling effects that cannot be replicated with a simple physical mixture of both components. In these hybrid structures, strong coupling occurs between the electronic states of metal and semiconductor, which leads to broadening and shifts in the plasmonic peak of the metal and the excitonic absorption peak of the semiconductor. This could be a result of the formation of new electronic states in the semiconductor–metal interface [172].

ZnO and TiO_2 have been extensively investigated as a photocatalysts because of their abundant source, nontoxicity, and low cost. It is well known that ZnO is an environment-friendly semiconductor with a direct bandgap of 3.37 eV; however, the quick recombination of the photoexcited electrons and holes in ZnO always leads to a decline in the photocatalytic efficiency [173]. The enhancement of photocatalytic efficiency can be achieved by the deposition of a layer of noble metal nanoparticles (MeNPs), such as Pt [174–177], Au [173,178–180], or Ag [167–171,174,176], on the surface of ZnO or TiO_2 nanostructures. Noble metals act as an electron sink, which can significantly enhance the photocatalytic activity in both UV and visible lights [181]. Noble metal NPs have the ability to absorb the visible light via surface plasmon resonance and are used to improve the charge separation and photocatalytic activity. Different approaches have been reported to prepare MeNPs–ZnO(or TiO_2) heterostructures and to study their photocatalytic properties [167–181].

8.5.1.1 Au–ZnO Hybrid Photocatalysts

Li *et al.* [180] have successfully synthesized Au–ZnO hybrid NPs with a novel hexagonal pyramid-like structure (Figure 8.14), which demonstrated a better photocatalytic efficiency than pure ZnO nanocrystals in the photocatalytic degradation of rhodamine B dye.

Wu *et al.* [182] fabricated close-packed Au/ZnO hollow-sphere monolayer thin films using PS spheres as a template (Figure 8.15a). The Au/ZnO hollow-sphere monolayer thin films showed significant enhancement of photocatalytic performance in the degradation of methyl orange compared to that of ZnO thin film and ZnO hollow-sphere monolayer thin films (Figure 8.15b). The observed degradation constant k of MO for the Au/ZnO 400 nm was $0.0415\,min^{-1}$, which is approximately 17 times better than that of ZnO thin film ($0.0024\,min^{-1}$) and 3 times that of the ZnO 400 nm ($0.0128\,min^{-1}$).

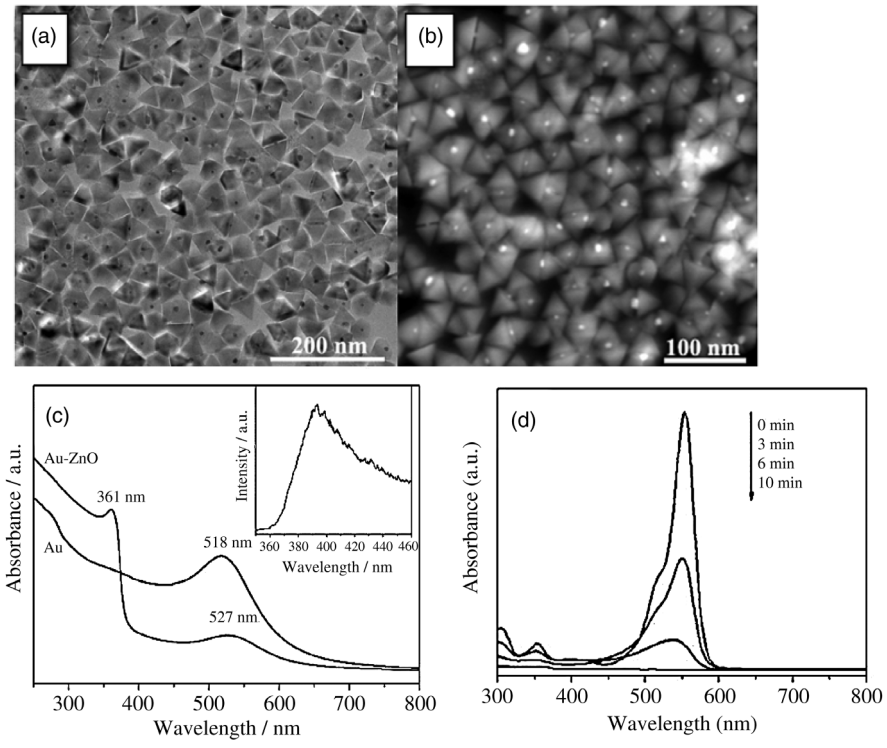

Figure 8.14 Au-ZnO hybrid nanopyramids and their optical properties. (a) TEM image of Au-ZnO NPs; (b) HAADF-STEM image of Au-ZnO NPs; (c) UV–vis absorption spectra of Au and Au–ZnO hybrid NCs dispersed in hexane, respectively; (d) time-dependent UV–vis absorption spectra for RhB in the presence of Au–ZnO hybrid NPs under UV irradiation (reproduced with permission from Ref. [180]. Copyright 2011, American Chemical Society).

The composite of Au/GO/ZnO nanostructures synthesized by Lee *et al.* [183] showed a photodegradation efficiency of 81% for methylene blue (Figure 8.16). Au/GO/ZnO reveals a better UV light absorption and more quenched PL emission than ZnO and GO/ZnO. PL emission is often used to investigate the recombination of photoexcited electron–hole pairs in ZnO. A band edge emission at 382 nm indicates that the bandgap of ZnO is 3.25 eV. As can be seen in Figure 8.16a, the intensities of GO/ZnO and Au/GO/ZnO are significantly reduced in comparison to ZnO and Au/GO/ZnO that have the lowest PL emission intensity, which demonstrates that Au/GO/ZnO is a promising hybrid photocatalyst. The Au/GO layer acts as an electron sink that is an additional approach for separating charge carriers [183].

8.5.1.2 Ag–ZnO Hybrid Photocatalysts

Andrade *et al.* [5] synthesized ZnO/Ag hybrid nanostructures with a star-shaped morphology by a novel and simple room-temperature method with enhanced photocatalysis and bactericide applications. The presence of thiocyanate on ZnO surface prevents uncontrollable growth of Ag NPs into different morphologies (such as nanosphere, nanorod, and nanoplates) and high degrees of polydispersity

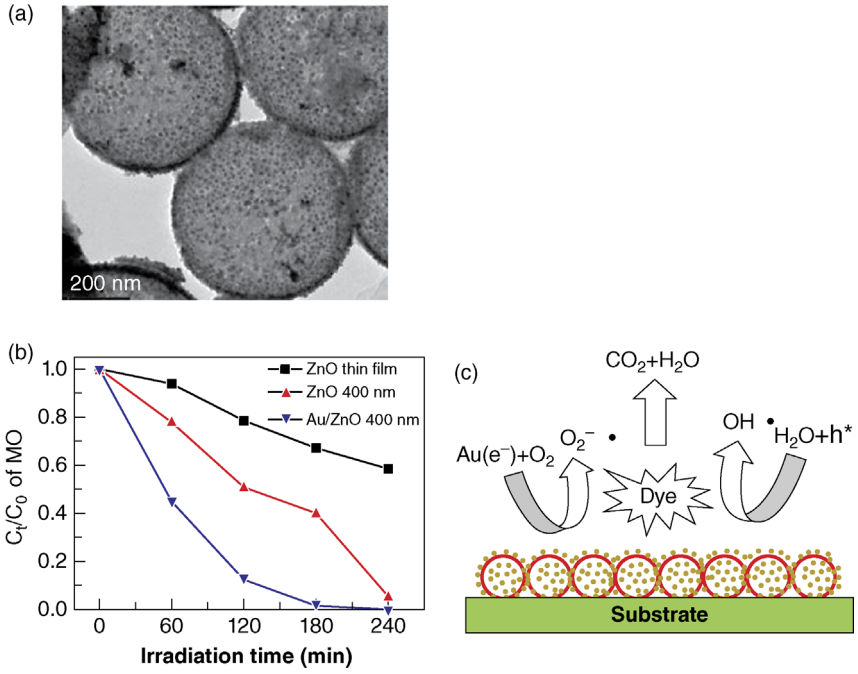

Figure 8.15 Au/ZnO hollow-sphere monolayer thin films and their photocatalytic properties. (a) TEM images of Au/ZnO spheres; (b) degradation rates of MO on the Au/ZnO 400 nm, ZnO 400 nm, and ZnO thin-film samples; (c) schematic illustration of the mechanism for the photocatalytic degradation of MO on the Au/ZnO photocatalyst (reproduced with permission from Ref. [182]. Copyright 2017, from Elsevier).

(Figure 8.17a). The optical properties of hybrid ZnO/Ag studied by UV-vis NIR and PL spectroscopies show that the sample ZnO(t)/Ag0.05 presents the higher photocatalytic activity, which degrades 70% of MB dye following 60 min of UV light exposure, whereas pure star-shaped ZnO degrades only 25% of MB for the same exposure time (Figure 8.17b).

Different Ag–ZnO hybrid heterostructures with enhanced photocatalytic activity were reported in the literature including Ag/ZnO [169,170], Ag/ZnO/graphene oxide [167], Ag/ZnO/graphene [168], Ag/AgCl/ZnO nanonetworks [171], Ba@Ag@ZnO nanocomposite [184], ZnO/Ag/Ag_2WO_4 [185], and so on.

8.5.1.3 Pt–ZnO Hybrid Photocatalysts

Hu *et al.* [186] prepared Pt–ZnO hybrid nanocomposites by solution plasma technology. They synthesized 2–3 nm Pt NPs that were dispersed on a pyramid-like ZnO (20–60 nm) surface. Photodegradation of RhB dye demonstrates that the Pt (5 wt%)–ZnO hybrid nanocomposite has a better photocatalytic activity than commercial P25, because Pt NPs restrain the photogenerated electron/hole recombination and increase the catalyst activity. Pt(5wt%)–ZnO nanocomposite can completely degrade 10 ppm RhB aqueous solution in 25 min. The

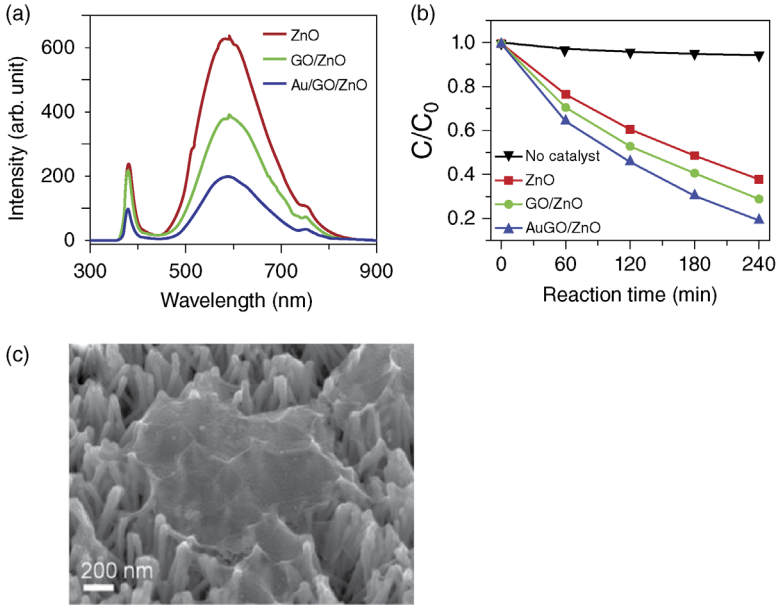

Figure 8.16 Au/GO/ZnO composite nanostructures. (a) PL spectra of ZnO, GO/ZnO, and Au/GO/ZnO; (b) photocatalytic performance of ZnO, GO/ZnO, and Au/GO/ZnO under UV irradiation; (c) SEM image of Au/GO/ZnO after photocatalytic reaction (reproduced with permission from Ref. [36]. Copyright 2017, Elsevier).

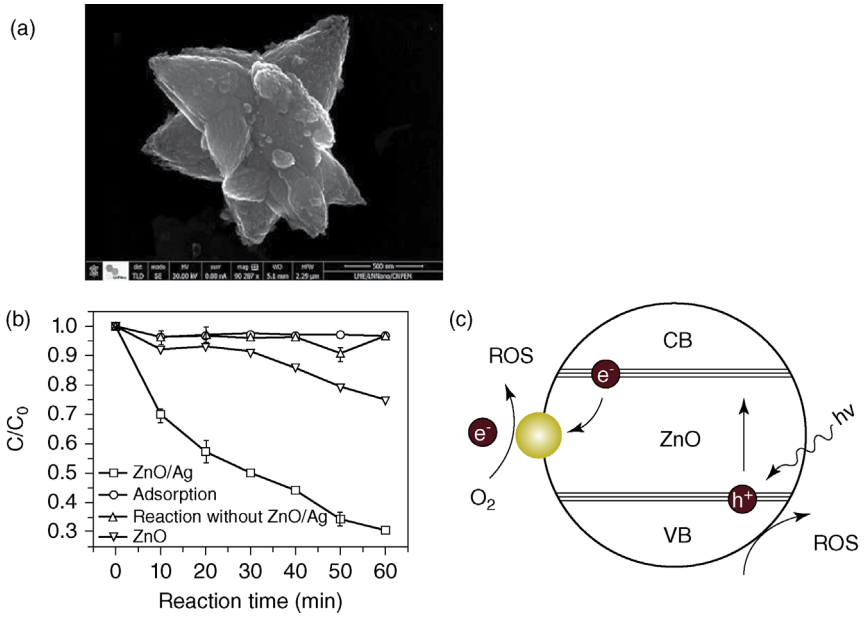

Figure 8.17 Star-shaped ZnO/Ag hybrid nanostructures: (a) SEM image of sample ZnO(t)/Au0.2; (b) photocatalytic degradation efficiency of ZnO(t)/Ag0.05; (c) proposed mechanism of electron transfer in hybrid ZnO/Ag photocatalyst and electron capture by Ag NPs for the formation of reactive oxygen species, which cause degradation of MB dye (reproduced with permission from Ref. [5]. Copyright 2017, Elsevier).

photocatalysis enhanced mechanisms of Pt–ZnO hybrid nanocomposite has been proposed.

Pt–ZnO hybrid photocatalysts also have been investigated for evaluation of their activity in the degradation of organic dyes [174,176], hydrogen production by photocatalytic water-splitting [175] and phenol degradation [177], and so on.

8.5.1.4 Me–TiO_2 Hybrid Photocatalysts

TiO_2 is well known as an excellent UV-responsive semiconductor for efficient photocatalysis for environmental applications including photocatalytic hydrogen generation and pollutant removal [152]. TiO_2 has large electronic bandgap in the range 3.0–3.2 eV, which restrict its optical absorption mainly to the UV region, corresponding to less than 4% of natural solar energy. This is why big efforts have been devoted to improving the visible-light absorption of TiO_2. In order to improve the photocatalytic performance of TiO_2, different strategies can be employed, such as the coupling and the use of metal NPs or other compounds in order to increase the electron–hole separation [187–191].

Very recently, Jedsukontorn *et al.* [187] prepared metal-decorated TiO_2 by sol immobilization route. TiO_2 was decorated by Bi, Pd, Pt, and Au, which promoted its photocatalytic activity to selective oxidation of glycerol. It was shown that the overall activity for glycerol conversion was ranked on the order of $Au/TiO_2 > Pt/TiO_2 > Pd/TiO_2 > Bi/TiO_2 > TiO_2$, which provided a glycerol conversion level of 92.8, 80.5, 63.6, 44.7, and 14.4%, respectively. The Au/TiO_2 photocatalyst exhibited the highest glycerol conversion activity due to the highest visible-light absorption compared to other photocatalysts, and also Au/TiO_2 photocatalyst had an appropriate mechanism of e^-–h^+ transfer to proceed the surface reaction

Grabowskaa *et al.* [188] prepared novel decahedral TiO_2 modified with Ru or Rh NPs, synthesized by hydrothermal method. The results showed that the novel material, which contains 0.2 wt.% Rh (0.2-Rh/TiO_2-HT), exhibited the best optical properties and a high degradation rate for phenol under UV–vis light (79% of phenol was degraded after 90 min of irradiation). Utsunomiya *et al.* [189] reported photodecomposition of NH_3 to H_2 and N_2 using metal-supported photocatalysts Ni-TiO_2 in an aqueous NH_3 solution under UV irradiation at room temperature. Possible reaction pathways by which N_2 and H_2 were formed through NH_2-NH_2 coupling and NH_3 decomposition proceeded via the formation of NH_2-NH_2. Ni^0 can be suggested to have enhanced the reaction pathways via H_2N-NH_2, because Ni^0 was present in the catalyst that showed a higher catalytic activity than others. Faraji *et al.* [190] fabricated RGO/Ag/TiO_2 nanotubes/Ti plates with high photocatalytic activity via electrochemical reduction of graphene oxide on Ag/TiO_2 nanotubes. The results of photocatalytic experiments demonstrated that the RGO/Ag/TiO_2 nanotube/Ti plate exhibits significantly enhanced photocatalytic activity for the photocatalytic degradation of MB dye: 89% MB molecules are decomposed within 120 min (conditions: 10 ppm aqueous solution of MB, five plates with a geometric area of 6 cm^2, and UV light irradiation). Evidence indicated that RGO/Ag plays as important role in facilitating charge separation/transfer in TiO_2 nanotubes (Figure 8.18).

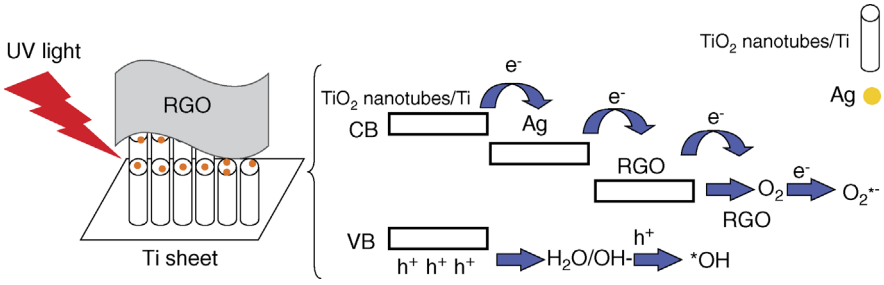

Figure 8.18 Ag/TiO_2 nanotube plates coated with RGO as photocatalysts (reproduced with permission from Ref. [190]. Copyright 2016, Elsevier).

8.5.2 Magnetic Hybrid Photocatalysts

Magnetically separable photocatalysts, as a new generation of photocatalysts, belong to a family of heterogeneous catalysts. The heterogeneous magnetic photocatalyst could be easily recovered by the use of magnetic field. Magnetic supports could overcome the limitation of separation from the liquid phase; thus, the photocatalyst could be effectively recycled by applying an external magnetic field [192]. Recently, many spinel-type ferrite complex oxides with visible-light photoactivity have been found to be easily collected and recovered for recycled use under an external magnetic field [193–199]. Moreover, spinel ferrites also have many other attractive benefits, such as biocompatibility, strong adsorption ability, remarkable mechanical hardness, and high electromagnetic performance [195,196].

Among them, $ZnFe_2O_4$, $CoFe_2O_4$, $NiFe_2O_4$, $MgFe_2O_4$, and $MnFe_2O_4$ are well-known narrow bandgap semiconductors that have various photocatalytic applications owing to their visible-light response and excellent photochemical stability. However, magnetic spinel ferrites alone have been proven to be photocatalytically less active because of the lower valence band edge potentials and poor performance in photoelectric conversion [54]. So, the design of the binary, ternary, and quaternary ferrite-based composite photocatalysts has been investigated very widely [192–205].

8.5.2.1 Binary Heterostructures

Many studies have reported the use of magnetically separable spinel ferrite-graphene photocatalysts. Graphene is a two-dimensional carbon material with high surface area, excellent conductivity, and unique graphitic basal plane structure. At present, the design and fabrication of graphene-based photocatalysts with high catalytic activity and magnetically separable function are very actual [201–205].

Fu *et al.* [201] prepared $MnFe_2O_4$/graphene photocatalyst through one-step hydrothermal method. $MnFe_2O_4$ NPs have an average diameter of 5.65 nm and their coupling with graphene sheets leads to high photocatalytic activity for the degradation of MB under visible light irradiation in the absence of hydrogen peroxide (Figure 8.19a). $MnFe_2O_4$/G(0.3) has a specific surface area sample of 179.30 $m^2 \cdot g^{-1}$ and a typical hysteresis loop in its magnetic behavior, indicating that it is a soft magnetic material (Figure 8.19c). The introduction of graphene into

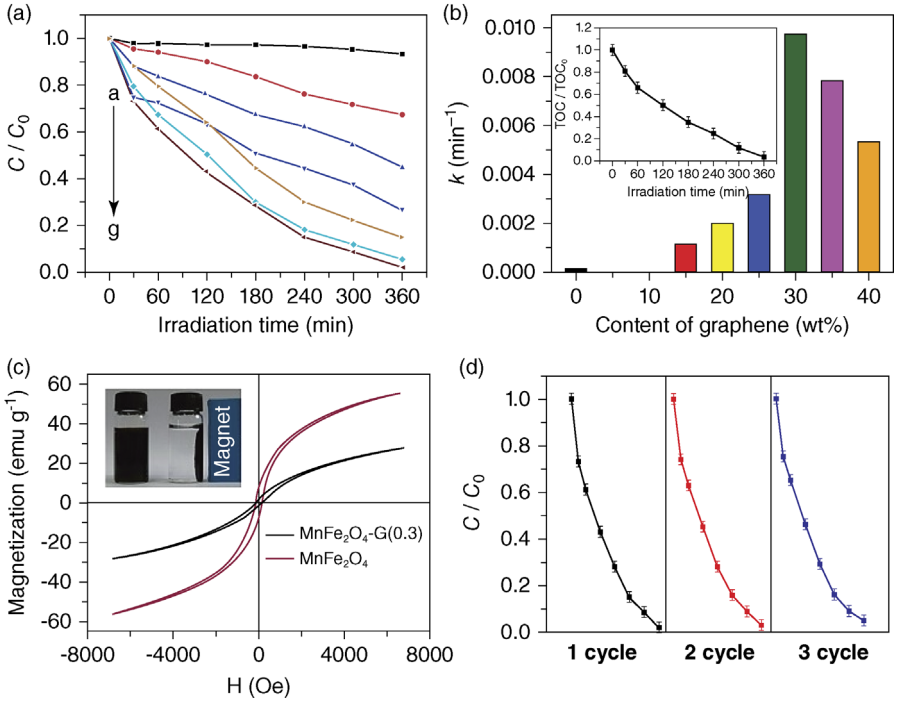

Figure 8.19 Magnetically separable $MnFe_2O_4$/graphene heteroarchitectures. (a) photocatalytic degradation of MB over (a) pure $MnFe_2O_4$, (b) $MnFe_2O_4$/G(0.15), (c) $MnFe_2O_4$/G(0.20), (d) $MnFe_2O_4$/G(0.25), (e) $MnFe_2O_4$/G(0.40), (f) $MnFe_2O_4$/G(0.35), and (g) $MnFe_2O_4$/G(0.30); (b) rate constant for the photodecomposition of MB on $MnFe_2O_4$/graphene photocatalysts with differing graphene content (inset: total organic carbon removal on $MnFe_2O_4$/G(0.30) photocatalyst; (c) hysteresis loops of pure $MnFe_2O_4$ and $MnFe_2O_4$/G(0.3) (the inset is the magnetic separation property of $MnFe_2O_4$/G(0.3) nanocomposite); and (d) photodegradation rate of MB in solution for three cycles using $MnFe_2O_4$/G(0.3) photocatalyst (reproduced with permission from Ref. [201]. Copyright 2012, American Chemical Society).

$MnFe_2O_4$/graphene photocatalyst leads to a qualitative change in the photocatalytic performance; the highest was obtained with 30% (w/w) graphene in $MnFe_2O_4$/graphene sample. The saturation magnetization (Ms), remanent magnetization (Mr), and coercivity (Hc) values of $MnFe_2O_4$/G(0.3) are 3.34 emu g^{-1}, 6 emu g^{-1}, and 142.83 Oe, respectively. This suggests that $MnFe_2O_4$/G(0.3) photocatalyst can be easily separated from the solution phase using an external magnet (Figure 8.19c).

More examples of coupled semiconductors can be found such as $CuFe_2O_4$/graphene for the degradation of methylene blue under visible light irradiation [202], $ZnFe_2O_4$/graphene [203], $NiFe_2O_4$/graphene [204], and $CoFe_2O_4$/graphene [205] for the degradation of MB. Fu *et al.* [205] reported about $CoFe_2O_4$/graphene nanocomposite 40% (w/w) for the degradation of dyes (MB, RhB, MO, active black BL-G, and active red RGB) under visible-light irradiation. It was shown that 40% (w/w) graphene in $CoFe_2O_4$/graphene gave the best performance in photocatalytic activity and almost all MB molecules in the solution were decomposed after 240 min.

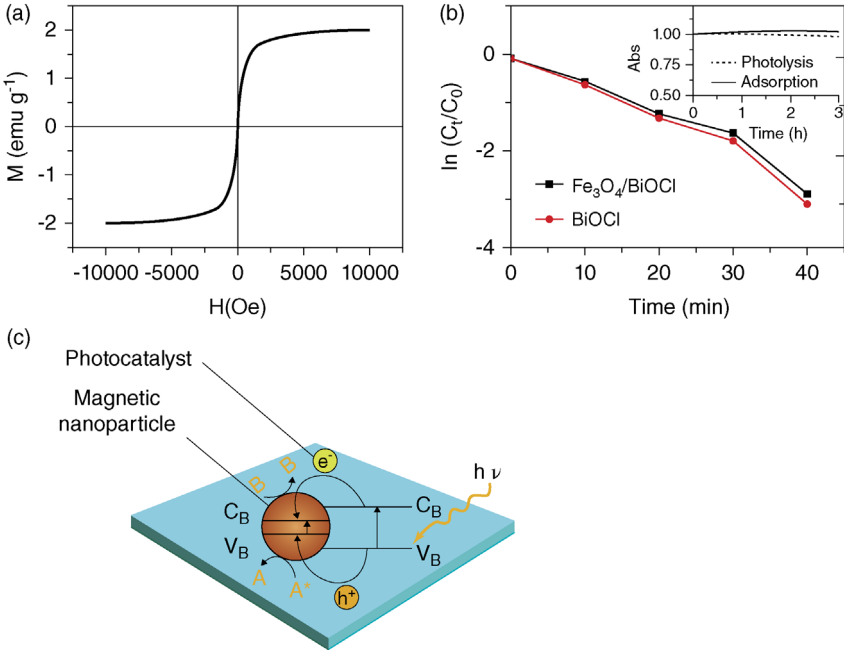

Figure 8.20 Magnetic photocatalyst Fe_3O_4/BiOCl nanocomposite. (a) Field-dependent magnetization of Fe_3O_4/BiOCl at 300 K (inset: a photograph showing magnetic recycle of the Fe_3O_4/BiOCl magnetic photocatalyst), (b) first-order plots for the photocatalytic degradation of RhB under visible-light irradiation using different samples (inset: absorption changes of direct photolysis and adsorption control experiments), and (c) scheme of possible charge carrier transfer in magnetic photocatalyst as-synthesized Fe_3O_4/BiOCl system (reproduced with permission from Ref. [192]. Copyright 2009, Elsevier).

Zhang *et al.* [192] prepared a novel magnetic photocatalyst, Fe_3O_4/BiOCl nanocomposite, by the chemical route and it was found that Fe_3O_4/BiOCl was an effective photocatalyst to degrade organic dyes (Figure 8.20). The photocatalytic activity of the superparamagnetic Fe_3O_4/BiOCl was investigated by the degradation of RhB dye in water (30 mg/l) under visible-light ($\lambda > 420$ nm) irradiation.

8.5.2.2 Ternary Heterostructures

In recent decades, in addition to the binary heterostructures, a lot of different ternary heterostructured composite photocatalysts have also been explored. Among them, ZnS-CdS-$Zn_{1-x}Cd_xS$ heterostructures with tunable morphology (0–2 D) [206], Ag–$BiVO_4$/$InVO_4$ composite [207], hierarchical Ag/Ag_2S/CuS ternary heterostructure composite [208], and so on. In this section, we will mainly focus on four widely distributed types of the ternary heterostructures: Fe_3O_4-based, Ag_3PO_4-based, g-C_3N_4-based, and BiOX-based photocatalysts.

8.5.2.2.1 Fe_3O_4-based Photocatalysts

Zhan *et al.* [209] reported on magnetic photocatalysts of cenospheres coated with Fe_3O_4/TiO_2 core/shell nanoparticles decorated with Ag nanoparticles

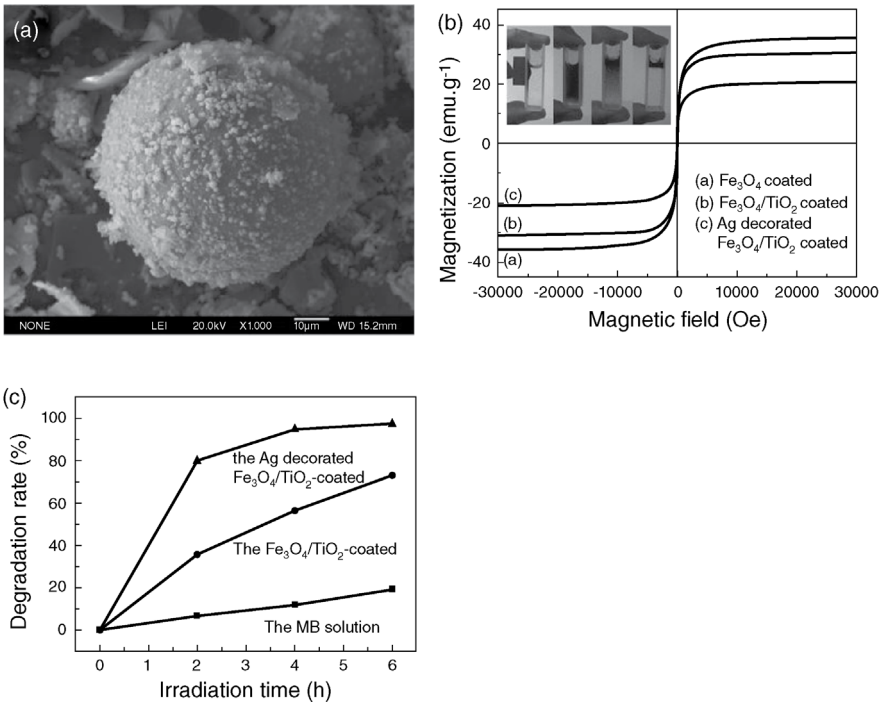

Figure 8.21 Photocatalytic activity of the Ag-decorated Fe_3O_4/TiO_2-coated cenospheres. (a) FESEM images of Ag-decorated Fe_3O_4/TiO_2-coated cenospheres, (b) hysteresis loops of as-prepared cenospheres at room temperature, and (c) effect of irradiation time on the degradation rate of MB solution under visible light (reproduced with permission from Ref. [209]. Copyright 2017, Elsevier).

(Figure 8.21a). Cenosphere, which is primarily composed of SiO_2, possesses the favorable characteristics of nontoxicity, high chemical stability, low cost, light weight mass, good insulation, and hollow spherical morphology. Because of the unique hollow structure and physical mechanics properties, it can float on the surface of water and absorb more solar light and thus might be used for environmental treatment. The hysteresis loops of the as-prepared cenospheres at room temperature (300 K) are represented in Figure 8.21b. As shown in the inset, the Ag-decorated Fe_3O_4/TiO_2-coated cenospheres can be attracted by a magnet. The Fe_3O_4-coated cenospheres deposited with a film of TiO_2 nanoparticles show a saturation magnetization 31 emu g^{-1}, whereas the Ag-decorated Fe_3O_4/TiO_2-coated cenospheres have a saturation magnetization of 21 emu g^{-1} and can be also attracted by a magnet. The calculated bandgap for Ag-decorated Fe_3O_4/TiO_2-coated cenosphere was far smaller (xx eV) than the theoretical value of anatase titania (3.2 eV). The DRS and photocatalytic degradation of MB dye results show that the photocatalytic activity of the Ag-decorated Fe_3O_4/TiO_2-coated cenospheres are much higher than that of the Fe_3O_4/TiO_2-coated one, which is ascribed to the surface plasmon resonance of Ag nanoparticles (Figure 8.21c).

Habibi-Yangjeh *et al.* [210] reported novel magnetic $Fe_3O_4/ZnO/NiWO_4$ nanocomposites. The evaluation photocatalytic activity under visible-light

irradiation was investigated for three dye pollutants of rhodamine B (RhB), MB, and MO. The optimal photocatalytic activity was exhibited by Fe_3O_4/ZnO/$NiWO_4$ (40%) nanocomposite with 97.9% of RhB degradation during light irradiation for 300 min.

Many other studies on magnetic photocatalysts such as Fe_3O_4/ZnO/$CoWO_4$ [211], rGO/Fe_3O_4/Ag_3PO_4 [212], g-C_3N_4/Fe_3O_4/Ag_2CrO_4 [213], Fe_3O_4@C@CdS [214], and so on have also been reported.

8.5.2.2.2 Ag_3PO_4-based Photocatalysts

In 2010, Yi *et al.* [215] reported the use of Ag_3PO_4 as an active visible-light-driven photocatalyst for the oxidation of water and photodecomposition of organic compounds. Silver orthophosphate (Ag_3PO_4) is a semiconductor with a narrow bandgap of 2.45 eV, which strongly absorbs visible-light irradiation (Figure 8.22).

Since then, various coupled photocatalytic systems, such as Ag_3PO_4/TiO_2 [216–218], Ag_3PO_4/Ag/ZnS [219], and Ag_3PO_4/Ag/SiC [220] composites have been developed to improve the photocatalytic activity and/or stability of Ag_3PO_4.

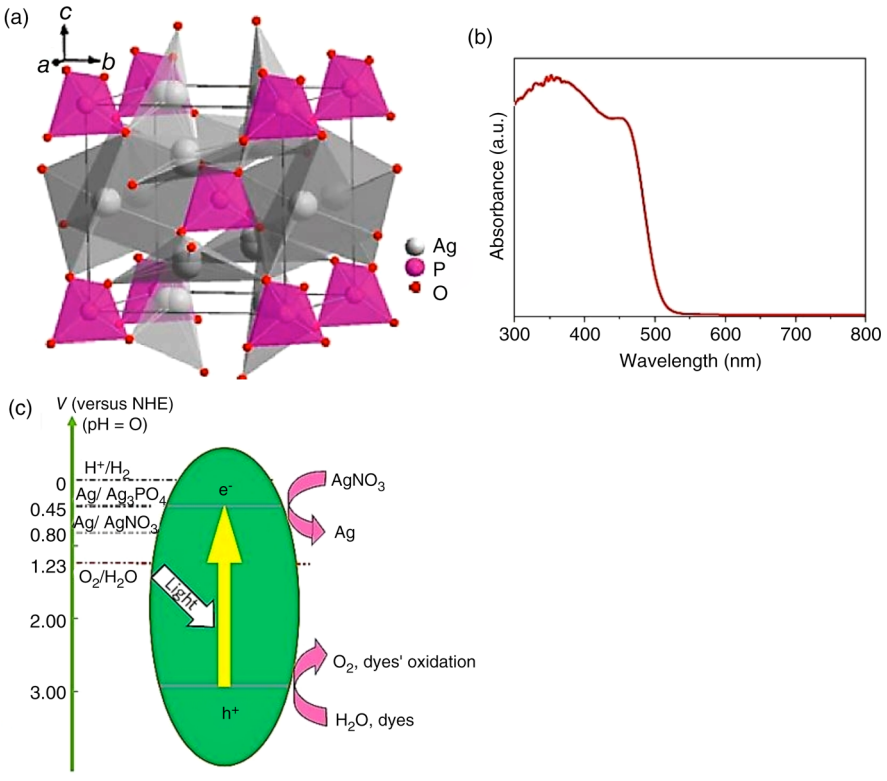

Figure 8.22 Crystal structure (a), optical property (b), and schematic drawing of redox potentials (c) of Ag_3PO_4 photocatalyst (reproduced with permission from Ref. [215]. Copyright 2010, Nature Publishing Group).

Shekofteh-Gohari *et al.* [221] reported about novel magnetically separable $ZnO/Ag_3VO_4/Fe_3O_4$ nanocomposites prepared by a facile refluxing method with 8 : 1 weight ratio of ZnO/Ag_3VO_4 to Fe_3O_4, which has a superior activity in the degradation of RhB under visible-light irradiation. Ag_3VO_4 have a narrow bandgap energy of about 2.1 eV, while Fe_3O_4 is well-known magnetic material. $ZnO/Ag_3VO_4/Fe_3O_4$ nanocomposite has remarkable absorption in complete range of the visible radiation. The saturation magnetization for the nanocomposite at 8500 Oe is 4.9 emu g^{-1}, which is high enough to be magnetically separated from the solution after decontamination processes. The photocatalytic activity of the nanocomposite was about 11.5-fold higher than that of ZnO/Fe_3O_4 nanocomposite.

8.5.2.2.3 g-C_3N_4-based Photocatalysts

Since Wang *et al.* [222] developed graphitic C_3N_4 (g-C_3N_4) as a visible-light-active photocatalyst for water splitting (Figure 8.23a–c), g-C_3N_4-based photocatalysis has

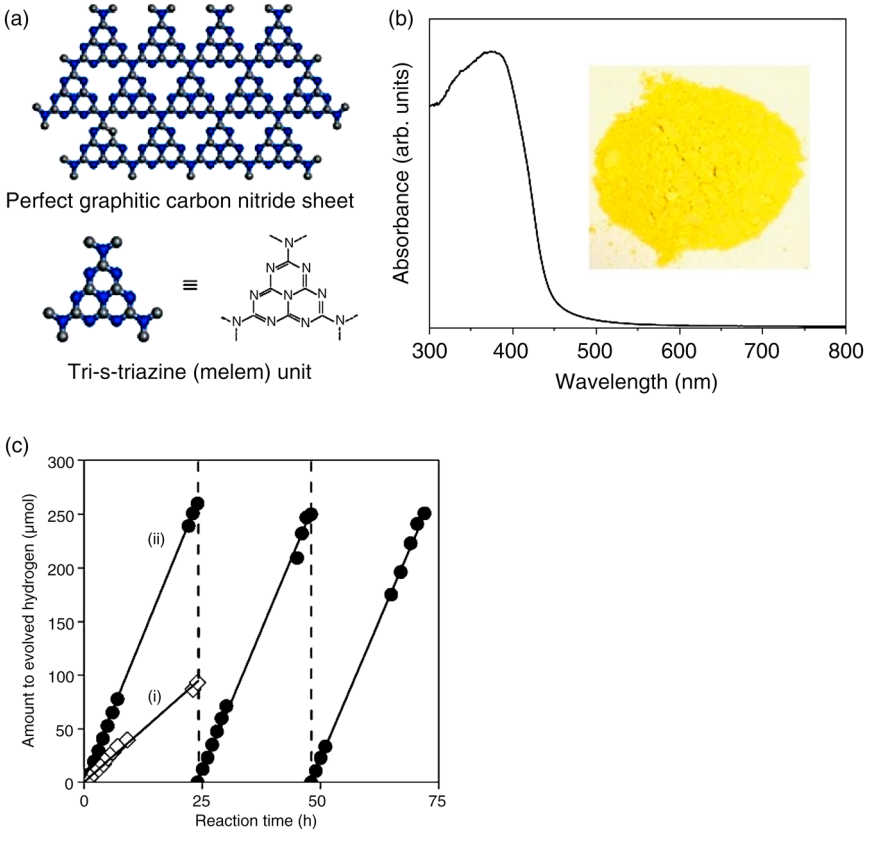

Figure 8.23 Optical and photocatalytical properties of g-C_3N_4 catalyst. (a) Crystal structure of graphitic carbon nitride, (b) optical properties of graphitic carbon nitride, and (c) stable hydrogen evolution from water by g-C_3N_4 ((i) unmodified g-C_3N_4 and (ii) 3.0 wt.% Pt-deposited g-C_3N_4 photocatalyst) (reproduced with permission from Ref. [222]. Copyright 2009, Nature Publishing Group).

become a very hot research topic. g-C_3N_4 has a bandgap of about 2.7 eV, with the CB and VB positions at about −1.1 and about +1.6 eV versus normal hydrogen electrode (NHE), respectively. This electronic structural character suggests that the g-C_3N_4 could photodegrade organic dye under visible-light irradiation. g-C_3N_4 can be used for various photocatalytic applications, such as water splitting, CO_2 reduction, dye degradation, and so on.

The cation or/and anion doping or coupling g-C_3N_4 to another semiconductor is an effective approach to create heterojunctions for extended absorbance and improved charge separation, which could further enhance its photocatalytic efficiency. A large number of semiconductors have been coupled with g-C_3N_4 to form semiconductor–semiconductor heterojunctions because visible-light photocatalytic efficiency of g-C_3N_4 is still relatively low and far from the requirements for practical applications. Different g-C_3N_4-based composites have shown superior photocatalytic degradation of organic pollutants (Ag_2CO_3/g-C_3N_4 [157], g-C_3N_4/CeO_2/ZnO [166], Ag_2O/g-C_3N_4/Fe_3O_4 [195], g-C_3N_4/Fe_3O_4/Ag_2CrO_4 [213], and g-C_3N_4/Fe_3O_4/Ag_3PO_4/Co_3O_4 [223]), hydrogen production (C-TiO_2@g-C_3N_4 [224] and $NiTiO_3$/g-C_3N_4 [225]), and so on.

8.5.2.2.4 BiOX-based Photocatalysts

Bismuth oxyhalides BiOX (X = Cl, Br, and I) are another category of Bi-based semiconductors. Recently, bismuth oxychloride (BiOCl) has attracted particular attention among researchers because of its excellent photocatalytic and photoluminescence properties. For example, it has high photocatalytic activity for the degradation of organic dyes [226–229]. The layered structured BiOCl possesses wide bandgap (E_g) of 3.4 eV and hence efficient separation of photoinduced electron–hole pair. It is noted that with increasing atomic number, the bandgap of BiOX (X = Cl, Br, and I) becomes narrower, 3.2 eV for BiOCl, 2.7 eV for BiOBr, and 1.7 eV BiOI, which could allow to maximize their photocatalytic activities in a large range [230]. Various approaches for improving the photocatalytic activity of BiOX photocatalyst have been proposed including doping, surface modification, and coupling with other semiconductor.

Ge *et al.* [229] reported that flower-like BiOCl hierarchical structures were successfully synthesized in the presence of eutectic choline chloride/urea mixtures through a solvothermal process (Figure 8.24a). The optical properties were studied using UV–vis DRS indicating a bandgap of 3.05 eV, which is suitable for photocatalytic decomposition of organic contaminants (Figure 8.24b). The evaluated photocatalytic activity, by the degradation of RhB in aqueous solution under sunlight irradiation, did not change after five cycles (Figure 8.24c).

Various bismuth oxyhalide-based photocatalysts can be classified as photocatalytic heterostructures that can be activated with visible light radiation. Many of these compounds have been mainly investigated for oxygen and hydrogen evolution from water splitting; nevertheless, degradation of organic pollutants has also been carried out under visible or solar light. Different magnetic BiOX-based photocatalysts were reported in literature: BiOBr-$ZnFe_2O_4$ [231], $CoFe_2O_4$/BiOX (X = Cl, Br, and I) [232], BiOBr/$CoFe_2O_4$ [233], $NiFe_2O_4$/BiOBr [234], $Bi_4O_5Br_2$/$Bi_{24}O_{31}Br_{10}$/Bi_2SiO_5 [235], $Ni_{0.5}Zn_{0.5}Fe_2O_4$@-PANI-modified BiOCl [236], and so on.

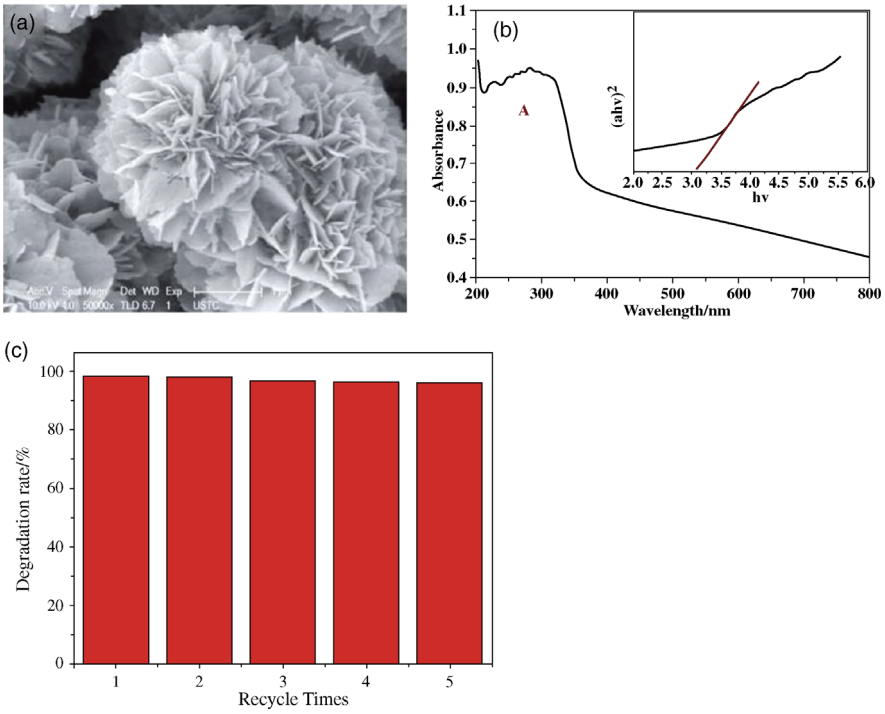

Figure 8.24 Flower-like hierarchical BiOCl photocatalyst. (a) SEM images of the BiOCl photocatalyst with flower-like hierarchical structure, (b) UV–vis diffuse reflectance spectra and $(ahv)^2$ versus *hv* curve of flower-like BiOCl, and (c) the photodegradation of RhB in solution for five cycles using flower-like BiOCl (reproduced with permission from Ref. [229]. Copyright 2015, the Royal Society of Chemistry).

8.6 Photocatalytic Activity

Environmental pollution has drawn much attention to the vital need for ecologically clean materials and chemical technologies. Photocatalysis is one of the solutions to address the environmental contaminants. This section provides a detailed overreview of the environmental applications of different semiconductor and semiconductor-based heterostructures. The huge studies regarding water photocatalytic purification refer to a big class of exogenous pollutants such as dyes, pharmaceutical drugs, and heavy metal ions. The photocatalytic hydrogen production and CO_2 reduction in the presense of photocatalysts under UV irradiation or solar light are also included in this section.

8.6.1 Photocatalyst for Water Decomposition

Hydrogen (H_2) is considered an alternative energy resource that can be regarded as renewable and environment-friendly. The mechanism for photocatalytic water decomposition includes the absorption of solar light, generation of electrons–holes, and catalytic reactions for H_2 or O_2 evolution. For H_2 generation, the

bottom of the CB should be lower than the H^+/H_2 redox couple (0.0 V versus NHE) and the top of the VB should be higher than the H_2O/O_2 redox couple (+1.23 V versus NHE) [237]. So, the development of single and hybrid nanostructures with enhanced photocatalytic activity for hydrogen generation has gained a lot of attention [238–243].

Quaternary oxide photocatalysts with perovskite-type structure with the general formula ABO_3 have been mainly investigated for both H_2 and O_2 evolution from aqueous solutions. Parida *et al.* [241] reported about the synthesis of nanophotocatalyst $LaFeO_3$ with orthorhombic perovskite structure by sol–gel autocombustion method (Figure 8.25). The highest amount of H_2 and O_2 evolved in 180 min over $LaFeO_3$ activated at 500 °C was recorded to be 1290 and 640 µmol, respectively, having an apparent quantum efficiency (AQE) of 8.07%.

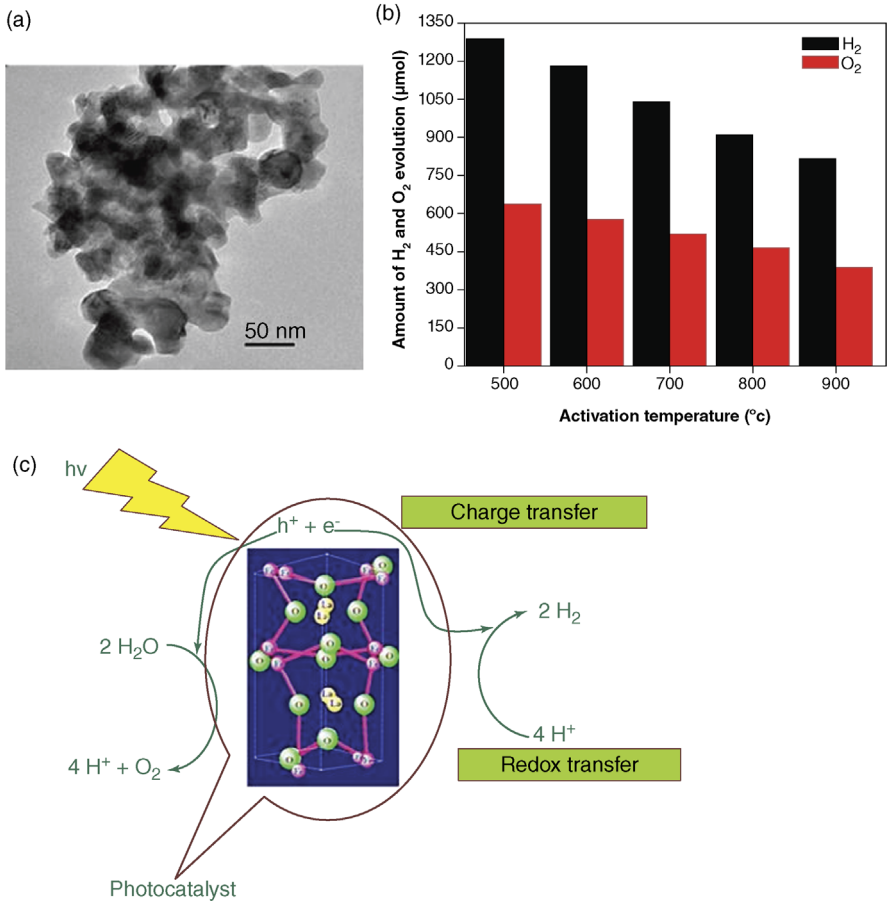

Figure 8.25 Nanocrystalline $LaFeO_3$ as an efficient visible-light-responsive photocatalyst for water decomposition. (a) HRTEM micrographs of $LaFeO_3$ activated at 500 °C, (b) the amount of H_2 and O_2 gas evolution over $LaFeO_3$ nanoparticles as a function of activation temperature, and (c) schematic representation of the mechanism of water splitting (reproduced with permission from Ref. [241]. Copyright 2010, Elsevier).

Zhao *et al.* [242] fabricated ternary graphitic carbon nitride/red phosphorus/molybdenum disulfide heterostructure with different amounts of MoS_2 (g-C_3N_4/RP-3.18/MoS_2-Y (Y = 0.14, 0.33, 0.52, and 0.80 wt%), where Y refers to the loading weight percentage of MoS_2). The highest initial H_2 generation rate of 257.9 μmol·g^{-1}·h^{-1} is approximately 859.7 and 4.4 times more than that of pure g-C_3N_4 and g-C_3N_4/RP-3.18, respectively. Under the irradiation of visible light, the highest total H_2 evolution amount 515.8 μmol·g^{-1} is obtained for the catalyst with 0.52 wt% MoS_2 loading during a reaction time of 2 h (H_2 evolution amount is 0.6 μmol·g^{-1} for pure g-C_3N_4, 118 μmol·g^{-1} for g-C_3N_4/RP-3.18, and 515.8 μmol·g^{-1} for C_3N_4/RP-3.18/MoS_2-0.52 over reaction time of 2 h).

Fang *et al.* [243] investigated H_2 generation on $Co_{0.5}Cd_{0.5}S$/g-C_3N_4 composite photocatalyst. The highest rate of H_2 production is up to 6.31 mmol g^{-1} h^{-1} under visible light ($\lambda > 400$ nm). Another sulfide photocatalyst CdS/NiS prepared by Zhou *et al.* [244] using one-pot hydrothermal method showed superior H_2 evolution of 24.37 mmol h^{-1} g^{-1} over CdS/NiS obtained under visible light.

Many other single and g-C_3N_4-based nanocomposites (binary oxides [245], vanadates [246], titanates [247], ortoferrire [248], niobates [249], etc.) can be activated with visible light for water splitting and have been investigated as photocatalysts. Depending on synthetic approach, these heterostructures have shown high photocatalytic performance for water decomposition under various catalytic conditions including the light source, amount of the catalyst, and H_2 generation rate.

8.6.2 Photocatalyst for Dye Degradation

Dyes are among the largest group of toxic organic compounds, which represent a danger to environment and human beings. The photocatalytic degradation of organic dyes is of great importance in water treatment. Synthetic dyes such as MB, RhB, and MO (Table 8.3) are widely used in the paper and textile industries. Wastewater containing these dyes has to be treated adequately before discharge into the environment. Therefore, the development of low-cost and efficient adsorbents for the removal of organic dyes from waste effluents is of considerable environmental importance. In recent years, many research works have paid increasing attention to the degradation of dyes in water by heterogeneous photocatalysis [250–271]. Although most dyes can be easily degraded by heterogeneous photocatalysis, the degradation rate depends upon the family of the dye and the used semiconductor photocatalyst [250]. Dye molecules can be easily excited by UV irradiation or visible light to allow transfer of electrons from the valence band to the conduction band of the semiconductor photocatalyst, leaving holes behind. These electron–hole pairs move to the surface catalyst where they initiate oxidation–reduction reactions with adsorbed pollutants.

8.6.2.1 Methylene Blue

Although MB is not very hazardous, several side effects have been reported, including carcinogenicity, mutagenicity, permanent burns to human and animal eyes, toxic effects on aquatic organisms, and so on. This is why the photocatalytic

Table 8.3 The chemical structure of the widely used dyes and its absorption band maxima (λ_{max}).

Dyes	Chemical structure	λ_{max} (nm)
Methylene blue 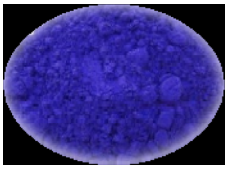	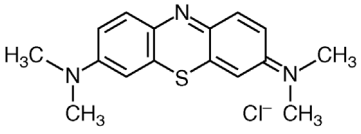	660
Methyl orange 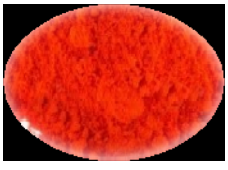	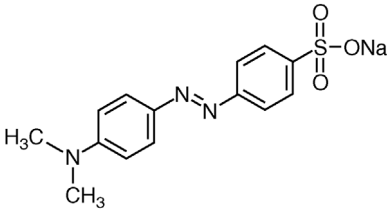	520 (Red form) 440 (Yellow form)
Rhodamine B 	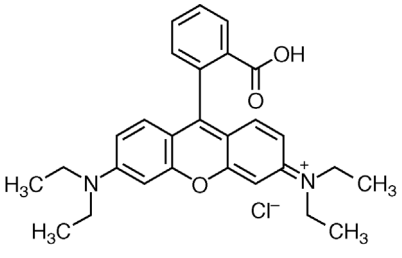	551

degradation of MB by using heterogeneous photocatalysis is of vital interest [251–256].

Helal *et al.* [251] reported about novel heterostructures of Fe_2O_3/Bi_2S_3 nanorods synthesized via one-step hydrothermal route and employed effectively as visible-light-driven photocatalysts for the degradation of organic pollutants such as MB and phenol (Figure 8.26a). The results showed that a maximum degradation efficiency of MB ~90% was achieved after 300 min using $0.06Fe_2O_3/Bi_2S_3$ molar ratio under visible light (Figure 8.26b).

Li *et al.* [252] reported on a novel magnetically separable $BiOBr/NiFe_2O_4$ composite photocatalyst fabricated through a facile hydrothermal method. The photocatalytic degradation of MB under the excitation of visible light (Figure 8.27) confirmed that the $BiOBr/NiFe_2O_4$ composite exhibited the best performance with a degradation rate of 90% within 60 min for $NiFe_2O_4$ amount of 20% (conditions: 10 mg of the catalyst, 10 ml of MB aqueous solution (10 $mg{\cdot}l^{-1}$), $\lambda > 420$ nm). The photodegradation mechanism of MB molecules by $BiOBr/NiFe_2O_4$ composite under the irradiation of visible light is presented in schematic illustration diagram (Figure 8.27).

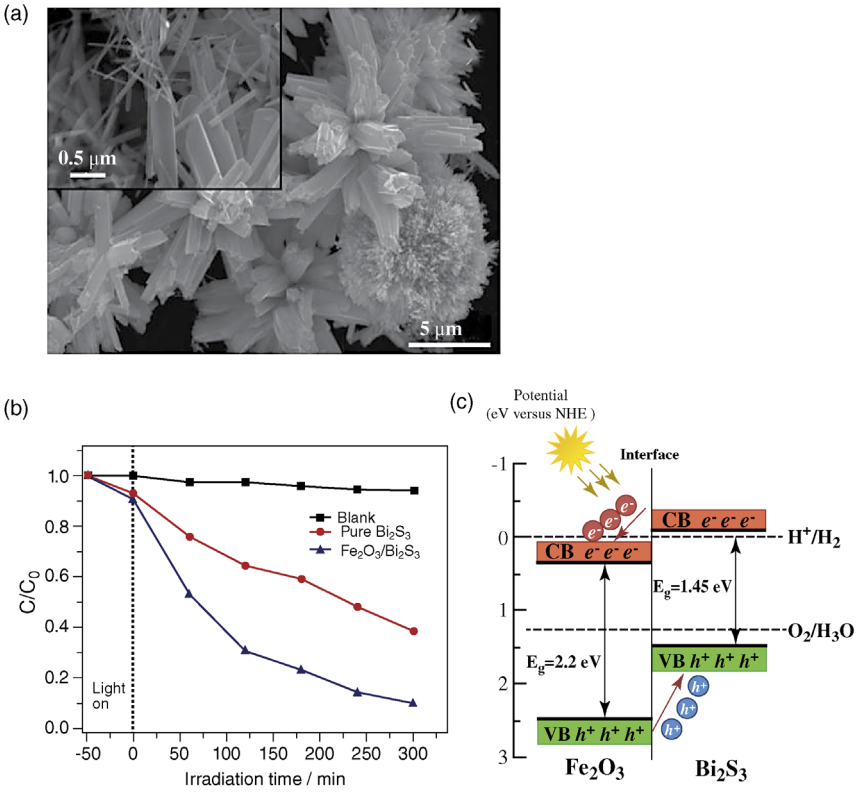

Figure 8.26 Heterostructured Fe_2O_3/Bi_2S_3 nanorods with enhanced photocatalytic activity under visible light. (a) FESEM image of Fe_2O_3/Bi_2S_3 heterostructure with a magnified image in the inset, (b) a comparative photocatalytic activities of pure Bi_2S_3 and Fe_2O_3/Bi_2S_3 heterostructure (MB concentration: 10 mg l^{-1}; volume of MB: 200 ml^{-1}; photocatalyst loading: 100 mg), and (c) deduced energy band levels of Fe_2O_3/Bi_2S_3 heterostructure showing the charge separation process [251]. (reproduced with permission from Ref. [251]. Copyright 2017, Elsevier).

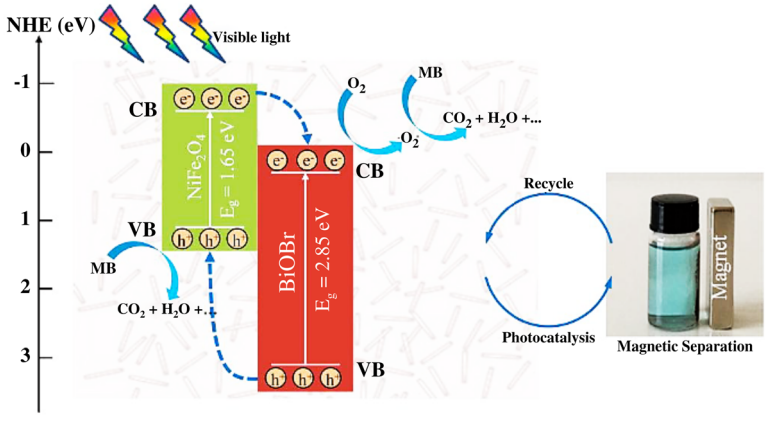

Figure 8.27 Photocatalytic degradation mechanism of MB over the $BiOBr/NiFe_2O_4$ composite photocatalysts synthesized by hydrothermal method (reproduced with permission from Ref. [107]. Copyright 2017, Elsevier).

Other spinel-based magnetically separable photocatalysts have been also successfully tested for the degradation of MB under the presence of visible or UV light including $Ni_xZn_{1-x}Fe_2O_4$ [253], $CoFe_2O_4/CeO_2$ nanocomposite [254], graphene-$Co_xZn_{1-x}Fe_2O_4$ nanoheterostructures [255], $CoFe_2O_4$–graphene hybrid material [256], and so on.

8.6.2.2 Methyl Orange

The different heterogeneous photocatalysts have been studied to determine their photocatalytic oxidation properties for MO degradation [257–263]. Wang et at [257] prepared nano-TiO_2 photocatalyst by sol–gel technique, on the basis of which carbon foam-loaded nano-TiO_2 photocatalyst (nano-TiO_2/CF) was synthesized by impregnating load, baking, and forming methods. The results showed that when the concentration ratio of tetrabutyl titanate to absolute ethyl alcohol was 1 : 8, impregnating load twice, and baking at 500 °C, the obtained nano-TiO_2/CF photocatalyst exhibited the most desired efficiency for the degradation of MO solution, reaching up to 83–87% (conditions: 0.1 g of TiO_2/CF photocatalyst, 20 mg·l^{-1} methyl orange solution). In this case, activated carbon can possibly prevent recombination of electron–hole pairs.

Trandafilović *et al.* [258] prepared ZnO NPs doped with different Eu^{3+} concentrations in water (ZnO:Eu(x%)-W) and other solvents (methanol ZnO:Eu(x%)-M and ethanol ZnO:Eu(x%)-E). The results indicated that the most effective samples were ZnO:Eu(3%)-W and ZnO:Eu(10%)-M (complete color degradation was observed after 60 min, 1 mg catalyst, 10 ppm aqueous solution of methyl orange).

Dorraj *et al.* [259] reported on a novel Cu-TiO_2/ZnO heterojunction nanocomposite that was synthesized for the first time via a two-step process by sol–gel method. The results showed that the degradation efficiency of MO reaches 83% in the presence of 3% Cu-TiO_2/30%ZnO nanocomposite after 60 min of irradiation time. This excellent photocatalytic activity was mainly attributed to the formation of heterojunction favouring efficient separation of photoinduced electron–hole pairs at the interface.

Magnetically recyclable nanophotocatalysts for the treatment and remediation of dyes have also gained much attention during the past few years because of their high surface area, low bandgap, high efficiency, and excellent recyclability [260,261]. Mousavi *et al.* [260] reported on novel magnetically separable g-$C_3N_4/Fe_3O_4/Ag_3PO_4$/AgCl nanocomposites, prepared by a facile ultrasonic irradiation method. It was found that g-$C_3N_4/Fe_3O_4/Ag_3PO_4$/AgCl(30%) nanocomposite displayed the highest photocatalytic activity for the degradation of MO and can be easily separated from the solution by an external magnetic field.

Another magnetically separable photocatalyst was reported by Rahimi-Nasrabadi *et al.* [261]. Cerium-doped copper ferrite NPs ($CuFe_{2-x}Ce_xO_4$) synthesized by an autocombustion method showed about 66% of MO degradation after 60 min irradiation of UV light.

8.6.2.3 Rhodamine B

RhB is widely used as a colorant in textiles and food industries and is also a well-known water pollutant. It is harmful to human beings and animals and causes

irritation of the skin, eyes, and respiratory tract. It carcinogenicity and toxicity have been experimentally proven. Thus, systematic efforts to degrade RhB from aqueous medium using different photocatalysts have attracted great attention.

Golzad-Nonakaran *et al.* [264] reported on ZnO/AgI/Ag_2CO_3 nanocomposites fabricated by an ultrasonic irradiation method. Photodegradation of dye pollutants (RhB, MO, and MB) under visible-light irradiation measurements confirmed that after light irradiation for 75 min, about 98.7% of RhB molecules were degraded over ZnO/AgI/Ag_2CO_3(30%). Based on the results, the enhanced photocatalytic activity was attributed not only to the generation of more charge carriers but also to more suppression of electron–hole pair recombination, due to the formation of tandem *n*–*n* heterojunctions (Figure 8.28a).

Mousavi *et al.* [265] prepared magnetically separable ternary g-C_3N_4/Fe_3O_4/BiOI nanocomposites as novel visible-light-driven photocatalysts. It is shown that molecules of RhB are almost completely (around 98 %) degraded over g-C_3N_4/Fe_3O_4/BiOI(20%) nanocomposite under visible-light irradiation for 180 min (conditions: ([RhB] = 1×10^{-5} M, photocatalyst weight = 0.1 g) (Figure 8.28b).

A novel magnetically separable quaternary visible-light-driven g-C_3N_4/Fe_3O_4/Ag_3PO_4/Co_3O_4 nanocomposite was fabricated by Mousavi *et al.* [223] using ultrasonic method. The g-C_3N_4/Fe_3O_4/Ag_3PO_4/Co_3O_4 nanocomposites showed considerable photocatalytic activity for the degradation of RhB under visible-light irradiation; in 150 min, RhB is almost completely degraded. Another novel magnetic g-C_3N_4/Fe_3O_4/AgI/Ag_2CrO_4 nanocomposite was prepared via reflux method by Akhundi *et al.* [266], which exhibited excellent performance for the photocatalytic degradation of RhB under visible-light irradiation (99.4% degradation of RhB in 150 min). The same research group of Akhundi *et al.* [267] prepared very similar quaternary magnetically recoverable g-C_3N_4/Fe_3O_4/Ag/Ag_2SO_3 plasmonic photocatalyst. The composite degraded 99% of RhB in 270 min, whereas about 38 and 49% of degradations were achieved over g-C_3N_4 and g-C_3N_4/Fe_3O_4, respectively.

More examples of different photocatalysts for rhodamine B degradation can be found in the literature such as Fe_3O_4/ZnO/$CuWO_4$ [268], Ag_2O/g-C_3N_4/Fe_3O_4 [195], RGO-supported ferrite (MFe_2O4, M = Mn, Zn, Co, and Ni) hybrids [269], bentonite/g-C_3N_4/Ag_3PO_4 [270], and so on.

8.6.3 Photocatalyst for Pharmaceutical Drugs Degradation

Recently, antibiotics and other pharmaceutical drugs are widely applied to treat various human and animal diseases [272]. The presence of such pharmaceutical compounds in environment may cause adverse effects on aquatic life. In recent decades, different heterogeneous photocatalysts have been extensively investigated under UV or solar light irradiation for the degradation of pharmaceutical drugs, such as *paracetamol* (La/ZnO [273]), *amoxicillin* (C_3N_4@$MnFe_2O_4$-graphene [200]), *metronidazole* (C_3N_4@$MnFe_2O_4$-graphene [200]), *tetracycline* (Ag/AgCl-Fe^0 [196], C_3N_4@$MnFe_2O_4$-graphene [200], Ag_3PO_4/$CuBi_2O_4$ [274], NGQDs-BiOI/$MnNb_2O_6$ [275], Ag/TiO_2 [276]), *carbamazepine* (Bi^{3+}/$NaBiO_3$ [277]), *amplicillin* (BiOCl/graphene [278], BiOCl/chitosan [278], WO_3/BiOCl/graphene [279], Bi_2O_3/BiOCl/graphene [280], Bi_2O_3/BiOCl/

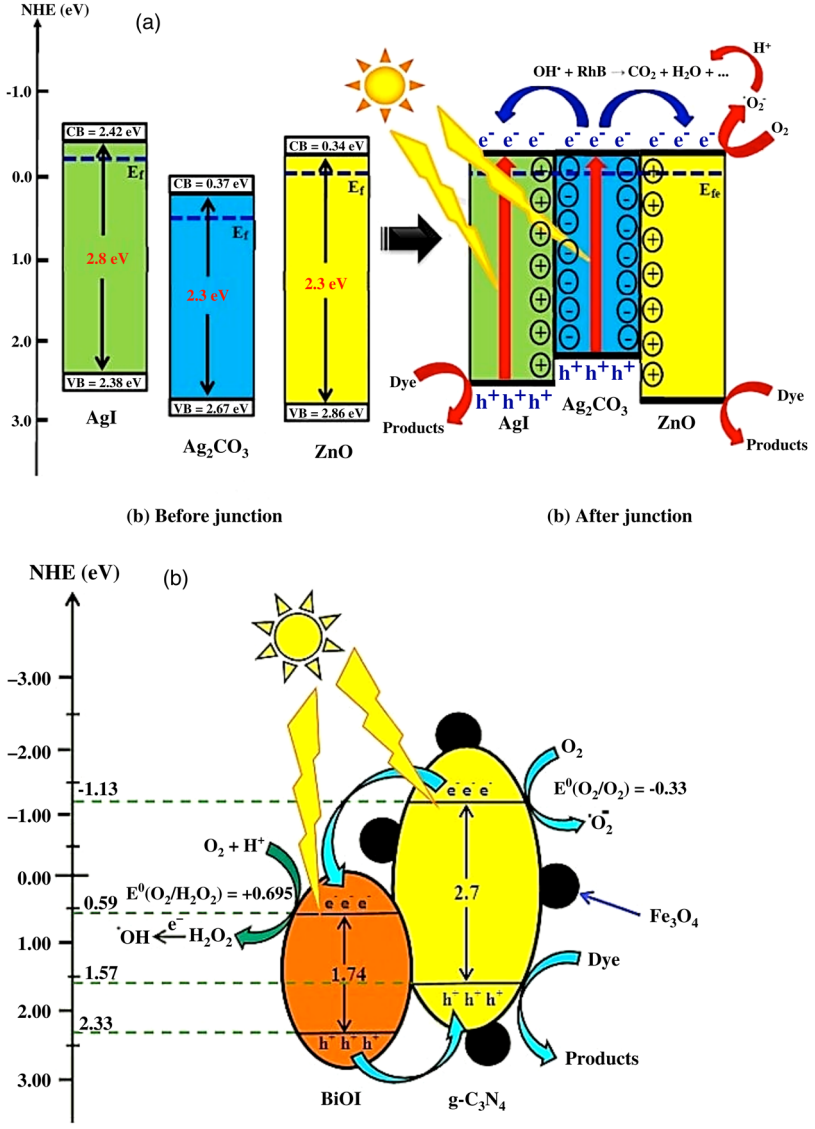

Figure 8.28 The photocatalytic degradation mechanism of rhodamine B over the (a) ZnO/AgI/Ag_2CO_3 nanocomposites (reproduced with permission from Ref. [264]. Copyright 2016, Elsevier) and (b) g-C_3N_4/Fe_3O_4/BiOI nanocomposites (reproduced with permission from Ref. [265]. Copyright 2016, Elsevier).

chitosan [280]), *oxytetracyline* (NGQDs-BiOI/$MnNb_2O_6$ [275], BiOCl/graphene [278], BiOCl/chitosan [278], WO_3/BiOCl/graphene [279], Bi_2O_3/BiOCl/graphene [280], Bi_2O_3/BiOCl/chitosan [280], Au-CuS-TiO2 [281]), *ciprofloxacin* (C_3N_4@$MnFe_2O_4$-graphene [200], NGQDs-BiOI/$MnNb_2O_6$ [275], g-C_3N_4/$BiPO_4$ [282]), *doxycycline* (NGQDs-BiOI/$MnNb_2O_6$ [275]), and *sulfamethoxazole*

(WO_3/TiO_2 [283]), have been degraded by applying different heterogeneous photocatalyst.

Ha-Tran Thi *et al.* [273] prepared visible light-driven photocatalyst of lanthanum (La) doped ZnO NPs by a facile precipitation method. La-doped ZnO photocatalysts were applied to treat 100 mg L^{-1} paracetamol in aqueous solution under visible-light irradiation after 3 h. With a degradation efficiency of 99%, 1.0 wt% La-doped ZnO photocatalyst showed the highest photocatalytic activity for the degradation of paracetamol.

Shi *et al.* [274] reported about the preparation of $Ag_3PO_4/CuBi_2O_4$ (ACBO) composites with a small quantity of Ag_3PO_4 NPs (0.5–10 wt.%) that were synthesized by an *in situ* precipitation method. The results indicated that ACBO with 5 wt.% content of Ag_3PO_4 (ACBO-5) exhibited the highest photocatalytic activity for the degradation of tetracycline under visible light irradiation, which is around 2.79 and 2.16-fold higher than that of pristine Ag_3PO_4 and $CuBi_2O_4$, respectively.

Newly designed magnetic g-$C_3N_4/MnFe_2O_4$/graphene (C_3N_4@$MnFe_2O_4$-G) composites with enhanced photocatalytic activity were successfully synthesized by Wang *et al.* [200]. The photocatalytic behavior of C_3N_4@$MnFe_2O_4$-G was estimated in photo Fenton-like degradation of antibiotic pollutants, including metronidazole, amoxicillin, tetracycline, and ciprofloxacin, using persulfate ($S_2O_8^{2-}$) as an oxidant under visible light illumination. It was shown that C_3N_4@$MnFe_2O_4$-G composites show a superior catalytic activity with 94.5% removal of metronidazole that was almost 3.5 times as high as that of pure g-C_3N_4. It was explained that a *p–n* heterojunction can be easily formed and the direct recombination of electrons and holes is greatly minimized when the n-type g-C_3N_4 is coupled with p-type ferrites [200].

Liu *et al.* [196] prepared magnetically separable Ag/AgCl zero valent iron NPs (ZVIPs) impregnated zeolite X (Ag/AgCl/(*x*)Fe-ZX) photocatalysts by hydrothermal precipitation–photoreduction method for tetracycline (TC) degradation. The Ag/AgCl/(*x*)Fe-ZX could be effectively separated from water due to the good magnetic property. When the content of the ZVIPs increased, the photocatalytic efficiency of Ag/AgCl/(x)Fe-ZX increased. The photocatalytic efficiency of TC degradation was maximum as the weight ratio of ZVIP was 5%. The TC degradation efficiency was 92% at 3 h (the initial TC concentration, 100 mg l^{-1}; the dosage of Ag/AgCl/(0.05) Fe-ZX, 1 g l^{-1}).

Yan *et al.* [275] prepared novel nitrogen doped graphene quantum dot-BiOI/$MnNb_2O_6$ *p–n* junction photocatalysts by a simple hydrothermal method. Antibiotics such as tetracycline, oxytetracyline, ciprofloxacin, and doxycycline were chosen as target pollutants to explore the photocatalytic performance under visible light. The obtained results showed that within 60 min of irradiation, the tetracycline degradation ratio of 5% NGQDs-Bi/Mn sample reached 87.2%. The proposed degradation pathways for photocatalytic degradation of tetracycline with 5% NGQD-Bi/Mn sample is shown in Figure 8.29. Under visible-light irradiation for 120 min, 57.4% of ciprofloxacin, 64.7% of doxycycline, and 72.1% of oxytetracyline could be degraded, suggesting that the 5%NGQD-Bi/Mn sample was an efficient photocatalyst for antibiotic degradation.

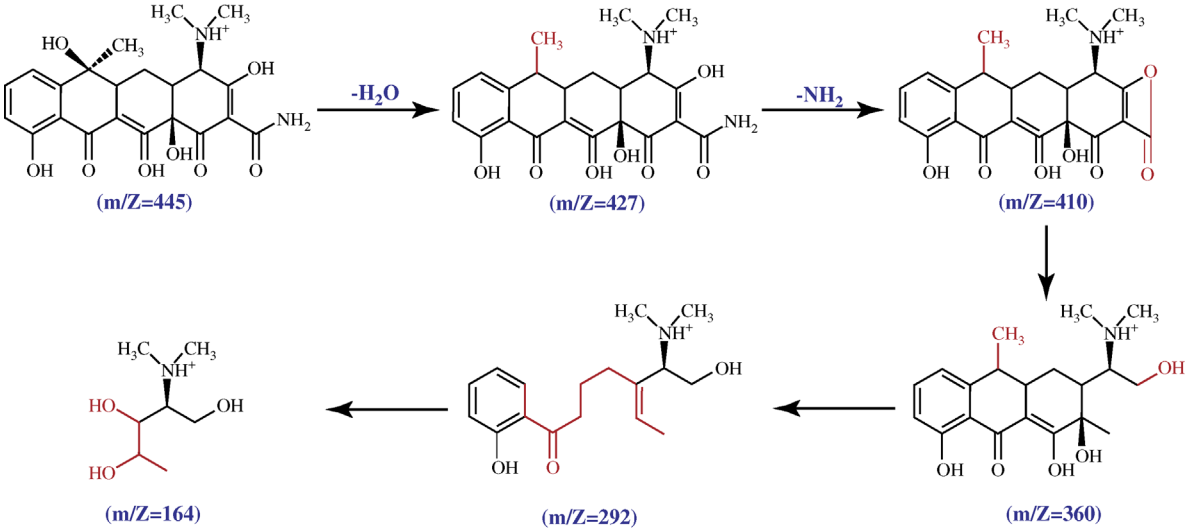

Figure 8.29 Proposed degradation pathways for photocatalytic degradation of tetracycline with 5%NGQD-Bi/Mn sample (reproduced with permission from Ref. [275]. Copyright 2017, Elsevier).

8.6.4 Photocatalyst for Reduction of Heavy Metal Ions

Water pollution by heavy metals has become a serious problem because of their adverse effects on ecological systems and human health. Heavy metals such as copper, chromium, cadmium, lead, zinc, mercury, and nickel are highly toxic, mutagenic, and carcinogenic at even relatively low concentrations [284]. Thus, the photocatalytic removal of heavy metals is rapidly gaining importance in wastewater treatment.

Chromium exists in the aquatic environment mainly in two states: *hexavalent Cr(VI)* and *trivalent Cr(III)*. Hexavalent chromium Cr(VI) is known to be toxic and carcinogenic, whereas Cr(III) is less toxic and can be readily precipitated out of solution in the form of $Cr(OH)_3$. The most probable Cr(VI) species in aqueous solutions are $Cr_2O_7^{2-}$, $Cr_2O_4^{2-}$, H_2CrO_4, and $HCrO_4^-$, although the relative distribution depends on the solution pH, the Cr(VI) concentration, and the redox potential.

Zhang *et al.* [285] synthesized a new high-efficiency visible-light photocatalyst fabricated from SnS_2 and conjugated derivative (CPVA) by thermal dehydration of polyvinyl alcohol (PVA), and evaluated its performance in photocatalytic reduction of aqueous Cr(VI). The results showed that SnS_2/CPVA nanocomposite (SnS_2/CPVA-1%-180 °C-2 h) had exceptionally higher photocatalytic activity in the reduction of aqueous Cr(VI) under visible-light irradiation ($\lambda > 420$ nm, 50 mg l^{-1} $K_2Cr_2O_7$, the dosage of the catalyst 300 mg, 100% reduction after 150 min).

Several studies were reported on the photocatalytic reduction of Cr(VI) from wastewater by using different TiO_2-based heterogeneous photocatalysts [286–290]. Zheng *et al.* [286] reported on the synthesis of hierarchical TiO_2/SnO_2 photocatalysts with different morphologies. Almost 99% of Cr(VI) were reduced after UV irradiation for 60 min of TiO_2/SnO_2 nanobelts, which is higher than that of Degussa P25 (conditions: the dosage of the catalyst 100 mg, 10 mg l^{-1} $K_2Cr_2O_7$ at pH 3). It can be explained by a better charge separation, fast and long-distance electron transport, and large surface-to-volume ratio of TiO_2/SnO_2 nanobelts.

Kumordzi *et al.* [291] prepared a composite catalyst of TiO_2 and graphene synthesized by a hydrothermal treatment method. It was used to photoreduce **Zn (II)**, the most abundant heavy metal found in combined sewer overflows (CSOs). The TiO_2–graphene composite photocatalyst showed a $20.3 \pm 0.04\%$ increase in the photoreduction of Zn^{2+} under solar light compared to undoped TiO_2. This enhancement is a result of the availability of more sorption sites, decrease in bandgap of the TiO_2, and effectiveness of the charge separation in TiO_2–graphene composite catalyst.

There are few studies in the literature reporting on heterogeneous photocatalysis, which demonstrated a remarkable photocatalytic activity for other heavy metals removal: **Cr(III)** (TiO_2/SiO_2 [292]), **Co(II)** (TiO_2/SiO_2 [292]), **Pb (II)** (TiO_2/SiO_2 [292,293], TiO_2/ZrO_2 [293], and Gd/CeO_2 [294]), **Cd(II)** (TiO_2/SiO_2 [293] and TiO_2/ZrO_2 [293]), **Ni(II)** (TiO_2 [295,296]), **U(VI)** (TiO_2 [297]), **Hg (II)** ($Ag/AgBr\text{-}Ag_2CO_3$ [298]), **Cu(II)** (ZrO_2/TiO_2 [299]), and so on.

8.6.5 Photocatalysts for CO_2 Reduction

Photocatalytic CO_2 reduction offers a strategy for converting solar energy into chemical energy and to reduce greenhouse gases produced by industrial activities.

Intensive studies have focused on the photoreduction of CO_2 to valuable fuels such as methane (CH_4), carbon monoxide (CO), methanol (CH_3OH), formic acid (HCOOH), or other compounds. Photocatalytic reduction of CO_2 with H_2O into hydrocarbon fuels such as CH_4 and CH_3OH is a reaction with a highly positive change in Gibbs free energy:

$$CO_2 + 2H_2O \rightarrow CH_3OH + 3/2O_2 (\Delta G^\circ = 702.07\ \text{kJ mol}^{-1})$$
$$\text{and } CO_2 + 2H_2O \rightarrow CH_4 + 2O_2 (\Delta G^\circ = 818.17\ \text{kJ mol}^{-1})$$

Thus, input energy is demanded to overcome these reaction barriers with the assistance of photocatalysts [300].

As illustrated in Figure 8.30 [301], photocatalytic CO_2 reduction mainly consists of five steps:

- Adsorption of CO_2 and the reductant,
- Generation of electrons (e^-) and hole (h^+) on the conduction band (CB) and valence band (VB) of the semiconductor,
- Transfer of e^- and h^+ to the surface of the catalyst,
- Reaction between the electrons/holes and the surface adsorbed species, and
- Desorption of the products and re-adsorption of the reactants.

Photocatalytic reduction of CO_2 was reported for the first time by Inoue *et al.* in 1979 [302] using various semiconductors, that is, WO_3, TiO_2, ZnO, CdS, GaP, and SiC. Since then, numerous photocatalysts have been reported for effective CO_2 reduction. Among the various proposed photocatalysts, TiO_2 and TiO_2-based heterostructures have been extensively studied over the past several decades for photocatalytic CO_2 reduction because it is cheap and environment-friendly [152,303–306]. Other various semiconductors such as MeS-based composites [307,308], g-C_3N_4-based composites [309,310], Bi_2WO_6 [311],

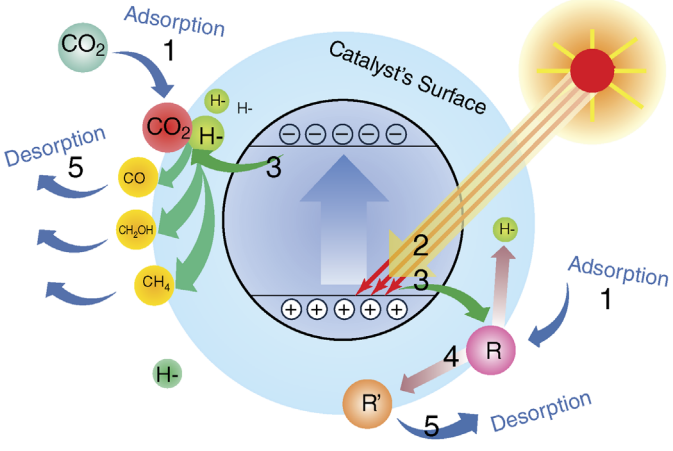

Figure 8.30 Schematic illustration of the main five steps in photocatalytically converting CO_2 with CO, CH_3OH, and CH_4 as examples of possible CO_2 reduction products (reproduced with permission from Ref. [301]. Copyright 2017, Elsevier).

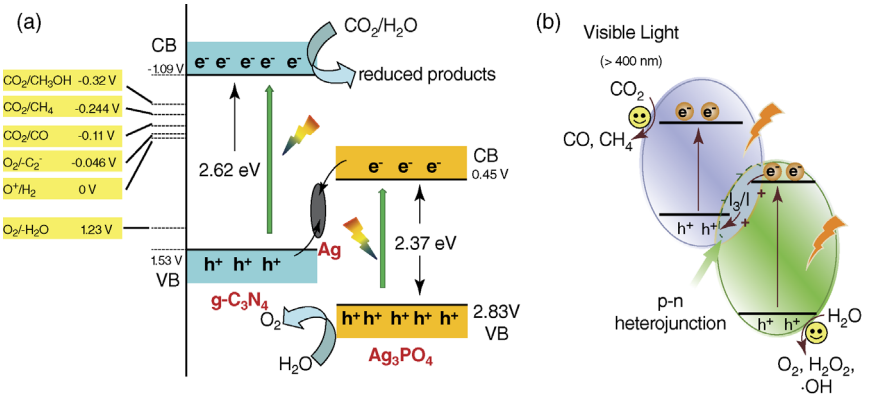

Figure 8.31 Reaction schemes for the photocatalytic reduction of CO_2 with H_2O on (a) $Ag_3PO_4/g\text{-}C_3N_4$ composite (reproduced with permission from Ref. [310]. Copyright 2015, American Chemical Society) and on (b) $BiOI/g\text{-}C_3N_4$ photocatalysts (reproduced with permission from Ref. [313]. Copyright 2016, American Chemical Society).

bismuth oxyhalides (BiOX, X = Br, I) [312–314], and so on have also been reported as photocatalysts for effective CO_2 reduction. For example, a combination of the $g\text{-}C_3N_4$ with other proper semiconductors such as Ag_3PO_4 (Figure 8.31a) and BiOI (Figure 8.31b) not only extend the visible-light absorption capacity but also improve the separation of electron–hole pairs. It provides a great enhancement of the photocatalytic activity for different hybrids and will undoubtedly help in the development of the next generation of photocatalysts for environmental applications.

References

1 Mao-Yuan, C. and Heh-Nan, L. (2015) Enhanced photocatalysis of ZnO nanowires co-modified with cuprous oxide and silver nanoparticles. *Mater. Lett.*, **160**, 440–443.

2 Sun, G., Zhu, C., Zheng, J., Jiang, B., Yin, H., Wang, H., Qiu, S., Yuan, J., Wu, M., Wu, W., and Xue, Q. (2016) Preparation of spherical and dendritic CdS@TiO2 hollow double-shelled nanoparticles for photocatalysis. *Mater. Lett.*, **166**, 113–115.

3 Richter, R., Ming, T., Davies, P., Liud, W., and Caillo, S. (2017) Removal of non-CO_2 greenhouse gases by largescale atmospheric solar photocatalysis. *Prog. Energy Combust. Sci.*, **60**, 68–96.

4 Khan, I., Saeed, K., and Khan, I. (2017) Nanoparticles: properties, applications and toxicities. *Arabian J. Chem.* doi: http://dx.doi.org/10.1016/j.arabjc.2017.05.011

5 Andrade, G.R.S., Nascimento, C., Lima, Z.M., Teixeira-Neto, E., Luiz, P., Iara, Costac, and Gimeneza, F. (2017) Star-shaped ZnO/Ag hybrid nanostructures for enhanced photocatalysis and antibacterial activity. *Appl. Surf. Sci.*, **399**, 573–582.

6 Liu, Y., Xie, C., Li, H., Chen, H., Zou, T., and Zeng, D. (2011) Improvement of gaseous pollutant photocatalysis with WO_3/TiO_2 heterojunctional-electrical layered system. *J. Hazard. Mater.*, **196**, 52–58.

7 Zhang, X., Yub, S., Liub, Y., Zhang, Q., and Zhoua, Y. (2017) Photoreduction of non-noble metal Bi on the surface of Bi_2WO_6 for enhanced visible light photocatalysis. *Appl. Surf. Sci.*, **396**, 652–658.

8 Khataee, A., Arefi-Oskoui, S., Fathinia, M., Fazli, A., Hojaghan, A.S., Hanifehpour, Y., and Joo, S.W. (2015) Photocatalysis of sulfasalazine using Gd-doped PbSe nanoparticles under visible light irradiation: kinetics, intermediate identification and phyto-toxicological studies. *J. Ind. Eng. Chem.*, **30**, 134–146.

9 Samua, G.F., Veresa, Á., Endrődia, B., Vargaa, E., Rajeshwarc, K., and Janáky, C. (2017) Bandgap-engineered quaternary $M_xBi_{2-x}Ti_2O_7$ (M: Fe, Mn) semiconductor nanoparticles: solution combustion synthesis, characterization, and photocatalysis. *Appl. Catal. B: Environ.*, **208**, 148–160.

10 Liu, M., Zhang, D., Chen, S., and Wen, T. (2016) Loading Ag nanoparticles on Cd(II) boronimidazolate framework for photocatalysis. *J. Solid State Chem.*, **237**, 32–35.

11 Asapu, R., Claes, N., Bals, S., Denys, S., Detavernierc, C., Lenaerts, S., and Verbruggena, Sammy W. (2017) Silver-polymer core-shell nanoparticles for ultra-stable plasmon-enhanced photocatalysis. *Appl. Catal. B: Environ.*, **200**, 31–38.

12 Aleksandrzak, M., Kukulk, W., and Mijowsk, E. (2017) Graphitic carbon nitride/graphene oxide/reduced graphene oxide nanocomposites for photoluminescence and photocatalysis. *Appl. Surf. Sci.*, **398**, 56–62.

13 Zhang, L., Zhang, Q., Xie, H., Guo, J., Lyu, H., Li, Y., Suna, Z., Wang, H., and Guo, Z. (2017) Electrospun titania nanofibers segregated by graphene oxide for improved visible light photocatalysis. *Appl. Catal. B*, **201**, 470–478.

14 Li, B., Zhang, B., Nie, S., Shao, L., and Hu, L. (2017) Optimization of plasmon-induced photocatalysis in electrospun Au/CeO_2 hybrid nanofibers for selective oxidation of benzyl alcohol. *J. Catal.*, **348**, 256–264.

15 Oliveira, H.G., Ferreira, L.H., Bertazzoli, R., and Longo, C. (2015) Remediation of 17-*a*-ethinylestradiol aqueous solution by photocatalysis and electrochemically assisted photocatalysis using TiO_2 and TiO_2/WO_3 electrodes irradiated by a solar simulator. *Water Res.*, **72**, 305–314.

16 Lima, Lucas V.C., Rodriguez, M., Freitas, V.A.A., Souza, T.E., Machado, A.E.H., Patrocínioc, A.O.T., Fabris, José D., Oliveira, Luiz C.A., and Pereiraa, Márcio C. (2015) Synergism between n-type WO_3 and p-type FeOOH semiconductors: High interfacial contacts and enhanced photocatalysis. *Appl. Catal. B*, **165**, 579–588.

17 Mohammadi, S., Sohrabi, M., Golikand, A.N., and Fakhri, A. (2016) Preparation and characterization of zinc and copper co-doped WO_3 nanoparticles: application in photocatalysis and photobiology. *J. Photochem. Photobiol. B*, **161**, 217–222.

18 Samokhvalov, A. (2017) Hydrogen by photocatalysis with nitrogen codoped titanium dioxide. *Renew. Sustain. Energy Rev.*, **72**, 981–1000.

19 Tang, W., Chen, X., Xia, J., Gong, J., and Zeng, X. (2014) Preparation of an Fe-doped visible-light-response TiO_2 film electrode and its photoelectrocatalytic activity. *Mater. Sci. Eng. B*, **187**, 39–45.

20 Fakhri, A. and Naji, M. (2017) Degradation photocatalysis of tetrodotoxin as a poison by gold doped PdO nanoparticles supported on reduced graphene oxide nanocomposites and evaluation of its antibacterial activity. *J. Photochem. Photobiol. B*, **167**, 58–63.

21 Zhou, R. and Srinivasan, M.P. (2015) Photocatalysis in a packed bed: degradation of organic dyes by immobilized silver nanoparticles. *J. Environ. Chem. Eng.*, **3**, 609–616.

22 Subramanyam, K., Sreelekha, N., Amaranatha Reddy, D., Murali, G., Varma, K. Rahul, and Vijayalakshmi, R.P. (2017) Chemical synthesis, structural, optical, magnetic characteristics and enhanced visible light active photocatalysis of Ni doped CuS nanoparticles. *Solid State Sci.*, **65**, 68–78.

23 Chandra, M.R., Prasada Reddy, P.S., Rao, T.S., Pammi, S.V.N., Kumar, K.S., Babub, K.V., Kumar, Ch. Kiran, and Hemalatha, K.P.J. (2017) Enhanced visible-light photocatalysis and gas sensor properties of polythiophene supported tin doped titanium nanocomposite. *J. Phys. Chem. Solids*, **105**, 99–105.

24 Friehs, E., AlSalka, Y., Jonczyk, R., Lavrentieva, A., Jochums, A., Walter, J., Stahl, F., Scheper, T., and Bahnemanna, D. (2016) Toxicity, phototoxicity and biocidal activity of nanoparticles employed in photocatalysis. *J. Photochem. Photobiol. C*, **29**, 1–28.

25 Ramesh, T., Nayak, B., Amirbahman, A., Tripp, C.P., and Mukhopadhyay, S. (2016) Application of ultraviolet light assisted titanium dioxide photocatalysis for food safety: a review. *Innovative Food Sci. Emerg. Technol.*, **38**, 105–115.

26 Wang, X., Jia, J., and Wang, Y. (2017) Combination of photocatalysis with hydrodynamic cavitation for degradation of tetracycline. *Chem. Eng. J.*, **315**, 274–282.

27 Tabib, A., Bouslama, W., Sieber, B., Addad, A., Elhouichet, H., Férida, M., and Boukherroub, R. (2017) Structural and optical properties of Na doped ZnO nanocrystals: application to solar photocatalysis. *Appl. Surf. Sci.*, **396**, 1528–1538.

28 Guana, Y., Wanga, S., Wang, X., Sund, C., Huang, Y., Liua, C., and Zhao, H. (2017) *In situ* self-assembled synthesis of Ag-AgBr/Al-MCM-41 with excellent activities of adsorption-photocatalysis. *Appl. Catal. B*, **209**, 329–338.

29 Gondal, M.A., Dastageer, M.A., and Khalil, A. (2009) Synthesis of nano-WO_3 and its catalytic activity for enhanced antimicrobial process for water purification using laser induced photo catalysis. *Catal. Commun.*, **11**, 214–219.

30 Liang, F. and Zhu, Y. (2016) Enhancement of mineralization ability for phenol via synergetic effect of photoelectrocatalysis of g-C3N4 film. *Appl. Catal. B*, **180**, 324–329.

31 Zhao, Y., Chang, W., Huang, Z., Feng, X., Ma, L., Qi, X., and Li, Z. (2017) Enhanced removal of toxic Cr (VI) in tannery wastewater by photoelectrocatalysis with synthetic TiO_2 hollow spheres. *Appl. Surf. Sci.*, **405**, 102–110.

32 Bensouici, F., Bououdina, M., Dakhel, A.A., Tala-Ighil, R., Tounane, M., Iratni, A., Souier, T., Liu, S., and Cai, W. (2017) Optical, structural and photocatalysis properties of Cu-doped TiO_2 thin films. *Appl. Surf. Sci.*, **395**, 110–116.

33 Riva, E.R., Pastoriza-Santos, I., Lak, A., Pellegrino, T., Pérez-Juste, J., and Mattoli, V. (2017) Plasmonic/magnetic nanocomposites: gold nanorods-

functionalized silica coated magnetic nanoparticles. *J. Colloid Interface Sci.*, **502**, 201–209.

34 Tan, E., Yin, P., Yu, C., Yu, G., and Zhao, C. (2016) The oxidant and laser power-dependent plasmon-driven surface photocatalysis reaction of *p*-aminothiophenol dimerizing into *p*,*p*′-dimercaptoazobenzene on Au nanoparticles. *Spectrochim. Acta, Part A*, **166**, 15–18.

35 Liu, A., Wang, G., Wang, F., and Zhang, Y. (2017) Gold nanostructures with near-infrared plasmonic resonance: synthesis and surface functionalization. *Coord. Chem. Rev.*, **336**, 28–42.

36 Choi, J., Chan, S., Joo, H., Yang, H., and Ko, K.F. (2016) Three-dimensional (3D) palladium-zinc oxide nanowire nanofiber as photo-catalyst for water treatment. *Water Res.*, **101**, 362–369.

37 Lozano, M.M., Escamilla, V.M., García, E.R., Medina, R.L., Romero, G.R., and Delgadillo, S.A.M. (2017) Sonophotocatalytic degradation of orange II dye using low cost photocatalyst. *J. Clean. Prod.*, **148**, 836–844.

38 Suligoj, A., Stangar, U.L., Ristic, A., Mazaj, M., Verhovsek, D., and Tusar, N.N. (2016) TiO_2–SiO_2 films from organic-free colloidal TiO_2 anatase nanoparticles as photocatalyst for removal of volatile organic compounds from indoor air. *Appl. Catal. B*, **184**, 119–131.

39 Fakhri, A. and Nejad, P.A. (2016) Antimicrobial, antioxidant and cytotoxic effect of Molybdenum trioxide nanoparticles and application of this for degradation of ketamine under different light illumination. *J. Photochem. Photobiol. B*, **159**, 211–217.

40 Wang, L., Ma, C., Ru, X., Guo, Z., Wu, D., Zhang, S., Yu, G., Hu, Y., and Wang, J. (2015) Facile synthesis of ZnO hollow microspheres and their high performance in photocatalytic degradation and dye sensitized solar cells. *J. Alloys Compd.*, **647**, 57–62.

41 Ollis, D. (2017) Removal kinetics of stearic acid discrete deposits on photocatalytic self-cleaning surfaces: effect of deposit initial size distribution. *Appl. Catal. B*, **209**, 174–182.

42 Yue, D., Qian, X., Kan, M., Ren, M., Zhu, Y., Jiang, L., and Zhao, Y. (2017) Sulfurated [NiFe]-based layered double hydroxides nanoparticles as efficient co-catalysts for photocatalytic hydrogen evolution using CdTe/CdS quantum dots. *Appl. Catal. B*, **209**, 155–160.

43 Gumiero, M., Peressini, D., Pizzariello, A., Sensidoni, A., Iacumin, L., Comi, G., and Toniolo, R. (2013) Effect of TiO_2 photocatalytic activity in a HDPE-based food packaging on the structural and microbiological stability of a short-ripened cheese. *Food Chem.*, **138**, 1633–1640.

44 Song, M.Y., Jurng, J., Park, Y., and Kim, B.C. (2016) An aptamer cocktail-functionalized photocatalyst with enhanced antibacterial efficiency towards target bacteria. *J. Hazard. Mater.*, **318**, 247–254.

45 Byrappa, K. and Yoshimura, M. (2001) *Handbook of Hydrothermal Technology*, Noyes Publications, New Jersey, USA.

46 Mutta, G.R., Popuri, S.R., Ruterana, P., and Buckman, J. (2017) Single step hydrothermal synthesis of mixed valent V_6O_{13} nano-architectures: a case study of the possible applications in electrochemical energy conversion. *J. Alloys Compd.*, **706**, 562–567.

47 Phuruangrat, A., Thongtem, S., and Thongtem, T. (2017) Microwave-assisted hydrothermal synthesis and characterization of CeO_2 nanowires for using as a photocatalytic material. *Mater. Lett.*, **196**, 61–63.

48 Moradiyan, E., Halladj, R., Askari, S., and Bijani, P.M. (2017) Ultrasonic-assisted hydrothermal synthesis and catalytic behavior of a novel SAPO-34/clinoptilolite nanocomposite catalyst for high propylene demand in MTO process. *J. Phys. Chem. Solids*, **107**, 83–92.

49 Che, H., Liu, X., Gao, Y., Liu, J., and Cao, Z. (2017) Sulfurated [NiFe]-based layered double hydroxides nanoparticles as efficient co-catalysts for photocatalytic hydrogen evolution using CdTe/CdS quantum dots. *J. Alloys Compd.*, **705**, 645–651.

50 Ishiguro, M. and Endo, T. (2015) Effect of the addition of calcium hydroxide on the hydrothermal–mechanochemical treatment of *Eucalyptus*. *Bioresour. Technol.*, **177**, 298–301.

51 Kashinath, L., Namratha, K., and Byrappa, K. (2017) Sol-gel assisted hydrothermal synthesis and characterization of hybrid ZnS-RGO nanocomposite for efficient photodegradation of dyes. *J. Alloys Compd.*, **695**, 799–809.

52 Andronic, L., Isac, L., Cuevas, S.M., Visa, M., Oller, I., Duta, A., and Malato, S. (2016) Pilot-plant evaluation of TiO_2 and TiO_2-based hybrid photocatalysts for solar treatment of polluted water. *J. Hazard. Mater.*, **320**, 469–478.

53 Nawaz, M., Miran, W., Jang, J., and Lee, D.S. (2017) One-step hydrothermal synthesis of porous 3D reduced graphene oxide/TiO_2 aerogel for carbamazepine photodegradation in aqueous solution. *Appl. Catal. B*, **203**, 85–95.

54 Min, S., Hou, J., Lei, Y., Ma, X., and Lu, G. (2017) Facile one-step hydrothermal synthesis toward strongly coupled TiO_2/graphene quantum dots photocatalysts for efficient hydrogen evolution. *Appl. Surf. Sci.*, **396**, 1375–1382.

55 Zhang, X., Zhang, L., Hu, J.S., Pan, C.L., and Hou, C.M. (2015) Facile hydrothermal synthesis of novel $Bi_{12}TiO_{20}$-Bi_2WO_6 heterostructure photocatalyst with enhanced photocatalytic activity. *Appl. Surf. Sci.*, **346**, 33–40.

56 Malik, R., Chaudhary, V., Tomer, V.K., Rana, P.S., Nehra, S.P., and Duhan, S. (2016) Visible light-driven mesoporous Au–TiO_2/SiO_2 photocatalysts for advanced oxidation process. *Ceram. Int.*, **42**, 10892–10901.

57 Ruiz, S.O., Gomez, R., Lopez, R., Gordillo, A.H., Avella, J.A.P., Moctezuma, E., and Perez, E. (2012) Photocatalytic reduction of methyl orange on Au/TiO_2 semiconductors. *Catal. Comm.*, **21**, 72.

58 Lin, H. and Shih, C. (2016) Efficient one-pot microwave-assisted hydrothermal synthesis of M (M = Cr, Ni, Cu, Nb) and nitrogen co-doped TiO_2 for hydrogen production by photocatalytic water splitting. *J. Mol. Catal. A*, **411**, 128–137.

59 Luo, L., Yang, Y., Zhang, A., Wang, M., Liu, Y., Bian, L., Jiang, F., and Pan, X. (2015) Hydrothermal synthesis of fluorinated anatase TiO_2/reduced graphene oxide nanocomposites and their photocatalytic degradation of bisphenol A. *Appl. Surf. Sci.*, **353**, 469–479.

60 Lei, Y. and Lu, X. (2017) The decisive effect of interface states on the photocatalytic activity of the silver(I) oxide/titanium dioxide heterojunction. *J. Colloid Interface Sci.*, **492**, 167–175.

61 Sun, X., Deng, S., Yang, Y., Xu, G., Zhao, R., Shen, G., and Han, G. (2017) Hydrothermal synthesis and photocatalytic activity of Li-doped $PbTiO_3$ perovskite cubic particles. *Surf. Coat. Technol.*, **320**, 527–530.

62 Li, M., Dai, Y., Ma, X., Jing, T., and Huang, B. (2017) Insights into the effect of inner polarization and multiple Ag-O units on high-efficient Ag-based photocatalyst. *Appl. Catal. B*, **205**, 211–218.

63 Treshchalov, A., Erikson, H., Puust, L., Tsarenko, S., Saar, R., Vanetsev, A., Tammeveski, K., and Sildos, I. (2017) Stabilizer-free silver nanoparticles as efficient catalysts for electrochemical reduction of oxygen. *J. Colloid Interface Sci.*, **491**, 358–366.

64 Li, J., Fang, W., Yu, C., Zhou, W., zhu, L., and Xie, Y. (2015) Ag-based semiconductor photocatalysts in environmental purification. *Appl. Surf. Sci.*, **358**, 46–56.

65 Lu, J., Wang, Y., Liu, F., Zhang, L., and Chai, S. (2017) Fabrication of a direct Z-scheme type WO_3/Ag_3PO_4 composite photocatalyst with enhanced visible-light photocatalytic performances. *Appl. Surf. Sci.*, **393**, 180–190.

66 Li, Z., Zhu, L., Wu, W., Wang, S., and Qiang, L. (2016) Highly efficient photocatalysis toward tetracycline under simulated solar-light by Ag^+-CDs-Bi_2WO_6: synergistic effects of silver ions and carbon dots. *Appl. Catal. B*, **192**, 277–285.

67 Adhikari, R., Gyawali, G., Sekino, T., and Lee, S.W. (2013) Microwave assisted hydrothermal synthesis of $Ag/AgCl/WO_3$ photocatalyst and its photocatalytic activity under simulated solar light. *J. Solid State Chem.*, **197**, 560–565.

68 Wang, J., Yang, X., Chen, J., Xian, J., Meng, S., Zheng, Y., Shao, Y., and Li, D. (2014) Photocatalytic activity of novel $Ag_4V_2O_7$ photocatalyst under visible light irradiation. *J. Am. Ceram. Soc.*, **97**, 267–274.

69 Maruyama, Y., Irie, H., and Hashimoto, K. (2006) Visible light sensitive photocatalyst, delafossite structured α-$AgGaO_2$. *J. Phys. Chem. B*, **110**, 23274–23278.

70 Dai, G., Yu, J., and Liu, G. (2012) A new approach for photocorrosion inhibition of Ag_2CO_3 photocatalyst with highly visible-light-responsive reactivity. *J. Phys. Chem. C*, **116**, 15519–15524.

71 Bi, Y., Hu, H., Ouyang, S., Lu, G., Cao, J., and Ye, J. (2012) Photocatalytic and photoelectric properties of cubic Ag_3PO sub-microcrystals with sharp corners and edges. *Chem. Commun.*, **48**, 3748–3750.

72 Duo, S., Li, Y., Liu, Z., Zhong, R., and Liu, T. (2016) Novel hybrid self-assembly of an ultralarge ZnO macroflower and defect intensity-induced photocurrent and photocatalytic properties by facile hydrothermal synthesis using $CO(NH_2)_2$-N_2H_4 as alkali sources. *Mat. Sci. Semicon. Proc.*, **56**, 196–212.

73 Arnold, M.S., Avouris, P., Pan, Z.W., and Wang, Z.L. (2003) Field-effect transistors based on single semiconducting oxide nanobelts. *J. Phys. Chem. B*, **107**, 659–663.

74 Rao, G.S.T. and Rao, D.T. (1999) Gas sensitivity of ZnO based thick film sensor to NH_3 at room temperature. *Sens. Actuators B*, **55**, 166–169.

75 Lee, C.J., Lee, T.J., Lyu, S.C., Zhang, Y., Ruh, H., and Lee, H.J. (2002) Field emission from well-aligned zinc oxide nanowires grown at low temperature. *Appl. Phys. Lett.*, **81**, 3648–3650.

76 Tominaga, K., Umezu, N., Mori, I., Ushiro, T., Moriga, T., and Nakabayashi, I. (1998) Transparent conductive ZnO film preparation by alternating sputtering of ZnO:Al and Zn or Al targets. *Thin Solid Films*, **334**, 35–39.

77 Huang, M.H., Mao, S., Feick, H., Yan, H., Wu, Y., Kind, H., Weber, E., Russo, R., and Yang, P. (2001) Room temperature ultraviolet nanowire nanolasers. *Supramol. Sci.*, **292**, 1897–1899.

78 Yan, Y., Liu, P., Wen, J.G., To, B., and Al-Jassim, M.M. (2003) *In-situ* formation of ZnO nanobelts and metallic Zn nanobelts and nanodisks. *J. Phys. Chem. B*, **107**, 9701–9704.

79 Yu, H., Zhang, Z., Han, M., Hao, X., and Zhu, F. (2005) A general low-temperature route for large scale fabrication of highly oriented ZnO nanorod/nanotube arrays. *J. Am. Chem. Soc.*, **127**, 2378–2379.

80 Peng, Y., Xu, A.W., Deng, B., Antonietti, M., and lfen, H.C. (2006) Polymer-controlled crystallization of zinc oxide hexagonal nanorings and disks. *J. Phys. Chem. B*, **110**, 2988–2993.

81 Sen, S., Guy, T.N., and Ozacar, M. (2017) Photocatalytic efficiencies of Ni, Mn, Fe and Ag doped ZnO nanostructures synthesized by hydrothermal method: the synergistic/antagonistic effect between ZnO and metals. *J. Photochem. Photobiol. A*, **341**, 39–50.

82 Xing, Z., Chen, Y., Liu, C., Yang, J., Xu, J., Situ, Y., and Huang, H. (2017) Synthesis of core–shell ZnO/oxygen doped g-C_3N_4 visible light driven photocatalyst *via* hydrothermal method. *J. Alloys Compd.*, **708**, 853–861.

83 Fuentes, S., Muñoz, P., Llanos, J., Vega, M., Martin, I.R., and Chavez-Angel, E. (2017) Synthesis and optical characterization of Er-doped bismuth titanate nanoparticles grown by sol–gel hydrothermal method. *Ceram. Int.*, **43**, 3623–3630.

84 Xu, X., Li, S., Wang, X., Ma, Y., Wang, X., and Gao, K. (2015) Fabrication and characterization of $Ca_2Fe_2O_5$ nanofibers photocatalyst by sol-gel assisted electrospinning at low-temperature. *Mater. Lett.*, **143**, 75–79.

85 Shen, H., Xue, T., Wang, Y., Cao, G., Lu, Y., and Fang, G. (2016) Photocatalytic property of perovskite $LaFeO_3$ synthesized by sol-gel process and vacuum microwave calcinations. *Mater. Res. Bull.*, **84**, 15–24.

86 Zhang, D., Zhang, L., and Taiwan, J. (2016) Ultrasonic-assisted sol–gel synthesis of rugby-shaped $SrFe_2O_4$/reduced graphene oxide hybrid as versatile visible light photocatalyst. *J. Taiwan Inst. Chem. Eng.*, **69**, 1–7.

87 Zhang, W., Pei, X., Chen, J., and He, H. (2015) Effects of Al doping on properties of *x*Al–3%In–TiO_2 photocatalyst prepared by a sol–gel method. *Mater. Sci. Semicond. Process*, **38**, 24–30.

88 Mitra, M., Ghosh, A., Mondal, A., Kargupta, K., Ganguly, S., and Banerjee, D. (2017) Facile synthesis of aluminium doped zinc oxide-polyaniline hybrids for photoluminescence and enhanced visible-light assisted photo-degradation of organic contaminants. *Appl. Surf. Sci.*, **402**, 418–428.

89 Niasari, M.S., Soofivand, F., Nasab, A.S., Arani, M.S., Faal, A.Y., and Bagheri, S. (2016) Synthesis, characterization, and morphological control of $ZnTiO_3$ nanoparticles through sol-gel processes and its photocatalyst application. *Adv. Powder Technol.*, **27**, 2066–2075.

90 Li, C., Sun, Z., Xue, Y., Yao, G., and Zheng, S. (2016) A facile synthesis of g-C_3N_4/TiO_2 hybrid photocatalysts by sol–gel method and its enhanced photodegradation towards methylene blue under visible light. *Adv. Powder Technol.*, **27**, 330–337.

91 Balasubramanyam, A., Sailaja, N., Mahboob, M., Rahman, M.F., Hussain, S.M., and Grover, P. (2010) *In vitro* mutagenicity assessment of aluminium oxide nanomaterials using the *Salmonella*/microsome assay. *Toxicol. in Vitro*, **24**, 1871–1876.

92 Jung, Y.S., Kim, D.W., Kim, Y.S., Park, E.K., and Baeck, S.H. (2008) Synthesis of alumina–titania solid solution by sol–gel method. *J. Phys. Chem. Solids*, **69**, 1464–1467.

93 Tzompantzi, F., Pina, Y., Mantilla, A., Aguilar-Martinez, O., Hernandez, F.G., Bokhimi, X., and Barrera, A. (2014) Hydroxylated sol–gel Al_2O_3 as photocatalyst for the degradation of phenolic compounds in presence of UV light. *Catal. Today*, **220**, 49–55.

94 Ziolo, R.F., Giannelis, E.P., Weinstein, B.A., O'Horo, M.P., Ganguli, B.N., and Mehrotra, V. (1992) Matrix-mediated synthesis of nanocrystalline ggr-Fe_2O_3: a new optically transparent magnetic material. *Science*, **257**, 219–223.

95 Alivisatos, P. (1996) Semiconductor clusters, nanocrystals and quantum dots. *Science*, **271**, 933–937.

96 Berkovsky, M.V., Medvedev, F.V., and Krakov, S.M. (1993) *Magnetic Fluids Engineering Applications*, Oxford University Press, Oxford, UK.

97 Manova, E., Tsoncheva, T., Paneva, D., Mitov, I., Tenchev, K., and Petrov, L. (2004) Mechanochemically synthesized nano-dimensional iron–cobalt spinel oxides as catalysts for methanol decomposition. *Appl. Catal. A*, **277**, 119–127.

98 Satyanarayana, L., Reddy, K.M., and Manorama, S.V. (2003) Nanosized spinel $NiFe_2O_4$: a novel material for the detection of liquefied petroleum gas in air. *Mater. Chem. Phys.*, **82**, 21–26.

99 Kulkarni, G.U., Kannan, K.R., Arunarkavalli, T., and Rao, C.N.R. (1994) Particle-size effects on the value of Tc of $MnFe_2O_4$: evidence for finite-size scaling. *Phys. Rev. B*, **49**, 724–727.

100 Viroonchatapan, E., Ueno, M., Sato, H., Adachi, I., Nagae, H., Tazawa, K., and Horikoshi, I. (1995) Preparation and characterization of dextran magnetite-incorporated thermosensitive liposomes: an on-line flow system for quantifying magnetic responsiveness. *Pharm. Res.*, **12**, 1176–1183.

101 Rao, K.J., Vaidhyanathan, B., Ganguli, M., and Ramakrishnan, P.A. (1999) Synthesis of inorganic solids using microwaves. *Chem. Mater.*, **11**, 882–895.

102 Verma, S., Joy, P.A., Khollam, Y.B., Potdar, H.S., and Deshpande, S.B. (2004) Synthesis of nanosized $MgFe_2O_4$ powders by microwave hydrothermal method. *Mater. Lett.*, **58**, 1092–1095.

103 Zhao, Y., Huang, Z., Chang, W., Wei, C., Feng, X., Ma, L., Qi, X., and Li, Z. (2017) Microwave-assisted solvothermal synthesis of hierarchical TiO_2 microspheres for efficient electro-field-assisted-photocatalytic removal of tributyltin in tannery wastewater. *Chemosphere*, **179**, 75–83.

104 Li, J., Huang, J., Wu, J., Cao, L., and Li, Q., and Yanagisawa, K. (2013) Microwave-assisted growth of $WO_3 \cdot 0.33H_2O$ micro/nanostructures with

enhanced visible light photocatalytic properties. *Cryst. Eng. Comm.*, **15**, 7904–7913.

105 Li, Q. and Hai, P. (2014) Rapid microwave-assisted synthesis of silver decorated-reduced graphene oxide nanoparticles with enhanced photocatalytic activity under visible light. *Mater. Sci. Semicond. Process*, **22**, 16–20.

106 Darvishi, M., Asgerani, G.M., and Yazdi, J.S. (2017) Simple microwave irradiation procedure for the synthesis of CuO/graphene hybrid composite with significant photocatalytic enhancement. *Surf. Interfaces*, **7**, 69–73.

107 Somsri, S., Sonwaew, W., and Rujiwatra, A. (2016) *Psidium guajava* Linn. extract mediated microwave synthesis and photocatalytic activities of ZnO nanoparticles. *Mater. Lett.*, **177**, 124–127.

108 Pomar, F.S., Jaramillo, A., Villareal, J.L., Medina, C., Rojas, D., Mera, A.C., Melendrez, M.F., and Tijerina, E.P. (2016) Rapid synthesis and photocatalytic activity of ZnO nanowires obtained through microwave-assisted thermal decomposition. *Ceram. Int.*, **42**, 18045–18052.

109 Flores, U.C., Romero, J.L., Medina, J.Z., Batista, M.J.M., Acuna, R.H., Munoz, E.M.R., and Cortes, J.A. (2016) Enhanced photocatalytic activity of MWCNT/TiO_2 heterojunction photocatalysts obtained by microwave assisted synthesis. *Catal. Today*, **266**, 102–109.

110 George, P., Dhabarde, N.R., and Chowdhury, P. (2017) Rapid synthesis of titanium based metal organic framework (MIL-125) via microwave route and its performance evaluation in photocatalysis. *Mater. Lett.*, **186**, 151–154.

111 Ghanbari, M., Soofivand, F., and Niasari, M.S. (2016) Simple synthesis and characterization of Ag_2CdI_4/AgI nanocomposite as an effective photocatalyst by co-precipitation method. *J. Mol. Liq.*, **223**, 21–28.

112 Hu, Y.L., Wu, Z., Zheng, X., Lin, N., Yang, Y., Zuo, J., Sun, D., Jiang, C., Sun, L., Lin, C., and Fu, Y. (2017) ZnO/ZnGaNO heterostructure with enhanced photocatalytic properties prepared from a LDH precursor using a coprecipitation method. *J. Alloys Compd.*, **709**, 42–53.

113 Vinosha, P.A., Mely, L.A., Jeronsia, J.E., Krishnan, S., and Das, S.J. (2017) Synthesis and properties of spinel $ZnFe_2O_4$ nanoparticles by facile co-precipitation route. *Optik*, **134**, 99–108.

114 Quan, X., Zhao, Q., Tan, H., Sang, X., Wang, F., and Dai, Y. (2009) Comparative study of lanthanide oxide doped titanium dioxide photocatalysts prepared by coprecipitation and sol-gel process. *Mater. Chem. Phy.*, **114**, 90–98.

115 Moffett, J.W. and Zika, R.G. (1987) *Photochemistry of Environmental Aquatic Systems*, Advances in Chemistry Series 327, American Chemical Society, Washington, DC, p. 116.

116 Ejhieh, A.N. and Shamsabadi, M.K. (2014) Comparison of photocatalytic efficiency of supported CuO onto micro and nano particles of zeolite X in photodecolorization of methylene blue and methyl orange aqueous mixture. *Appl. Catal. A*, **477**, 83–92.

117 Sykora, J., Kovacova, J., Brandsteterova, E., and Jabconova, A. (1993) *Contributions to Development of Coordination Chemistry* (eds G. Ondrejovic and A. Sirota), Slovak Technical University Press, Bratislava, p. 385.

118 Sykora, J., Jakubcova, M., and Cvengrosova, Z. (1982) Photooxidation effect of cupric complexes on aliphatic alcohols in nonaqueous solutions. *Collect. Czech. Chem. Commun*, **47**, 2061.

119 Guan, H., Hou, H., Li, M., and Cui, J. (2017) Photocatalytic and thermoelectric properties of Cu_2MnSnS_4 nanoparticles synthesized via solvothermal method. *Mater. Lett.*, **188**, 319–322.

120 Wang, M., Guo, P., Chai, T., Xie, Y., Han, J., You, M., Wang, Y., and Zhu, T. (2017) Effects of Cu dopants on the structures and photocatalytic performance of cocoon-like Cu-$BiVO_4$ prepared via ethylene glycol solvothermal method. *J. Alloys Compd.*, **691**, 8–14.

121 Wei, Q., Yan, J., Ren, X., Ren, X., and Liu, S. (2015) Synthesis of hierarchical structure Cu_2SnSe_3 microsphere by a solvothermal method. *Mater. Lett.*, **161**, 727–730.

122 Zdravkov, A., Kudryashova, J., Kanaev, A., Povolotskiy, A., Volkova, A., Golikova, E., and Khimich, N. (2015) A new solvothermal route to efficient titania photocatalyst. *Mater. Chem. Phys.*, **160**, 73–79.

123 Faccenda, M. and Zilio, L.D. (2017) *The Role of Solid–Solid Phase Transitions in Mantle Convection*, vol. 268–271, Lithos, pp. 198–224.

124 Fujihara, K., Ohno, T., and Matsumura, M. (1998) Splitting of water by electrochemical combination of two photocatalytic reactions on TiO_2 particles. *J. Chem. Soc. Faraday Trans.*, **94**, 3705.

125 Gratzel, M. (2005) Solar energy conversion by dye-sensitized photovoltaic cells. *Inorg. Chem.*, **44**, 6841.

126 Muggli, D.S. and Ding, L. (2001) Photocatalytic performance of sulfated TiO_2 and Degussa P-25 TiO_2 during oxidation of organics. *Appl. Catal. B*, **32**, 181.

127 Bessekhouad, Y., Robert, D., and Weber, J.V. (2003) Preparation of TiO_2 nanoparticles by sol-gel route. *Int. J. Photoenergy*, **5**, 153.

128 Matthews, R.W. (1987) Photooxidation of organic impurities in water using thin films of titanium dioxide. *J. Phys. Chem.*, **91**, 3328.

129 Mills, A., Lepre, A., Elliott, N., Bhopal, S., Parkin, I.P., and O'Neill, S.A. (2003) Characterisation of the photocatalyst, Pilkington Activ™: a reference film photocatalyst? *J. Photochem. Photobiol. A*, **160**, 213.

130 Mitoraj, D., Janczyk, A., Strus, M., Kisch, H., Stochel, G., Heczko, P.B., and Macyk, W. (2007) Visible light inactivation of bacteria and fungi by modified titanium dioxide. *Photochem. Photobiol. Sci.*, **6**, 642.

131 Fox, M.A. and Dulay, M.T. (1993) Heterogeneous photocatalysis. *Chem. Rev.*, **93**, 341.

132 Fujihira, M., Satoh, Y., and Osa, T. (1981) Heterogeneous photocatalytic oxidation of aromatic compounds on TiO_2. *Nature*, **293**, 206.

133 Hotsenpiller, P.A.M., Bolt, J.D., Farneth, W.E., Lowekamp, J.B., and Rohrer, G.S. (1998) Orientation dependence of photochemical reactions on TiO_2 surfaces. *J. Phys. Chem. B*, **102**, 3216.

134 Gruy, F. and Pijolat, M. (1992) Kinetics of anatase TiO_2 surface area reduction in a mixture of HCl, H_2O, and O_2: l, experimental study. *J. Am. Ceram. Soc*, **75**, 657.

135 Okada, K., Yamamoto, N., Kameshima, Y., and Yasumori, A. (2001) Effect of silica additive on the anatase-to-rutile phase transition. *J. Am. Ceram. Soc.*, **84**, 1591.

136 Matthews, A. (1976) The crystallization of anatase and rutile from amorphous titanium dioxide under hydrothermal conditions. *Am. Miner.*, **61**, 419.

137 Zhang, H. and Banfield, J.F. (1998) Thermodynamic analysis of phase stability of nanocrystalline titania. *J. Mater. Chem.*, **8**, 2073.

138 Bacsa, R.R. and Kiwi, J. (1998) Effect of rutile phase on the photocatalytic properties of nanocrystalline titania during the degradation of *p*-coumaric acid. *Appl. Catal. B*, **16**, 19.

139 Kumar, K.N.P., Keizer, K., and Burggraaf, A.J. (1994) Stabilization of the porous texture of nanostructured titania by avoiding a phase transformation. *J. Mater. Sci. Lett.*, **13**, 59.

140 Hirano, M., Nakahara, N., Ota, K., Tanaike, O., and Inagaki, N. (2003) Photoactivity and phase stability of ZrO_2-doped anatase-type TiO_2 directly formed as nanometer-sized particles by hydrolysis under hydrothermal conditions. *J. Solid State Chem.*, **170**, 39.

141 Carp, O., Huisman, C.L., and Reller, A. (2004) Photoinduced reactivity of titanium dioxide. *Prog. Solid State Chem.*, **21**, 33.

142 Shannon, R.D. and Pask, J.A. (1965) Kinetics of the anatase-rutile formation. *J. Am. Ceram. Soc.*, **48**, 391.

143 Penn, R.L. and Banfield, J.F. (1999) Formation of rutile nuclei at anatase {112} twin interfaces and the phase transformation mechanism in nanocrystalline titania. *Am. Miner.*, **84**, 871.

144 Zhang, Z., Wang, C., Zakaria, R., and Ying, J. (1998) Role of particle size in nanocrystalline TiOi-based photocatalysts. *J. Phys. Chem. B*, **102**, 10871.

145 Zhang, H. and Banfield, J.F. (2000) Understanding polymorphic phase transformation behavior during growth of nanocrystalline aggregates: insights from TiO_2. *J. Phys. Chem. B*, **104**, 3481.

146 Ding, X. and Li, X. (1998) Correlation between anatase to rutile transformation and grain growth in nanocrystalline titania powders. *J. Mater. Res.*, **13**, 2556.

147 Gouma, P.I. and Mills, M.J. (2001) Anatase-to-rutile transformation in titania powders. *J. Am. Ceram. Soc.*, **84**, 619.

148 Zhang, Q., Gao, L., and Guo, J. (2000) Effects of calcinations on the photocatalytic properties of nanosized TiO_2 powders prepared by $TiCl_4$ hydrolysis. *Appl. Catal. B*, **26**, 207.

149 Han, J., Zhu, G., Hojamberdiev, M., Peng, J., and Liu, P. (2016) Temperature effect on phase transition and morphological transformation of BiOI microspheres to Bi_5O_7I microstructures. *Mater. Lett.*, **169**, 122–125.

150 Tian, B., Li, C., and Zhang, J. (2012) One-step preparation, characterization and visible-light photocatalytic activity of Cr-doped TiO_2 with anatase and rutile bicrystalline phases. *Chem. Eng. J.*, **191**, 402–409.

151 Lei, X.F., Xue, X.X., Yang, H., Chen, C., Li, X., Niu, M.C., Gao, X.Y., and Yang, Y.T. (2015) Effect of calcinations temperature on the structure and visible-light photocatalytic activities of (N, S and C) co-doped TiO_2 nano-materials. *Appl. Surf. Sci.*, **332**, 172–180.

152 Reli, M., Kobielusz, M., Matějová, L., Daniš, S., Macyk, W., Obalová, L., Kuśtrowski, P., Rokicińska, A., and Kočí, K. (2017) TiO_2 Processed by pressurized hot solvents as a novel photocatalyst for photocatalytic reduction of carbon dioxide. *Appl. Surf. Sci.*, **391**, Part B, 282–287.

153 Baran, T., Wojtyła, S., Dibenedetto, A., Aresta, M., and Macyk, W. (2016) Photocatalytic carbon dioxide reduction at p-type copper(I) iodide. *ChemSusChem*, **9**, 2933.

154 Qiu, F., Zhu, X., Guo, Q., Dai, Y., Xu, J., and Zhang, T. (2017) Fabrication of a novel hierarchical flower-like hollow structure Ag_2WO_4/WO_3 photocatalyst and its enhanced visible-light photocatalytic activity. *Powder Technol.*, **317**, 287–292.:

155 Wu, X., Zhao, J., Wang, L., Han, M., Zhang, M., Wang, H., Huang, H., Liu, Y., and Kang, Z. (2017) Carbon dots as solid-state electron mediator for $BiVO_4$/CDs/CdS Z-scheme photocatalyst working under visible light. *Appl. Catal. B*, **206**, 501–509.

156 Li, H., Su, Z., Hu, S., and Yan, Y. (2017) Free-standing and flexible Cu/Cu_2O/CuO heterojunction net: a novel material as cost-effective and easily recycled visible-light photocatalyst. *Appl. Catal. B*, **207**, 134–142.

157 Chen, J., Zhong, J., Li, J., Huang, S., Hu, W., Li, M., and Du, Q. (2017) Synthesis and characterization of novel $Ag_2CO_3/g\text{-}C_3N_4$ composite photocatalysts with excellent solar photocatalytic activity and mechanism insight. *J. Mol. Catal.*, **435**, 91–98.

158 Ameta, R. and Ameta, S.C. (2016) *Photocatalysis: Principles and Applications*, CRC Press, 339 p.

159 Hernández-Ramírez, A. and Medina-Ramirez., I. (2015) *Photocatalytic Semiconductors: Synthesis, Characterization, and Environmental Applications*, Springer International Publishing, p., 289.

160 Morrison, S.R. (1980) *Electrochemistry at Semiconductor and Oxidized Metal Electrode*, Plenum, New York.

161 Zhang, X., Tang, A., Jia, Y., Wang, Y., Wang, H., and Zhang, S. (2017) Enhanced visible-light-driven photocatalytic performance of $Ag/AgGaO_2$ metal semiconductor heterostructures. *J. Alloys Compd.*, **701**, 16–22.

162 Lamba, R., Umar, A., Mehta, S.K., and Kansal, S.K. (2017) Enhanced visible light driven photocatalytic application of Ag_2O decorated ZnO nanorods heterostructures. *Sep. Purif. Technol.*, **183**, 341–349.

163 Jiang, D., Xue, J., Wu, L., Zhou, W., Zhang, Y., and Li, X. (2017) Photocatalytic performance enhancement of CuO/Cu_2O heterostructures for photodegradation of organic dyes: effects of CuO morphology. *Appl. Catal. B*, **211**, 199–204.

164 Zhang, J. and Nosaka, Y. (2015) Generation of OH radicals and oxidation mechanism in photocatalysis of WO_3 and $BiVO_4$ powders. *J. Photochem. Photobiol. A*, **303–304**, 53–58.

165 Qamar, M., Alhooshani, K., Ahmed, M.I., Azad, A.-M., and Merzougui, B. (2015) Amelioration in the visible-light-driven photocatalysis by faceted WO_3 nanocuboids. *Catal. Commun.*, **70**, 21–25.

166 Yuan, Y., Huang, G.-F., Hu, W.-Y., Xiong, D.-N., Zhou, B.-X., Chang, S., and Huang, W.-Q. (2017) Construction of $g\text{-}C_3N_4/CeO_2/ZnO$ ternary photocatalysts with enhanced photocatalytic performance. *J. Phys. Chem. Solids*, **106**, 1–9.

167 Qin, J., Li, R., Lu, C., Jiang, Y., Tang, H., and Yang, X. (2015) Ag/ZnO/graphene oxide heterostructure for the removal of rhodamine B by the synergistic adsorption–degradation effects. *Ceram. Int.*, **41** (3), Part A, 4231–4237.

168 Dou, P., Tan, F., Wang, W., Sarreshteh, A., Qiao, X., Qiu, X., and Chen, J. (2015) One-step microwave-assisted synthesis of Ag/ZnO/graphene nanocomposites with enhanced photocatalytic activity. *J. Photochem. Photobiol. A*, **302**, 17–22.

169 Liu, Y., Wei, S., and Gao, W. (2015) Ag/ZnO heterostructures and their photocatalytic activity under visible light: effect of reducing medium. *J. Hazard. Mater.*, **287**, 59–68.

170 Liu, H., Hu, Y., Zhang, Z., Liu, X., Jia, H., and Xu, B. (2015) Synthesis of spherical Ag/ZnO heterostructural composites with excellent photocatalytic activity under visible light and UV irradiation. *Appl. Surf. Sci.*, **355**, 644–652.

171 Meng, A., Xing, J., Li, Z., Wei, Q., and Li, Q. (2016) Ag/AgCl/ZnO nano-networks: preparation, characterization, mechanism and photocatalytic activity. *J. Mol. Catal. A*, **411**, 290–298.

172 Cao, W. (2016) *Semiconductor Photocatalysis: Materials, Mechanisms and Applications*, InTech, p., 674.

173 Yuyang, S., Long, J., Tian, Z., Jin, W., Ling, L., Yong, J., Zhifeng, J., and Xiaosong, S. (2015) Synthesis of Au–ZnO hybrid nanostructure arrays and their enhanced photocatalytic activity. *New J. Chem.*, **39**, 2943–2948.

174 Wu, Z., Xue, Y., Wang, H., Wu, Y., and Yu., H. (2014) ZnO nanorods/Pt and ZnO nanorods/Ag heteronanostructure arrays with enhanced photocatalytic degradation of dyes. *RSC Adv.*, **4**, 59009–59016.

175 Xie, M.-Y., Su, K.-Y., Peng, X.-Y., Wu, R.-J., Chavali, M., and Chang, W.-C. (2017) Hydrogen production by photocatalytic water-splitting on Pt-doped TiO_2–ZnO under visible light. *J. Taiwan Inst. Chem. Eng.*, **70**, 161–167.

176 Muñoz-Fernandez, L., Sierra-Fernandez, A., Milošević, O., and Rabanal, M.E. (2016) Solvothermal synthesis of Ag/ZnO and Pt/ZnO nanocomposites and comparison of their photocatalytic behaviors on dyes degradation. *Adv. Powder Technol.*, **27** (3), 983–993.

177 Morales-Flores, N., Pal, U., and Sánchez Mora, E. (2011) Photocatalytic behavior of ZnO and Pt-incorporated ZnO nanoparticles in phenol degradation. *Appl. Catal. A*, **394** (1–2), 269–275.

178 He, W., Kim, H.-K., Wamer, W.G., Melka, D., Callahan, J.H., and Yin, J.-J. (2014) Photogenerated charge carriers and reactive oxygen species in ZnO/Au hybrid nanostructures with enhanced photocatalytic and antibacterial activity. *J. Am. Chem. Soc.*, **136** (2), 750–757.

179 Roy, P., Periasamy, A.P., Liang, C.-T., and Chang, H.-T. (2013) Synthesis of graphene-ZnO-Au nanocomposites for efficient photocatalytic reduction of nitrobenzene. *Environ. Sci. Technol.*, **47** (12), 6688–6695.

180 Li, P., Wei, Z., Wu, T., Peng, Q., and Li., Y. (2011) Au–ZnO hybrid nanopyramids and their photocatalytic properties. *J. Am. Chem. Soc.*, **133** (15), 5660–5663.

181 Fageria, P., Gangopadhyay, S., and Pande, S. (2014) Synthesis of ZnO/Au and ZnO/Ag nanoparticles and their photocatalytic application using UV and visible light. *RSC Adv.*, **4**, 24962.

182 Wu, S., Chen, Z., Wang, T., and Ji, X. (2017) A facile approach for the fabrication of Au/ZnO-hollow-sphere-monolayer thin films and their photocatalytic properties. *Appl. Surf. Sci.*, **412**, 69–76.

183 Lee, J.-E., Khoa, N.T., Kim, S.W., Kim, E.J., and Hahn, S.H. (2015) Fabrication of Au/GO/ZnO composite nanostructures with excellent photocatalytic performance. *Mater. Chem. Phys.*, **164**, 29–35.

184 Dhatshanamurthi, P. and Shanthi, M. (2017) Enhanced photocatalytic degradation of azo dye in aqueous solutions using Ba@Ag@ZnO nanocomposite for self-sensitized under sunshine irradiation. *Int. J. Hydrogen Energy*, **42** (8), 5523–5536.

185 Pirhashemi, M. and Habibi-Yangjeh, A. (2017) Ultrasonic-assisted preparation of plasmonic ZnO/Ag/Ag_2WO_4 nanocomposites with high visible-light photocatalytic performance for degradation of organic pollutants. *J. Colloid Interface Sci.*, **491**, 216–229.

186 Hu, X., Xu, Q.C., Ge, C., Su, N., Zhang, J., Huang, H., Zhu, S., Xu, Y., and Cheng, J. (2017) Synthesis and photocatalytic activity of Pt–ZnO hybrid nanocomposite by solution plasma technology. *Nanotechnology*, **28** (4), 045604. (8pp).

187 Jedsukontorn, T., Saito, N., and Hunsom, M. (2017) Photocatalytic behavior of metal-decorated TiO_2 and their catalytic activity for transformation of glycerol to value added compounds. *J. Mol. Catal.*, **432**, 160–171.

188 Grabowskaa, E., Diak, M., Klimczuk, T., Lisowski, W., and Zaleska-Medynska, A. (2017) Novel decahedral TiO_2 photocatalysts modified with Ru or Rh NPs: insight into the mechanism. *J. Mol. Catal.*, **434**, 154–166.

189 Utsunomiya, A., Okemoto, A., Nishino, Y., Kitagawa, K., Kobayashi, H., Taniya, K., Ichihashi, Y., and Nishiyama, S. (2017) Mechanistic study of reaction mechanism on ammonia photodecomposition over Ni/TiO_2 photocatalysts. *Appl. Catal. B*, **206**, 378–383.

190 Faraji, M. and Mohaghegh, N. (2016) Ag/TiO_2-nanotube plates coated with reduced graphene oxide as photocatalysts. *Surf. Coat. Technol.*, **288**, 144–150.

191 Mohamed, M.M. and Al-Sharif, M.S. (2013) Visible light assisted reduction of 4-nitrophenol to 4-aminophenol on Ag/TiO_2 photocatalysts synthesized by hybrid templates. *Appl. Catal. B*, **142–143**, 432–441.

192 Zhang, L., Wang, W., Zhou, L., Shang, M., and Sun, S. (2009) Fe_3O_4 coupled BiOCl: a highly efficient magnetic photocatalyst. *Appl. Catal. B*, **90** (3–4), 458–462.

193 Tatarchuk, T.R., Bououdina, M., Paliychuk, N.D., Yaremiy, I.P., and Moklyak, V.V. (2017) Structural characterization and antistructure modeling of cobalt-substituted zinc ferrites. *J. Alloys Compd.*, **694**, 777–791.

194 Tatarchuk, T., Bououdina, M., Macyk, W., Shyichuk, O., Paliychuk, N., Yaremiy, I., Al-Najar, B., and Pacia, M. (2017) Structural, optical, and magnetic properties of Zn-doped $CoFe_2O_4$ nanoparticles. *Nanoscale Res. Lett.*, **12**, 141.

195 Zhang, D., Cui, S., and Yang, J. (2017) Preparation of Ag_2O/g-C_3N_4/Fe_3O_4 composites and the application in the photocatalytic degradation of rhodamine B under visible light. *J. Alloys Compd.*, **708**, 1141–1149.

196 Liu, M., Hou, L., Xi, B., Li, Q., Hu, X., and Yu, S. (2016) Magnetically separable Ag/AgCl-zero valent iron particles modified zeolite X heterogeneous photocatalysts for tetracycline degradation under visible light. *Chem. Eng. J.*, **302**, 475–484.

197 Padmapriya, G., Manikandan, A., Krishnasamy, V. *et al.* (2016) Enhanced catalytic activity and magnetic properties of spinel $Mn_xZn_{1-x}Fe_2O_4$ ($0.0 \leq x \leq 1.0$) nano-photocatalysts by microwave irradiation route. *J. Supercond. Nov. Magn.*, **29**, 2141.

198 Harish, K.N., Bhojya Naik, H.S., Prashanth Kumar, P.N., and Viswanath, R. (2013) Optical and photocatalytic properties of solar light active Nd-substituted Ni ferrite catalysts: for environmental protection. *ACS Sust. Chem. Eng.*, **1** (9), 1143–1153.

199 Sun, T., Zhao, Z., Liang, Z., Liu, J., Shi, W., and Cui, F. (2017) Efficient removal of arsenite through photocatalytic oxidation and adsorption by ZrO_2-Fe_3O_4 magnetic nanoparticles. *Appl. Surf. Sci.* doi: 10.1016/j.apsusc.2017.04.137.

200 Wang, X., Wang, A., and Ma, J. (2017) Visible-light-driven photocatalytic removal of antibiotics by newly designed C_3N_4@$MnFe_2O_4$-graphene nanocomposites. *J. Hazard. Mater.*, **336**, 81–92.

201 Fu, Y., Xiong, P., Chen, H., Sun, X., and Wang, X. (2012) High photocatalytic activity of magnetically separable manganese ferrite–graphene heteroarchitectures. *Ind. Eng. Chem. Res.*, **51** (2), 725–731.

202 Fu, Y., Chen, Q., He, M., Wan, Y., Sun, X., Xia, H., and Wang, X. (2012) Copper ferrite-graphene hybrid: a multifunctional heteroarchitecture for photocatalysis and energy storage. *Ind. Eng. Chem. Res.*, **51** (36), 11700–11709.

203 Fu, Y.S. and Wang, X. (2011) Magnetically separable $ZnFe_2O_4$-graphene catalyst and its high photocatalytic performance under visible light irradiation. *Ind. Eng. Chem. Res.*, **50**, 7210–7217.

204 Fu, Y., Chen, H., Sun, X., and Wang, X. (2012) Graphene-supported nickel ferrite: a magnetically separable photocatalyst with high activity under visible light. *AIChE J.*, **58**, 3298–3305.

205 Fu, Y., Chen, H., Sun, X., and Wang, X. (2012) Combination of cobalt ferrite and graphene: high-performance and recyclable visible-light photocatalysis. *Appl. Catal. B*, **111–112**, 280–287.

206 Li, K., Chen, R., Li, S.-L., Xie, S.-L., Cao, X.-L., Dong, L.-Z., Bao, J.-C., and Lan, Y.-Q. (2016) Engineering the morphology and configuration of ternary heterostructures for improving their photocatalytic activity. *ACS Appl. Mater. Interfaces*, **8** (7), 4516–4522.

207 Lin, X., Guo, X., Shi, W., Zhao, L., Yan, Y., and Wang, Q. (2015) Ternary heterostructured Ag–$BiVO_4$/$InVO_4$ composites: synthesis and enhanced visible-light-driven photocatalytic activity. *J. Alloys Compd.*, **635**, 256–264.

208 Shi, Y., Chen, Y., Tian, G., Wang, L., Xiao, Y., and Fu, H. (2015) Hierarchical Ag/Ag_2S/CuS ternary heterostructure composite as an efficient visible-light photocatalyst. *ChemCatChem*, **7**, 1684–1690.

209 Zhan, J., Zhang, H., and Zhu, G. (2014) Magnetic photocatalysts of cenospheres coated with Fe_3O_4/TiO_2 core/shell nanoparticles decorated with Ag nanopartilces. *Ceram. Int.*, **40** (6), 8547–8559. .

210 Habibi-Yangjeh, A. and Shekofteh-Gohari, M. (2017) Novel magnetic Fe_3O_4/ZnO/$NiWO_4$ nanocomposites: enhanced visible-light photocatalytic performance through *p–n* heterojunctions. *Sep. Purif. Technol.*, **184**, 334–346.

211 Shekofteh-Gohari, M. and Habibi-Yangjeh, A. (2017) Fe_3O_4/ZnO/$CoWO_4$ nanocomposites: novel magnetically separable visible-light-driven

photocatalysts with enhanced activity in degradation of different dye pollutants. *Ceram. Int.*, **43** (3), 3063–3071.

212 Chen, F., Li, S., Chen, Q., Zheng, X., Fang, S., and Chen, Z. (2016) Construction of rGO/Fe_3O_4/Ag_3PO_4 multifunctional composite as recyclable adsorbent and photocatalysts towards the mixture of dyes in water under visible light irradiation. *Mater. Lett.*, **185**, 561–564.

213 Habibi-Yangjeh, A. and Akhundi, A. (2016) Novel ternary g-C_3N_4/Fe_3O_4/Ag_2CrO_4 nanocomposites: magnetically separable and visible-light-driven photocatalysts for degradation of water pollutants. *J. Mol. Catal. A*, **415**, 122–130.

214 Li, D., Xie, J., Zhang, Y., Qiao, R., Li, S., and Li, Z. (2015) Convenient synthesis of magnetically recyclable Fe_3O_4@C@CdS photocatalysts by depositing CdS nanocrystals on carbonized ferrocene. *J. Alloys Compd.*, **646**, 978–982.

215 Yi, Z., Ye, J., Kikugawa, N., Kako, T., Ouyang, S., Stuart-Williams, H., Yang, H., Cao, J., Luo, W., Li, Z., Liu, Y., and Withers, R.L. (2010) An orthophosphate semiconductor with photooxidation properties under visible-light irradiation. *Nat. Mater.*, **9**, 559–564.

216 Li, J., Guo, Z., Liu, Z., Cui, M., and Zhu, Z. (2015) Ag_3PO_4/TiO_2 heterostructures with enhanced photocatalytic activity. *Phys. Status Solidi A*, **212**, 459–466.

217 Xie, J., Yang, Y., He, H., Cheng, D., Mao, M., Jiang, Q., Song, L., and Xiong, J. (2015) Facile synthesis of hierarchical Ag_3PO_4/TiO_2 nanofiber heterostructures with highly enhanced visible light photocatalytic properties. *Appl. Surf. Sci.*, **355**, 921.

218 Li, Y., Yu, L., Li, N., Yan, W., and Li, X. (2015) Heterostructures of Ag_3PO_4/TiO_2 mesoporous spheres with highly efficient visible light photocatalytic activity. *J. Colloid Interface Sci.*, **450**, 246.

219 Wei, N., Cui, H., Wang, M., Wang, X., Song, X., Ding, L., and Tian, J. (2017) Highly efficient photocatalytic activity of Ag_3PO_4/Ag/ZnS(en)0.5 photocatalysts through Z-scheme photocatalytic mechanism. *RSC Adv.*, **7**, 18392.

220 Chen, Z., Bing, F., Liu, Q., Zhang, Z., and Fang, X. (2015) Novel Z-scheme visible-light-driven Ag_3PO_4/Ag/SiC photocatalysts with enhanced photocatalytic activity. *J. Mater. Chem. A*, **3**, 4652–4658.

221 Shekofteh-Gohari, M. and Habibi-Yangjeh, A. (2015) Ternary ZnO/Ag_3VO_4/Fe_3O_4 nanocomposites: novel magnetically separable photocatalyst for efficiently degradation of dye pollutants under visible-light irradiation. *Solid State Sci.*, **48**, 177–185.

222 Wang, X., Maeda, K., Thomas, A., Takanabe, K., Xin, G., Carlsson, J.M., Domen, K., and Antonietti, M. (2009) A metal-free polymeric photocatalyst for hydrogen production from water under visible light. *Nat. Mater.*, **8**, 76–80.

223 Mousavi, M. and Habibi-Yangjeh, A. (2017) Novel magnetically separable g-C_3N_4/Fe_3O_4/Ag_3PO_4/Co_3O_4 nanocomposites: visible-light-driven photocatalysts with highly enhanced activity. *Adv. Powder Technol.*, **28** (6), 1540–1553.

224 Zou, Y., Shi, J.-W., Ma, D., Fan, Z., Lu, L., and Niu, C. (2017) *In-situ* synthesis of C-doped TiO_2@g-C_3N_4 core-shell hollow nanospheres with enhanced

visible-light photocatalytic activity for H_2 evolution. *Chem. Eng. J.* doi: 10.1016/j.cej.2017.04.056

225 Zeng, Y., Wang, Y., Chen, J., Jiang, Y., Kiani, M., Li, B., and Wang, R. (2016) Fabrication of high-activity hybrid $NiTiO_3$/g-C_3N_4 heterostructured photocatalysts for water splitting to enhanced hydrogen production. *Ceram. Int.*, **42** (10), 12297–12305.

226 Wang, Q., Hui, J., Huang, Y., Ding, Y., Cai, Y., Yin, S., Li, Z., and Su, B. (2014) The preparation of BiOCl photocatalyst and its performance of photodegradation on dyes. *Mater. Sci. Semicond. Process.*, **17**, 87–93.

227 Zhang, K.-L., Liu, C.-M., Huang, F.-Q., Zheng, C., and Wang, W.-D. (2006) Study of the electronic structure and photocatalytic activity of the BiOCl photocatalyst. *Appl. Catal. B*, **68** (3–4), 125–129.

228 Li, Y., Tian, Y., Zhang, R., Ma, L., Zhou, C., and Tian, X. (2016) Hierarchical BiOCl microspheres with narrow band gap as visible light active photocatalysts. *Inorg. Chim. Acta*, **439**, 123–129.

229 Ge, J., Guo, X., Xu, X., Zhang, P., Zhu, J., and Wang, J. (2015) A eutectic mixture of choline chloride and urea as an assisting solvent in the synthesis of flower-like hierarchical BiOCl structures with enhanced photocatalytic activity. *RSC Adv.*, **5**, 49598–49605.

230 Cheng, H., Huang, B., and Dai, Y. (2014) Engineering BiOX (X = Cl, Br, I) nanostructures for highly efficient photocatalytic applications. *Nanoscale*, **6**, 2009–2026.

231 Kong, L., Jiang, Z., Xiao, T.C., Lu, L.F., Jones, M.O., and Edwards, P.P. (2011) Exceptional visible-light-driven photocatalytic activity over BiOBr-$ZnFe_2O_4$ heterojunctions. *Chem. Commun.*, **47**, 5512–5514.

232 Choi, Y.I., Kim, Y.-I., Cho, D.W., Kang, J.-S., Leung, K.T., and Sohn, Y. (2015) Recyclable magnetic $CoFe_2O_4$/BiOX (X =Cl, Br and I) microflowers for photocatalytic treatment of water contaminated with methyl orange, rhodamine B, methylene blue, and a mixed dye. *RSC Adv.*, **5**, 79624–79634.

233 Jiang, R., Zhu, H.Y., Li, J.B., Fu, F.Q., Yao, J., Jiang, S.T., and Zeng, G.M. (2016) Fabrication of novel magnetically separable BiOBr/$CoFe_2O_4$ microspheres and its application in the efficient removal of dye from aqueous phase by an environment-friendly and economical approach. *Appl. Surf. Sci.*, **364**, 604–612.

234 Lv, D., Zhang, D.F., Liu, X.Y., Liu, Z.R., Hu, L.J., Pu, X.P., Ma, H.Y., Li, D.C., and Dou, J.M. (2016) Magnetic $NiFe_2O_4$/BiOBr composites: one-pot combustion synthesis and enhanced visible-light photocatalytic properties. *Sep. Purif. Technol.*, **158**, 302–307.

235 Liu, D., Yao, W., Wang, J., Liu, Y., Zhang, M., and Zhu, Y. (2015) Enhanced visible light photocatalytic performance of a novel heterostructured $Bi_4O_5Br_2$/$Bi_{24}O_{31}Br_{10}$/Bi_2SiO_5 photocatalyst. *Appl. Catal. B*, **172–173**, 100–107.

236 Tanwar, R., Kaur, B., and Mandal, U.K. (2017) Highly efficient and visible light driven $Ni_{0.5}Zn_{0.5}Fe_2O_4$@PANI modified BiOCl heterocomposite catalyst for water remediation. *Appl. Catal. B.* doi: 10.1016/j.apcatb.2017.04.051.

237 Ray, C. and Pal, T. (2017) Recent advances of metal-metal oxide nanocomposites and their tailored nanostructures in numerous catalytic applications. *J. Mater. Chem. A.*

238 Al-Hamdi, A.M., Rinner, U., and Sillanpää, M. (2017) Tin dioxide as a photocatalyst for water treatment: a review. *Process Saf. Environ.*, **107**, 190–205.

239 Liu, H., Xu, Z., Zhang, Z., and Ao, D. (2016) Highly efficient photocatalytic H_2 evolution from water over $CdLa_2S_4$/mesoporous g-C_3N_4 hybrids under visible light irradiation. *Appl. Catal. B*, **192**, 234–241.

240 Wen, J., Xie, J., Chen, X., and Li, X. (2017) A review on g-C_3N_4-based photocatalysts. *Appl. Surf. Sci.*, **391**, Part B, 72–123.

241 Parida, K.M., Reddy, K.H., Martha, S., Das, D.P., and Biswal, N. (2010) Fabrication of nanocrystalline $LaFeO_3$: an efficient sol–gel auto-combustion assisted visible light responsive photocatalyst for water decomposition. *Int. J. Hydrogen Energy*, **35** (22), 12161–12168.

242 Zhao, H., Sun, S., Wu, Y., Jiang, P., Dong, Y., and Xu, Z.J. (2017) Ternary graphitic carbon nitride/red phosphorus/molybdenum disulfide heterostructure: an efficient and low cost photocatalyst for visible-light-driven H_2 evolution from water. *Carbon*, **119**, 56–61.

243 Fang, X., Song, J., Shi, H., Kang, S., Li, Y., Sun, G., and Cui, L. (2017) Enhanced efficiency and stability of $Co_{0.5}Cd_{0.5}S$/g-C_3N_4 composite photo-catalysts for hydrogen evolution from water under visible light irradiation. *Int. J. Hydrogen Energy*, **42** (9), 5741–5748.

244 Zhou, X., Sun, H., Zhang, H., and Tu, W. (2017) One-pot hydrothermal synthesis of CdS/NiS photocatalysts for high H_2 evolution from water under visible light. *Int. J. Hydrogen Energy*, **42** (16), 11199–11205.

245 Ma, C., Zhou, J., Cui, Z., Wang, Y., and Zou, Z. (2016) *In situ* growth MoO_3 nanoflake on conjugated polymer: an advanced photocatalyst for hydrogen evolution from water solution under solar light. *Sol. Energy Mater. Sol. Cells*, **150**, 102–111.

246 Suarez, C.M., Hernández, S., and Russo, N. (2015) $BiVO_4$ as photocatalyst for solar fuels production through water splitting: a short review. *Appl. Catal. A*, **504**, 158–170.

247 Zeng, Y., Wang, Y., Chen, J., Jiang, Y., Kiani, M., Li, B., and Wang, R. (2016) Fabrication of high-activity hybrid $NiTiO_3$/g-C_3N_4 heterostructured photocatalysts for water splitting to enhanced hydrogen production. *Ceram. Int.*, **42** (10), 12297–12305.

248 Acharya, S., Padhi, D.K., and Parida, K.M. (2017) Visible light driven $LaFeO_3$ nano sphere/RGO composite photocatalysts for efficient water decomposition reaction. *Catal. Today*.

249 Liu, Q., Chai, Y., Zhang, L., Ren, J., and Dai, W.-L. (2017) Highly efficient Pt/$NaNbO_3$ nanowire photocatalyst: its morphology effect and application in water purification and H_2 production. *Appl. Catal. B*, **205**, 505–513.

250 Gaya, U. (2014) *Heterogeneous Photocatalysis Using Inorganic Semiconductor Solids*, Springer, Netherlands, p. 213.

251 Helal, A., Harraz, F.A., Ismail, A.A., Sami, T.M., and Ibrahim, I.A. (2017) Hydrothermal synthesis of novel heterostructured Fe_2O_3/Bi_2S_3 nanorods with enhanced photocatalytic activity under visible light. *Appl. Catal. B*, **213**, 18–27.

252 Li, X., Wang, L., Zhang, L., and Zhuo, S. (2017) A facile route to the synthesis of magnetically separable BiOBr/$NiFe_2O_4$ composites with enhanced photocatalytic performance. *Appl. Surf. Sci.*, **419**, 586–594.

253 Padmapriya, G., Manikandan, A., Krishnasamy, V., Jaganathan, S.K., and Antony, S.A. (2016) Spinel $Ni_xZn_{1-x}Fe_2O_4$ ($0.0 \leq x \leq 1.0$) nano-photocatalysts: synthesis, characterization and photocatalytic degradation of methylene blue dye. *J. Mol. Struct.*, **1119**, 39–47.

254 Wetchakun, N., Chaiwichain, S., Wetchakun, K., Kangwansupamonkon, W., Inceesungvorn, B., and Phanichphant, S. (2013) Synthesis and characterization of novel magnetically separable $CoFe_2O_4/CeO_2$ nanocomposite photocatalysts. *Mater. Lett.*, **113**, 76–79.

255 Nazim, S., Kousar, T., Shahid, M., Azhar Khan, M., Nasar, G., Sher, M., and Warsi, M.F. (2016) New graphene-$Co_xZn_{1-x}Fe_2O_4$ nano-heterostructures: magnetically separable visible light photocatalytic materials. *Ceram. Int.*, **42** (6), 7647–7654.

256 Zhang, D., Pu, X., Gao, Y., Su, C., Li, H., Li, H., and Hang, W. (2013) One-step combustion synthesis of $CoFe_2O_4$–graphene hybrid materials for photodegradation of methylene blue. *Mater. Lett.*, **113**, 179–181.

257 Wang, C., Shi, Z., Peng, L., He, W., Li, B., and Li, K. (2017) Preparation of carbon foam-loaded nano-TiO_2 photocatalyst and its degradation on methyl orange. *Surf. Interfaces*, **7**, 116–124.

258 Trandafilović, L.V., Jovanović, D.J., Zhang, X., Ptasińska, S., and Dramićanin, M.D. (2017) Enhanced photocatalytic degradation of methylene blue and methyl orange by ZnO:Eu nanoparticles. *Appl. Catal. B*, **203**, 740–752.

259 Dorraj, M., Alizadeh, M., Sairi, N.A., Basirun, W.J., Goh, B.T., Woi, P.M., and Alias, Y. (2017) Enhanced visible light photocatalytic activity of copper-doped titanium oxide–zinc oxide heterojunction for methyl orange degradation. *Appl. Surf. Sci.*, **414**, 251–261.

260 Mousavi, M., Habibi-Yangjeh, A., and Abitorabi, M. (2016) Fabrication of novel magnetically separable nanocomposites using graphitic carbon nitride, silver phosphate and silver chloride and their applications in photocatalytic removal of different pollutants using visible-light irradiation. *J. Colloid Interface Sci.*, **480**, 218–231.

261 Rahimi-Nasrabadi, M., Behpour, M., Sobhani-Nasab, A., and Jeddy, M.R. (2016) Nanocrystalline Ce-doped copper ferrite: synthesis, characterization, and its photocatalyst application. *J. Mater. Sci. Mater. Electron.* doi: 10.1007/s10854-016-5305-8

262 Chen, Z., Liao, J., Chen, Y., Zhang, J., Fan, W., and Huang, Y. (2016) Synthesis of oxygen deficient BiOI for photocatalytic degradation of methyl orange. *Inorg. Chem. Commun.*, **74**, 39–41.

263 Wu, X., Zhang, D., Jiao, F., and Wang, S. (2016) Visible-light-driven photodegradation of methyl orange using Cu_2O/ZnAl calcined layered double hydroxides as photocatalysts. *Colloids Surf. A*, **508**, 110–116.

264 Golzad-Nonakaran, B. and Habibi-Yangjeh, A. (2016) Ternary ZnO/AgI/Ag_2CO_3 nanocomposites: novel visible-light-driven photocatalysts with excellent activity in degradation of different water pollutants. *Mater. Chem. Phys.*, **184**, 210–221.

265 Mousavi, M. and Habibi-Yangjeh, A. (2016) Magnetically separable ternary g-C_3N_4/Fe_3O_4/BiOI nanocomposites: novel visible-light-driven photocatalysts based on graphitic carbon nitride. *J. Colloid Interface Sci.*, **465**, 83–92.

266 Akhundi, A. and Habibi-Yangjeh, A. (2016) Codeposition of AgI and Ag_2CrO_4 on g-C_3N_4/Fe_3O_4 nanocomposite: novel magnetically separable visible-light-driven photocatalysts with enhanced activity. *Adv. Powder Technol.*, **27** (6), 2496–2506.

267 Akhundi, A. and Habibi-Yangjeh, A. (2017) High performance magnetically recoverable g-C_3N_4/Fe_3O_4/Ag/Ag_2SO_3 plasmonic photocatalyst for enhanced photocatalytic degradation of water pollutants. *Adv. Powder Technol.*, **28** (2), 565–574.

268 Shekofteh-Gohari, M. and Habibi-Yangjeh, A. (2016) Fabrication of novel magnetically separable visible-light-driven photocatalysts through photosensitization of Fe_3O_4/ZnO with $CuWO_4$. *J. Ind. Eng. Chem.*, **44**, 174–184.

269 Bai, S., Shen, X., Zhong, X., Liu, Y., Zhu, G., Xu, X., and Chen, K. (2012) One-pot solvothermal preparation of magnetic reduced graphene oxide-ferrite hybrids for organic dye removal. *Carbon*, **50** (6), 2337–2346.

270 Ma, J., Huang, D., Zhang, W., Zou, J., Kong, Y., Zhu, J., and Komarneni, S. (2016) Nanocomposite of exfoliated bentonite/g-C_3N_4/Ag_3PO_4 for enhanced visible-light photocatalytic decomposition of rhodamine B. *Chemosphere*, **162**, 269–276.

271 Li, G., Wong, K.H., Zhang, X., Hu, C., Yu, J.C., Chan, R.C.Y., and Wong, P.K. (2009) Degradation of acid orange 7 using magnetic AgBr under visible light: the roles of oxidizing species. *Chemosphere*, **76** (9), 1185–1191.

272 Li, D. and Shi, W. (2016) Recent developments in visible-light photocatalytic degradation of antibiotics. *Chin. J. Catal.*, **37** (6), 792–799.

273 Ha-Tran Thi, V. and Lee, B.-K. (2017) Effective photocatalytic degradation of paracetamol using La-doped ZnO photocatalyst under visible light irradiation. *Mater. Res. Bull.* doi: 10.1016/j.materresbull.2017.04.028

274 Shi, W., Guo, F., and Yuan, S. (2017) *In situ* synthesis of Z-scheme Ag_3PO_4/$CuBi_2O_4$ photocatalysts and enhanced photocatalytic performance for the degradation of tetracycline under visible light irradiation. *Appl. Catal. B*, **209**, 720–728.

275 Yan, M., Hua, Y., Zhu, F., Gu, Wei., Jiang, J., Shen, H., and Shi, W. (2017) Fabrication of nitrogen doped graphene quantum dots-BiOI/$MnNb_2O_6$ p-n junction photocatalysts with enhanced visible light efficiency in photocatalytic degradation of antibiotics. *Appl. Catal. B*, **202**, 518–527.

276 Wang, Y., Li, J., Ding, C., Sun, Y., Lin, Y., Sun, W., and Luo, C. (2017) Synthesis of surface plasma photocatalyst Ag loaded TiO_2 nanowire arrays/graphene oxide coated carbon fiber composites and enhancement of the photocatalytic activity for tetracycline hydrochloride degradation. *J. Photochem. Photobiol. A*, **342**, 94–101.

277 Ding, Y., Zhang, G., Wang, X., Zhu, L., and Tang, H. (2017) Chemical and photocatalytic oxidative degradation of carbamazepine by using metastable Bi^{3+} self-doped $NaBiO_3$ nanosheets as a bifunctional material. *Appl. Catal. B*, **202**, 528–538.

278 Priya, B., Shandilya, P., Raizada, P., Thakur, P., Singh, N., and Singh, P. (2016) Photocatalytic mineralization and degradation kinetics of ampicillin and oxytetracycline antibiotics using graphene sand composite and chitosan supported BiOCl. *J. Mol. Catal. A*, **423**, 400–413.

279 Singh, P., Priya, B., Shandilya, P., Raizada, P., Singh, N., Pare, B., and Jonnalagadda, S.B. (2016) Photocatalytic mineralization of antibiotics using 60%WO_3/BiOCl stacked to graphene sand composite and chitosan. *Arabian J. Chem.* doi: 10.1016/j.arabjc.2016.08.005

280 Priya, B., Raizada, P., Singh, N., Thakur, P., and Singh, P. (2016) Adsorptional photocatalytic mineralization of oxytetracycline and ampicillin antibiotics using Bi_2O_3/BiOCl supported on graphene sand composite and chitosan. *J. Colloid Interface Sci.*, **479**, 271–283.

281 Chen, Q., Wu, S., and Xin, Y. (2016) Synthesis of Au–CuS–TiO_2 nanobelts photocatalyst for efficient photocatalytic degradation of antibiotic oxytetracycline. *Chem. Eng. J.*, **302**, 377–387.

282 Xia, J., Zhao, J., Chen, J., Di, J., Ji, M., Xu, L., Chen, Z., and Li, H. (2017) Facile fabrication of g-C_3N_4/$BiPO_4$ hybrid materials via a reactable ionic liquid for the photocatalytic degradation of antibiotic ciprofloxacin. *J. Photochem. Photobiol. A*, **339**, 59–66.

283 Ioannidou, E., Frontistis, Z., Antonopoulou, M., Venieri, D., Konstantinou, I., Kondarides, D.I., and Mantzavinos, D. (2017) Solar photocatalytic degradation of sulfamethoxazole over tungsten – modified TiO_2. *Chem. Eng. J.*, **318**, 143–152.

284 Gómez-Pastora, J., Bringas, E., and Ortiz, I. (2014) Recent progress and future challenges on the use of high performance magnetic nano-adsorbents in environmental applications. *Chem. Eng. J.*, **256**, 187–204.

285 Zhang, F., Zhang, Y., Zhou, C., Yang, Z., Xue, H., and Dionysiou, D.D. (2017) A new high efficiency visible-light photocatalyst made of SnS_2 and conjugated derivative of polyvinyl alcohol and its application to Cr(VI) reduction. *Chem. Eng. J.*, **324**, 140–153.

286 Zheng, Y., Luo, C., Liu, L., Yang, Z., Ren, S., Cai, Y., and Xiong, J. (2016) Synthesis of hierarchical TiO_2/SnO_2 photocatalysts with different morphologies and their application for photocatalytic reduction of Cr(VI). *Mater. Lett.*, **181**, 169–172.

287 Li, Y., Bian, Y., Qin, H., Zhang, Y., and Bian, Z. (2017) Photocatalytic reduction behavior of hexavalent chromium on hydroxyl modified titanium dioxide. *Appl. Catal. B*, **206**, 293–299.

288 Athanasekou, C., Romanos, G.Em., Papageorgiou, S.K., Manolis, G.K., Katsaros, F., and Falaras, P. (2017) Photocatalytic degradation of hexavalent chromium emerging contaminant via advanced titanium dioxide nanostructures. *Chem. Eng. J.*, **318**, 171–180.

289 Moakhar, R.S., Goh, G.K.L., Dolati, A., and Ghorbani, M. (2017) Sunlight-driven photoelectrochemical sensor for direct determination of hexavalent chromium based on Au decorated rutile TiO_2 nanorods. *Appl. Catal. B* **201**, 411–418.

290 Naimi-Joubani, M., Shirzad-Siboni, M., Yang, J.-K., Gholami, M., and Farzadkia, M. (2015) Photocatalytic reduction of hexavalent chromium with illuminated ZnO/TiO_2 composite. *J. Ind. Eng. Chem.*, **22**, 317–323.

291 Kumordzi, G., Malekshoar, G., Yanful, E.K., and Ray, A.K. (2016) Solar photocatalytic degradation of Zn^{2+} using graphene based TiO_2. *Sep. Purif. Technol.*, **168**, 294–301.

292 Harraz, F.A., Abdel-Salam, O.E., Mostafa, A.A., Mohamed, R.M., and Hanafy, M. (2013) Rapid synthesis of titania–silica nanoparticles photocatalyst by a modified sol–gel method for cyanide degradation and heavy metals removal. *J. Alloys Compd.*, **551**, 1–7.

293 Mishra, T., Hait, J., Aman, N., Jana, R.K., and Chakravarty, S. (2007) Effect of UV and visible light on photocatalytic reduction of lead and cadmium over titania based binary oxide materials. *J. Colloid Interface Sci.*, **316, 1**, 80–84.

294 Ayawanna, J., Teoh, W., Niratisairak, S., and Sato, K. (2015) Gadolinia-modified ceria photocatalyst for removal of lead (II) ions from aqueous solutions. *Mater. Sci. Semicond. Process.*, **40**, 136–139.

295 Saien, J., Ghamari, F., and Azizi, A. (2016) The role of counter-anions in photocatalytic reduction of Ni(II) with a trace amount of titania nanoparticles. *J. Iran Chem. Soc.*, **13**, 2247.

296 Saien, J., Azizi, A., and Soleymani, A.R. (2014) Optimized photocatalytic conversion of Ni(II) ions with very low titania nanoparticles at different temperatures, kinetics and energy consumption. *Sep. Purif. Technol.*, **134**, 187–195.

297 Wang, G., Zhen, J., Zhou, L., Wu, F., and Deng, N. (2015) Adsorption and photocatalytic reduction of U(VI) in aqueous TiO_2 suspensions enhanced with sodium formate. *J. Radioanal. Nucl. Chem.*, **304** (2), 579–585.

298 Zhang, A., Zhang, L., Lu, H., Chen, G., Liu, Z., Xiang, J., and Sun, L. (2016) Facile synthesis of ternary Ag/AgBr-Ag_2CO_3 hybrids with enhanced photocatalytic removal of elemental mercury driven by visible light. *J. Hazard. Mater.*, **314**, 78–87.

299 Aman, N., Mishra, T., Hait, J., and Jana, R.K. (2011) Simultaneous photoreductive removal of copper (II) and selenium (IV) under visible light over spherical binary oxide photocatalyst. *J. Hazard. Mater.*, **186** (1), 360–366.

300 Schneider, J., Bahnemann, D., Ye, J., Puma, G.L., and Dionysiou, D.D. (2016) *Photocatalysis Fundamentals and Perspectives*, The Royal Society of Chemistry, p. 452.

301 Sun, Z., Wang, H., Wu, Z., and Wang, L. (2017) g-C_3N_4 based composite photocatalysts for photocatalytic CO_2 reduction. *Catal. Today.* doi: 10.1016/j.cattod.2017.05.033

302 Inoue, T., Fujishima, A., Konishi, S., and Honda, K. (1979) Photoelectrocatalytic reduction of carbon dioxide in aqueous suspensions of semiconductor powders. *Nature*, **277**, 637–638.

303 Nikokavoura, A. and Trapalis, C. (2017) Alternative photocatalysts to TiO_2 for the photocatalytic reduction of CO_2. *Appl. Surf. Sci.*, **391**, Part B, 149–174.

304 Low, J., Cheng, B., and Yu, J. (2017) Surface modification and enhanced photocatalytic CO_2 reduction performance of TiO_2: a review. *Appl. Surf. Sci.*, **392**, 658–686.

305 Sohn, Y., Huang, W., and Taghipour, F. (2017) Recent progress and perspectives in the photocatalytic CO_2 reduction of Ti-oxide-based nanomaterials. *Appl. Surf. Sci.*, **396**, 1696–1711.

306 Ali, K.A., Zuhairi, A., and Mohamed, A.R. (2017) Visible light responsive TiO_2 nanoparticles modified using Ce and La for photocatalytic reduction of CO_2: effect of Ce dopant content. *Appl. Catal. A*, **537**, 111–120.

307 Baran, T., Wojtyła, S., Dibenedetto, A., Aresta, M., and Macyk, W. (2015) Zinc sulfide functionalized with ruthenium nanoparticles for photocatalytic reduction of CO_2. *Appl. Catal. B*, **178**, 170–176.

308 Zhu, Z., Qin, J., Jiang, M., Ding, Z., and Hou, Y. (2017) Enhanced selective photocatalytic CO_2 reduction into CO over Ag/CdS nanocomposites under visible light. *Appl. Surf. Sci.*, **391**, Part B, 572–579.

309 Ye, S., Wang, R., Wu, M.-Z., and Yuan, Y.-P. (2015) A review on g-C_3N_4 for photocatalytic water splitting and CO_2 reduction. *Appl. Surf. Sci.*, **358**, Part A, 15–27.

310 He, Y., Zhang, L., Teng, B., and Fan, M. (2015) New application of Z-scheme Ag_3PO_4/g-C_3N_4 composite in converting CO_2 to fuel. *Environ. Sci. Technol.*, **49** (1), 649–656.

311 Dai, W., Xu, H., Yu, J., Hu, X., Luo, X., Tu, X., and Yang, L. (2015) Photocatalytic reduction of CO_2 into methanol and ethanol over conducting polymers modified Bi_2WO_6 microspheres under visible light. *Appl. Surf. Sci.*, **356**, 173–180.

312 Bai, Y., Ye, L., Chen, T., Wang, P., Wang, L., Shi, X., and Wong, P.K. (2017) Synthesis of hierarchical bismuth-rich $Bi_4O_5Br_xI_{2-x}$ solid solutions for enhanced photocatalytic activities of CO_2 conversion and Cr(VI) reduction under visible light. *Appl. Catal. B*, **203**, 633–640.

313 Wang, J.-C., Yao, H.-C., Fan, Z.-Y., Zhang, L., Wang, J.-S., Zang, S.-Q., and Li, Z.-J. (2016) Indirect Z-scheme BiOI/g-C_3N_4 photocatalysts with enhanced photoreduction CO_2 activity under visible light irradiation. *ACS Appl. Mater. Interfaces*, **8** (6), 3765–3775.

314 Ye, L., Jin, X., Ji, X., Liu, C., Su, Y., Xie, H., and Liu, C. (2016) Facet-dependent photocatalytic reduction of CO_2 on BiOI nanosheets. *Chem. Eng. J.*, **291**, 39–46.